SEA ICE CONCENTRATION DETERMINATION IN LANCASTER SOUND, EASTERN GATEWAY TO THE NORTHWEST PASSAGE, 2015-2024 USING SATELLITE THERMAL DATA

DÉTERMINATION DE LA CONCENTRATION DE GLACE DE MER DANS LE DÉTROIT DE LANCASTER, PORTE D'ENTRÉE DE L'EST DU PASSAGE DU NORD-OUEST, 2015-2024 À L'AIDE DE DONNÉES THERMIQUES SATELLITAIRES

A Thesis Submitted to the Division of Graduate Studies
of the Royal Military College of Canada
by

Sean G. Leithead, CD, BEng, MASc, P.Eng.
Major

In Partial Fulfillment of the Requirements for the Degree of
Master of Science in Physics (Space Science)
April 2026

To Megan, Grant, Norah and Mairi

Acknowledgements

Thank you very much to Dr. Ron Vincent at RMC for being my thesis supervisor. He introduced me to the world of remote sensing, provided excellent guidance, and allowed me to test his ice concentration algorithm on the Canadian Arctic. Thank you to Dr. L. Sangalli and Maj David Anderson for their space expertise and involvement with the Audimus cubesat. Thank you to Dr. Catharine Marsden, former Dean of Engineering, Col Chris Renahan, Commanding Officer of Military Post Grad Students and Military Faculty, and Dr. Jean-Marc Noël, Dean of Graduate Studies, for their leadership and their support. Thank you to Maj Marie-Michèle Siu in the Canadian Armed Forces' Directorate of Space Requirements for her support. Thank you to Dr. Billy Allan, current Dean of Engineering and my previous MASc degree supervisor, for his continued belief and encouragement. Thank you also to Dr. Marc LaViolette and Dr. David DuQuesnay from the Mech/Aero Eng Department. Thank you to Mich Lavoie for providing tech support and drive space to download a multitude of satellite images. Thank you to my parents, Greg and Mona Leithead, and my brother Mark Leithead, for their support of my love of space and spaceflight which began in my youth. Last but not least, thank you to my wonderful wife Megan, my son Grant, my daughter Norah and my dog Mairi for their caring, support and understanding while I set off in a different city to learn more about space.

Abstract

A novel ice concentration (IC) algorithm based on sea surface temperatures (SST) generated from MetOp-A, -B and -C Advanced Very High Resolution Radiometer (AVHRR) satellite images was tested on Lancaster Sound in the Canadian Arctic, 2015-2024. Lancaster Sound is an operationally important region and the eastern entrance to the Northwest Passage. The IC algorithm used the Single-Channel Composite Arctic Sea Surface Temperature Algorithm (CASSTA) and thermal infrared satellite data as its basis, and was termed AVHRR CASSTA-based IC (ACIC). Weekly ACIC images were generated for 2015-2024. Sentinel-1 and RADARSAT Constellation Mission (RCM) Synthetic Aperture Radar (SAR) satellite images were used for gap-filling, Sentinel-1 in 2015-2019 and RCM in 2020-2024, when AVHRR images were too cloudy. AVHRR visible channel was used for gap-filling during times of year when SST was too warm for ACIC to be accurate and daylight was present. Isodata unsupervised classification analysis was used for SAR and AVHRR visible channel images to determine IC. IC results over the 10-year period were compared with Canadian Ice Service (CIS) ice chart results and University of Bremen passive microwave (PM) IC maps. Ten-year average melt and freeze dates in Lancaster Sound were determined to be Jun 2 & Oct 20, respectively. Ten-year average ACIC results reported 0.6-2.9 tenths lower IC values than CIS ice chart results, depending on the time of year, and 0.0-1.6 tenths lower IC values than U Bremen PM results, depending on the time of year. However, IC results of all three data methods were nearly in agreement when uncertainty ranges were included: 100% between ACIC and U Bremen PM, and 88% between ACIC and CIS ice charts. Hydrophone and/or sonobuoy water deployment date ranges, to support the Audimus cubesat mission, were determined to be Jun 2 - Oct 20 for Polar Class 6 & 7 ice strengthened ship detection, with an additional period of Mar 1 - Jun 2 where an appreciable region of open water was present east of the ice arch but bounded by ice further east. Based on this research, ACIC is applicable for further arctic research & supporting operational monitoring/assessment of IC.

Résumé

Un nouvel algorithme de concentration de glace (CG) basé sur les températures de surface de la mer (TSM) générées à partir d'images satellitaires du radiomètre AVHRR (Advanced Very High Resolution Radiometer) des satellites MetOp-A, -B et -C a été testé dans le détroit de Lancaster, dans l'Arctique canadien, de 2015 à 2024. Le détroit de Lancaster est une zone d'importance opérationnelle et constitue l'entrée de l'est du passage du Nord-Ouest. Cet algorithme de CG utilise l'algorithme CASSTA (Single-Channel Composite Arctic Sea Surface Temperature Algorithm) et des données satellites infrarouges thermiques; il a été nommé AVHRR CASSTA-based ice concentration en anglais (ACIC). Des images ACIC hebdomadaires ont été générées pour la période 2015-2024. Des images satellitaires radar à synthèse d'ouverture (RSO) Sentinel-1 et Mission de la Constellation RADARSAT (MCR) ont été utilisées pour combler les lacunes, Sentinel-1 de 2015 à 2019 et MCR de 2020 à 2024, lorsque les images AVHRR étaient trop nuageuses. Le canal visible de l'AVHRR a été utilisé pour combler les lacunes pendant les périodes de l'année où la TSM était trop élevée pour que l'ACIC soit précis et où la lumière du jour était présente. Une analyse de classification non supervisée isodata a été utilisée pour les images RSO et du canal visible de l'AVHRR afin de déterminer la CG. Les résultats de CG sur une période de 10 ans ont été comparés à ceux des cartes de glace du Service canadien des glaces (SCG) et aux cartes CG obtenues par micro-ondes passives (MP) de l'Université de Brêmen. Les dates moyennes de fonte et de gel sur 10 ans dans le détroit de Lancaster ont été déterminées respectivement le 2 juin et le 20 octobre. Les résultats moyens de l'ACIC sur 10 ans ont rapporté des valeurs d'CG inférieures de 0,6 à 2,9 dixièmes à celles des cartes de glace du SCG, selon la période de l'année, et de 0,0 à 1,6 dixièmes à celles des données MP de l'Université de Brêmen, selon la période de l'année. Cependant, les résultats de CG des trois méthodes de données étaient presque concordants lorsque les intervalles d'incertitude étaient inclus: 100% entre l'ACIC et les données MP de l'Université de Brêmen, et 88% entre l'ACIC et les cartes de glace du SCG. Les périodes de déploiement des hydrophones et/ou des sonobouées dans l'eau, en soutien à la mission du cubesat Audimus, ont été fixées du 2 juin au 20 octobre pour la détection des navires renforcés par la glace de classe polaire 6 et 7. Une période supplémentaire, du 1er mars au 2 juin, a été envisagée durant laquelle une zone d'eau libre importante était présente à l'est de l'arche de glace, mais bordée par la glace plus à l'est. Ces recherches confirment l'applicabilité de l'ACIC à la poursuite des recherches arctiques et au soutien du suivi et de l'évaluation opérationnels de CG.

Contents

List of Tables

List of Figures

List of Acronyms and Abbreviations

ACIC	AVHRR CASSTA-based Ice Concentration
ADCP	Acoustic Doppler Current Profiler
AIS	Automatic Identification System
AMSR	Advanced Microwave Scanning Radiometer
ASCAT	Advanced Scatterometer
ASI	Arctic Radiation and Turbulence Interaction Study Sea Ice
ASST	Arctic Sea Surface Temperaure
AVHRR	Advanced Very High Resolution Radiometer
BSRTO	Barrow Strait Observatory
BT	Brightness Temperature
BTD	Brightness Temperature Difference
CAA	Canadian Arctic Archipelago
CASSTA	Composite Arctic Sea Surface Temperature Algorithm
CCG	Canadian Coast Guard
CIS	Canadian Ice Service
CLASS	Comprehensive Large Array-Data Stewardship System
CNN	Convolutional Neural Network
CP	Compact Polarimetric
dB	Decibels
DIFAR	Directional Frequency Analysis and Recording
DP	Dual Polarization
DRDC	Defence Research and Development Canada
EODMS	Earth Observation Data Management System
ESA	European Space Agency
EUMETSAT	European Organisation for the Exploitation of Meteorological Satellites

EW	Extra Wide swath mode
FRAC	Full Resolution Area Coverage
FS	Finnish-Swedish
FYI	First-Year Ice
GHRSST	Group for High-Resolution Sea Surface Temperature
GMT	Greenich Mean Time
GPS	Global Positioning System
GRD	Ground Range Detected
HH	Horizontal-Horizontal polarization
HV	Horizontal-Vertical polarization
IC	Ice Concentration
IPS	Ice Profiling Sonar
IR	Infrared
IST	Ice Surface Temperature
IW	Interferometric Wide swath mode
JAXA	Japan Aerospace Exploration Agency
LCC-VLA	Low Cost/Low Complexity Vertical Line Array
MIZ	Marginal Ice Zone
MIZST	Marginal Ice Zone Surface Temperature
MLP	Multilayer Perception
MODIS	Moderate Resolution Imaging Spectroradiometer
MYI	Multi-Year Ice
NASA	National Aeronautics and Space Administration
NESZ	Noise-Equivalent Sigma Zero
NN	Neural Network
NOAA	National Oceanic and Atmospheric Administration
NOW	North Open Water
NWP	Northwest Passage
OW	Open Water
PC	Polar Class
PM	Passive Microwave
POES	Polar-Orbiting Environmental Satellites
RCM	RADARSAT Constellation Mission
RGB	Red Green Blue
ROI	Region of Interest
RMC	Royal Military College of Canada
SAR	Synthetic Aperture Radar
SC30M	ScanSAR 30 m
SC50M	ScanSAR 50 m
SC100M	ScanSAR 100 m

SCLN	ScanSAR Low Noise
SM	StripMap swath mode
SSM/I	Special Sensor Microwave/Imager
SSO	Sun Synchronous Orbit
SST	Sea Surface Temperature
STK	Systems Tool Kit
SWIR	Short-Wave Infrared
TIR	Thermal Infrared
U	University
UHF	Ultra High Frequency
UTM	Universal Transverse Mercator
VH	Vertical-Horizontal polarization
VHF	Very High Frequency
VIIRS	Visible Infrared Imaging Radiometer Suite
VNIR	Visible/Near Infrared
VV	Vertical-Vertical polarization
WMO	World Meteorological Organization

1 Introduction

1.1 Overview

A significant portion of Canada stretches north of the Arctic Circle. Arctic sea ice depletion in recent history has resulted in increased interest in the Canadian Arctic in terms of shipping traffic and impacts to Canadian sovereignty. Satellites in polar orbits are an advantageous method of monitoring this region. This Chapter introduces the Region of Interest (ROI) of the research for this thesis, increased navigability of the ROI, Royal Military College of Canada (RMC) Audimus cubesat mission, hydrophone and sonobuoy background, sea ice concentration (IC) characteristics and polynyas, and the goal/mission of the research.

1.2 Lancaster Sound in the Northwest Passage

The ROI for the research for this thesis is Lancaster Sound, part of the Canadian Arctic, north of the Arctic Circle, and the eastern entrance/exit of the Northwest Passage (NWP). This research analyzed the region from Resolute in the west to the eastern edge of Devon Island, which is approximately 500 km long by 60-75 km wide. Fig. 1.1 shows Lancaster Sound's place in the global Arctic Ocean region, Fig. 1.2 shows the location of Lancaster Sound within the NWP, and Fig. 1.3 zooms in to show Lancaster Sound itself. The region between Resolute and Prince Leopold Island is also referred to as Barrow Strait, however for this research, Lancaster Sound and Barrow Strait together are referred to as Lancaster Sound.

Due to changing climate and sea ice dynamics in the region, the NWP has become more traversable for shipping traffic [1–4]. The northern route of the NWP became ice-free for the first time during the summer of 2007 [1]. Though Canada claims that the NWP falls within its internal waters, countries such as the United States, the European Union, Denmark, Russia, Norway and

Japan have challenged this claim, stating that it should be considered an international strait since it connects the Atlantic and Pacific Oceans [5, 6]. There have also been warnings about non-Canadian submarine activity in the Canadian Arctic [7].

Figure 1.1: Map of the countries surrounding the Arctic Ocean, claiming land in the Arctic region (Lancaster Sound identified) (adapted from [8])

Figure 1.2: Lancaster Sound within the Northwest Passage (adapted from [9])

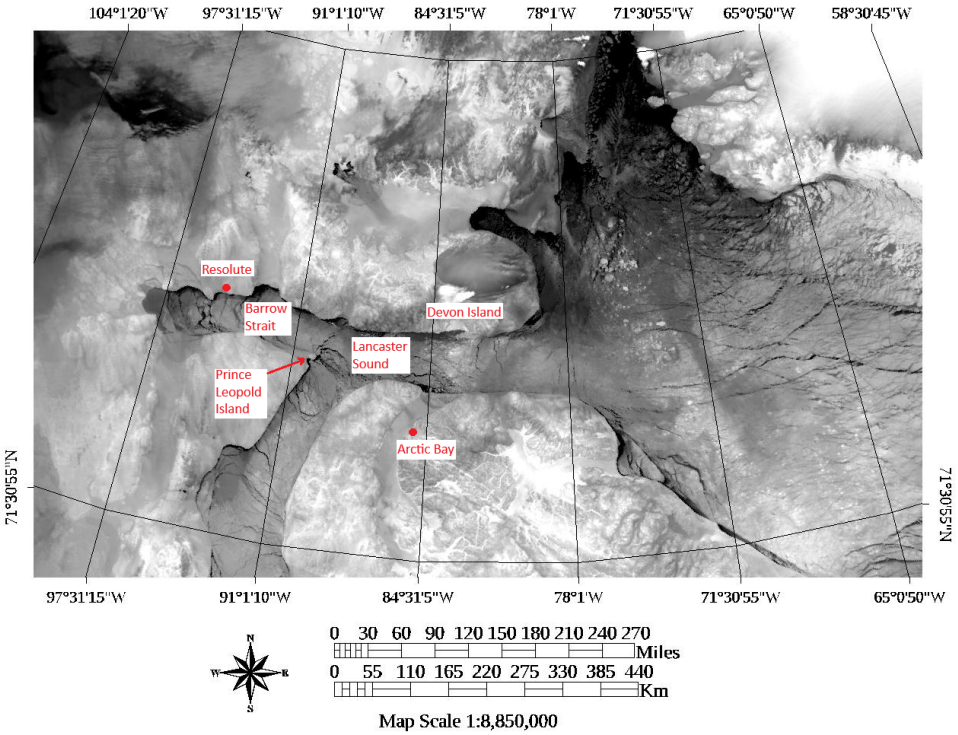

Figure 1.3: Lancaster Sound satellite thermal IR imagery map (Jan 14, 2019)

1.3 Operational Monitoring

The NWP, shown in Fig. 1.2, is an option for the strategic movement of naval assets including nuclear submarines from the Arctic Ocean to the Atlantic, or vice versa [10]. Detection under ice is difficult from above, and although long-range patrols carried out by CP140 Aurora aircraft can drop sonobuoys (portable hydrophones) in leads in Arctic Ocean ice, the opportunity is dependent on where the leads are [10]. If a detection was made, the pursuit and attack of an intruder under ice would be very difficult if not impossible, therefore necessitating underwater sensors under the arctic ice [10]. Significant domain awareness of the region is provided from space in Canada via the RADARSAT program, including RADARSAT-2 and RADARSAT Constellation Mission (RCM) satellites [10].

Comprehensive underwater surveillance of the complete Arctic region would be too expensive, and instead, monitoring access choke points would be more achievable [10]. A Defence Research and Development Canada (DRDC) report from 2016 identified suggested NWP choke point surveillance stations [10, 11]. Two of these locations are: near Resolute, and where Lancaster Sound meets Baffin Bay in the east. Lancaster Sound is an easier region to transit than the Canadian Arctic Archipelago (CAA), which is the set of small islands to the west and northwest of Lancaster Sound. The CAA's waters are relatively shallow, and combined with the thickness of the ice, the multitude of islands restricting maneuvering, and limited bathymetry information, result in a dangerous area for submarines, for example [10]. Since Lancaster Sound is deeper, and the eastern entry choke point to the NWP, monitoring of Lancaster Sound was recommended [10–12]. For the research for this thesis however, surface vessels were the operational focus.

1.4 Increased Navigability of Lancaster Sound

Fig. 1.4 shows the resultant mean NWP shipping season lengths in weeks for 2007-2021, based on a Polar Class (PC) 7 medium ice strength ship [1]. PC 7 ships can operate in summer/fall in thin first-year ice (FYI), which may include old ice inclusions [13]. In Fig. 1.4, the Lancaster Sound mean shipping length ranges from approximately 12-25 weeks per year from the 3000 marker heading eastward. For east Lancaster Sound, which is roughly east of the green 500 marker on Fig. 1.4, the mean shipping season is 20-25 weeks [1]. The only section of the NWP that has seen a statistically significant increase in shipping season length is at the eastern entrance to Lancaster Sound, where

the season length increased from 20 weeks in 2007-2011 to 23-25 weeks in 2017-2021 [1]. For the PC 3 high ice strength class, which can operate year-round in second-year ice which may include multi-year ice (MYI) inclusions, there were no sections of the NWP that had a season length of zero weeks [1, 13]. For non-ice strengthened ships, there were no sections that were open year-round [1]. The increase in shipping season length for PC 7 ships in East Lancaster Sound occurred predominantly in the late season (October-November), with an increase of two weeks from 2007 to 2021 [1].

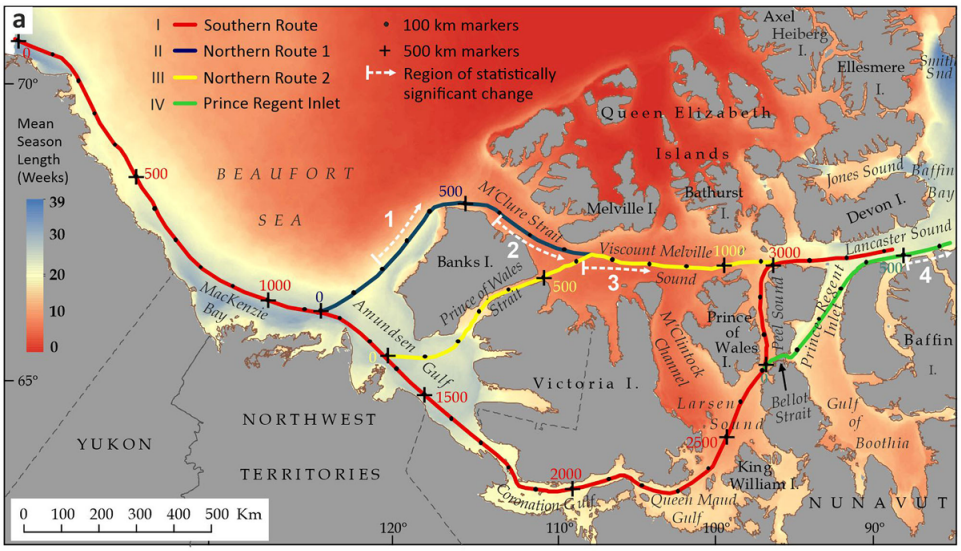

Figure 1.4: NWP map, showing mean shipping season length in weeks for Polar Class 7 ice strengthened ships between 2007-2021 [1]. These ships can operate in summer/fall in medium to thin first year ice. Lancaster Sound is at the eastern edge of the figure.

Another study, based on IC and ice thickness, provided NWP navigability predictions for open water (OW) ships and PC 6 ice strengthened ships [4]. The NWP navigable windows in 2021 for OW ships were mid-August to early October, increasing to beginning of August to early October in 2030 [4]. For PC 6 ships, the navigable window in 2021 was from the beginning of August to late October, increasing to between mid-July to late November in 2030 [4].

Ship trajectories from 2013-2020, based on archives of real-time location observations from vessels with Automatic Identification System (AIS) transmitters and a coupled ocean and sea ice model, were used to analyze Arctic

shipping traffic trends [3]. AIS transmitters are marine navigation safety devices that broadcasts a ship's position, speed, course and identity to other ships and ground stations. Fig. 1.5 shows the number of ship trajectories by Finnish-Swedish (FS) Ice Class category types for the 2013-2020 period, also broken down by month and year. Table 1.1 details some equivalencies between PC and FS class types.

Table 1.1: Icebreaking Ship Class Equivalents [1, 13–15]

Polar Class (PC)	Finnish-Swedish (FS) Class Equivalent	Ice Strength	Capable Ice Depth (m)	Ice Characteristics
PC 3	FS 1A Super	Second year ice	up to 2.5	Second year ice with MYI inclusions
PC 6	FS 1A Super	Medium FYI	> 1	FYI with old ice inclusions
PC 7	FS 1A	Thin FYI	0.5-1	Difficult ice conditions
-	FS 1B	Thin FYI	0.3-0.5	Moderately difficult ice conditions
-	FS 1C	Thin FYI	0.15-0.3	Easy ice conditions
Open Water	FS II	None	-	Requires open water

Fig. 1.5 a) shows that the lowest number of ship trajectories in the NWP was fewer than 20 in late August/early September 2013, and the peak was over 50 in August 2019. In Fig. 1.5 b), the FS 1A/B/C ship trajectories were heavily concentrated between mid-July to mid-September, and in general composed 80 % of the overall traffic. Outside the dashed lines are zero trajectory entries. The FS 1A Super had much less frequent trajectories but can transit between mid-June to mid-October. The FS II vessels were restricted to mid-July to mid-August. Even during September, most ships in the NWP only visited Baffin Bay, east of Lancaster Sound, without navigating deep into the CAA [3].

Reductions in sea ice do not necessarily equate to increased ship navigability [1]. One of the key features to track is the strength (or robustness) of choke points along the route where MYI remains in high concentration while other regions are ice-free during the summer [1]. In addition, several studies have argued that increases in sea ice mobility could reduce safe shipping in the Arctic for ships with limited ice strengthening [1]. For the NWP, the CAA is a pivotal region, and the sea ice freezing and melting in channels of these Canadian islands, for example Barrow Strait and Viscount Melville Sound, greatly impact the operation of Arctic shipping [4].

Since Lancaster Sound becomes ice free during the summer in the 2015-2024 study period [1–4, 16], this means that the strongest ice that could form would be thick FYI. These studies also help frame the expected times of year when melting and freezing occur in the NWP.

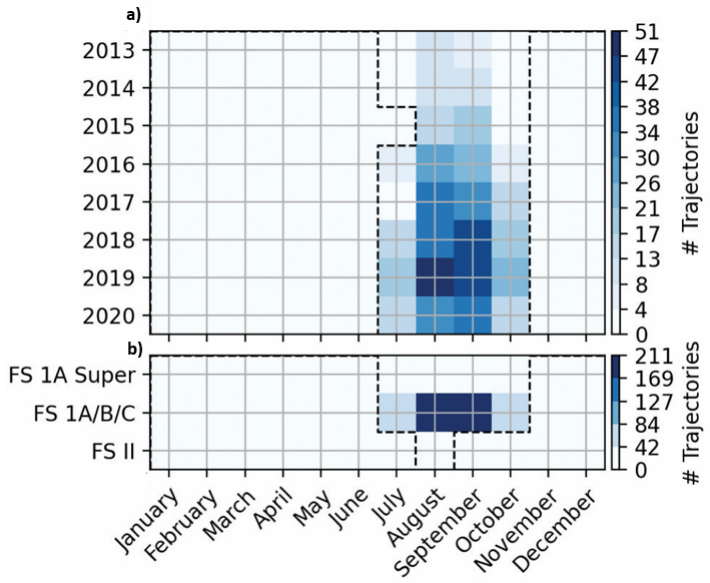

Figure 1.5: Northwest Passage ship trajectories heat map 2013-2020 (adapted from [3]): a) # of ship trajectories for all ship types studied [3] shown by year, and b) # of ship trajectories for FS 1A Super (equivalent to Polar Class (PC) 6) ice strengthened, FS 1A/B/C (FS 1A equivalent to PC 7) lightly ice strengthened, and FS II OW ship types. Months of the year on the bottom axis apply to the entire figure. Black dotted line denotes the outer trajectory boundaries.

1.5 Audimus Cubesat Mission

1.5.1 Mission Overview

The Audimus cubesat mission is a 3U cubesat that, at the time of writing, is planning to be launched by RMC by the end of the decade. Its goal is to listen to acoustic sounds from hydrophones and sonobuoys that are deployed in Lancaster Sound's waters, and transmit these sounds to the RMC ground station. The cubesat will be orbiting in a sun-synchronous low-earth polar orbit within a 500-600 km altitude band at an inclination of approximately 98° [11,17]. An altitude closer to 500 km is preferred due to Very High Frequency (VHF) communications and de-orbit considerations [17]. Fig. 1.6 shows the concept of operations for Audimus. Communications with the hydrophones or sonobuoys is via VHF, and communications with the Ground Station is via Ultra High

Frequency (UHF). Fig. 1.7 shows the planned polar Sun Synchronous Orbit (SSO), with the RMC Kingston ground station and hydrophone example in Lancaster Sound also shown. Computer simulations of the planned orbit using Systems Tool Kit (STK) software, as seen in Fig. 1.7, showed approximately 14 Audimus accesses over Lancaster Sound per day [11].

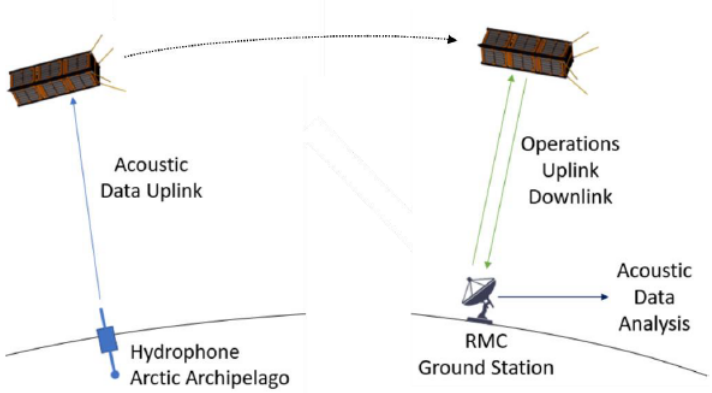

Figure 1.6: RMC Audimus 3U cubesat concept of operations [11]

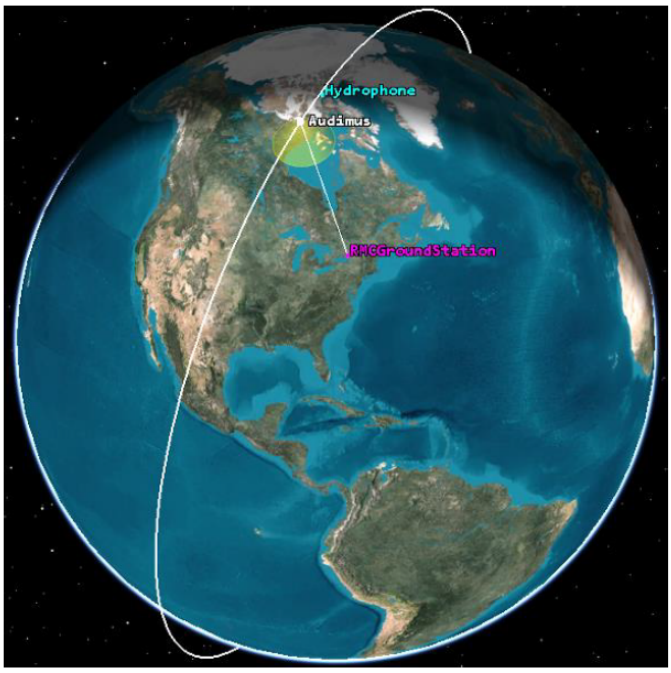

Figure 1.7: STK computer simulation showing Audimus cubesat's planned polar sun-synchronous orbit. RMC Kingston ground station and hydrophone in Lancaster Sound also shown [11].

1.5.2 Hydrophones and Sonobuoys

Two primary hydrophone data sources are being developed to support the Audimus mission [11, 12]. First is a project for a low cost/low complexity vertical line array (LCC-VLA) of hydrophones for the Canadian Arctic, while the second is a refurbishment of the existing Barrow Strait Observatory (BSRTO) [11]. Intended as a through-the-ice, extremely long-term sonobuoy, LCC-VLA is being developed by JASCO Applied Sciences for DRDC Atlantic as a remote monitoring system to bolster underwater surveillance in the Arctic, and is an evolution of a VLA drifter buoy [11, 18]. The LCC-VLA includes a vertical hydrophone array, signal processing hardware, a GPS receiver, a satellite radio, a hull for housing components and ice penetration, and a command centre message parsing system [11].

The BSRTO has been operational since 2011 off Gascoyne Inlet on the southwest coast of Devon Island. The project was initiated to provide real-time ice and ocean data for use by mariners and for input to sea ice forecasting

and climate models [19]. The observatory itself consists of three components: an acoustic telemetry link that passes data from instruments on a sub-surface mooring (node) to an underwater hub, an 8 km long sub-sea cable at a depth of 165 m that carries data from the hub to a shore station in Gascoyne Inlet, and a two-way Iridium satellite link that transmits data from the shore station to the user [19, 20]. The results demonstrated a new capability for accurate freeze-up predictions in northern Barrow Strait. There are three main nodes. The Acoustic Doppler Current Profiler (ADCP) node, which is moored 60 m below the surface, contains a 307 kHz ADCP to measure ocean currents, presence and velocity of sea ice [20]. An Ice Profiling Sonar (IPS) node is moored at 40 m below the surface and is an upward looking sonar to measure ice draft. The third node is a hub node moored a few meters above the sea floor (150 m depth) which contains a smart icListen hydrophone, made by Oceansonics Ltd., that collects passive acoustic data [20]. The addition of the hydrophone demonstrated a capability for year-round under-ice acoustic monitoring of the arctic, and the observatory was able to differentiate between ice-covered vs OW even during periods of consistent ice cover [20]. In addition, an advantage of the icListen hydrophone is that is has an onboard acoustic signal spectral processing capability [20]. A successful test of the hydrophone detected a known nearby Canadian Coast Guard (CCG) ship [20]. While the BSTRO located in the NWP has demonstrated a capability for year-round operation, the acoustic data provided is limited to just two minutes of data per day, which would be insufficient for monitoring of vessel traffic [11]. The Audimus cubesat mission would obtain and transmit more data per day than the current BSTRO setup.

Sonobuoys are portable hydrophones, consisting of a surface float containing a radio transmitter, antenna, electronics package and saltwater-activated battery, along with an underwater component consisting of hydrophones and stabilizing equipment [11]. Sonobuoys can be deployed by aircraft, helicopters or ships. Three sonobuoy types from the Canadian Armed Forces inventory have been considered for use: the SSQ-53D Directional Frequency Analysis and Recording (DIFAR) sonobuoy, the SSQ-573 DIFAR sonobuoy, and geobuoys [11]. The SSQ-53D DIFAR sonobuoy is a proven system that provides directional and omnidirectional acoustic data [11]. The SSQ-573 DIFAR is similar to the SSQ-53D but has an all-digital electronics design [21]. Geobuoys are arctic ice-pick sonobuoys still undergoing trials [11].

1.5.3 Contribution to the Audimus Mission

Results of the research for this thesis will be used to inform hydrophone and/or sonobuoy placement for RMC's Audimus cubesat mission. Placing these in Lancaster Sound will present some unique challenges with ice coverage being a key consideration. In winter, when an ice arch and polynya are present, the area further east is not completely ice free, with drifting ice being pushed out into Baffin Bay [11]. In areas of heavy ice coverage there exist small OW areas or ice leads through which a sonobuoy could be dropped, for example. This requires a high degree of accuracy and will likely result in a significant rate of sensor damage [11]. Sonobuoys must be deployed in clear OW to prevent potential damage or entanglement in the ice, which could seasonally limit air deployment of sonobuoys [11]. Sonobuoys can also be deployed by ship, even in icy conditions, if dropped off the stern as the ship breaks through the ice. The frequent summer presence of CCG ice breakers presents additional opportunities for buoy deployment [11]. While there is still the possibility of damage to the electronics housing from drifting ice, deployment from ice-breaking capable ships is a proven method [11]. Geobuoys can be used on ice packs, and could be used instead of sonobuoys in the Lancaster Sound ice pack west of the formed ice arch until the ice arch collapses [11]. Drifting hydrophones will also need to avoid entanglement in ice floes.

The goal of the Audimus cubesat mission is to demonstrate the ability of satellite acoustic monitoring of Lancaster Sound, and the research for this thesis will aid in providing recommendations on when to deploy hydrophones or sonobuoys in the water, based on sea IC in Lancaster Sound. Thermal Infrared (TIR), Synthetic Aperture Radar (SAR), and visible spectrum satellite imagery were used to analyze the annual sea and ice conditions over a 10-year period, 2015-2024, in Lancaster Sound.

1.6 Sea Ice Concentration and Characteristics

1.6.1 Ice Concentration and Ice Types

For the research for this thesis, sea IC in Lancaster Sound was monitored and analyzed over a 10-year period, 2015-2024, using satellite remote sensing. IC can be categorized within the following categories: consolidated ice, compact ice, very close pack/drift, open drift, very open drift, and ice-free (open) water [22]. Definitions of these categories are provided in Table 1.2. Fig. 1.8 shows pictorial images of various ICs, both from above (circle images) and real-life photos.

Table 1.2: Sea ice types based on IC (adapted from [22])

Concentration Level	Definition
Consolidated Ice	Floating ice in which the concentration is 10/10 and the floes are frozen together.
Compact ice	Floating ice in which the concentration is 10/10 and no water is visible.
Very close pack/drift	Floating ice in which the concentration is 9/10 to less than 10/10.
Close pack/drift	Floating ice in which the concentration is 7/10 to 8/10, composed of floes mostly in contact with one another.
Open drift	Floating ice in which the concentration is 4/10 to 6/10, with many leads and polynyas.
Very open drift	Ice in which the concentration is 1/10 to 3/10 and water dominates over the ice.
Open water (ice-free)	No ice present. If ice of any kind is present, this term shall not be used.

Pack ice is defined as any area of ice where the floating ice has a concentration $> 70\%$, regardless of ice type or form [22]. The Marginal Ice Zone (MIZ) is a buffer between OW and the pack ice. Within the MIZ, the ice edge is a conventional boundary which is marked by an IC threshold of 10% or 15% [22]. Hence, the commonly accepted yet non-rigorous definition of MIZ is that it is part of the ice cover which is close enough to the open ocean boundary to be affected by its presence [22]. Another loose definition is that the MIZ is the ice regime adjacent to OW where IC $< 70\%$ [22].

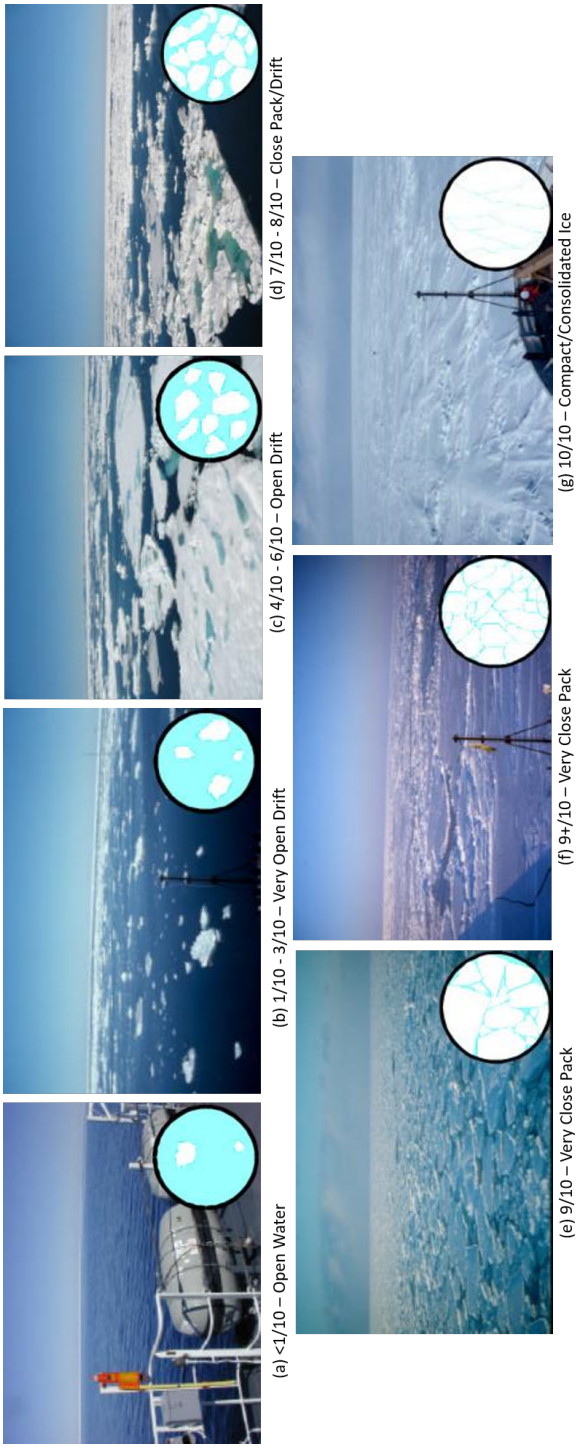

Figure 1.8: Ice concentration pictorials, per tenth coverage, showing photo and above view pictograph (adapted from [23])

1.6.2 Polynyas and Ice Arches

A polynya is a large area of OW that persists even when atmospheric temperatures are significantly below the freezing point. It is a Russian word which means "natural ice hole" [22]. In a polynya, ice is removed by melting or advection as soon as it is formed. This leaves the water surface exposed to the cold atmosphere, which then initiates reformation of new ice that will be removed again, and the process continues [22]. Therefore, polynyas are referred to as "ice factories" [22]. There are two main mechanisms for non-coastal polynya formation: first is thermodynamically driven by warm upwelling water that reaches the sea surface and prevents ice formation or melts newly formed ice; and the second is wind driven, where strong winds keep removing the new ice soon after formation, exposing the water surface to possible ice re-formation under cold air temperature [22]. During the winter months, polynyas create an ocean-to-atmosphere heat flux about two orders of magnitude higher than the surrounding ice pack [24]. Fig 1.9 shows an example of how the Lancaster Sound ice arch and polynya forms in a different geographical location from year to year. The location of the Lancaster Sound ice arch can vary by more than 500 km and even extend into Barrow Strait, significantly changing the area of the polynya [24]. An ice arch and polynya has formed every year in Lancaster Sound from 1979-2022, and in general, the ice arch forms in mid-February and collapses in late June [24].

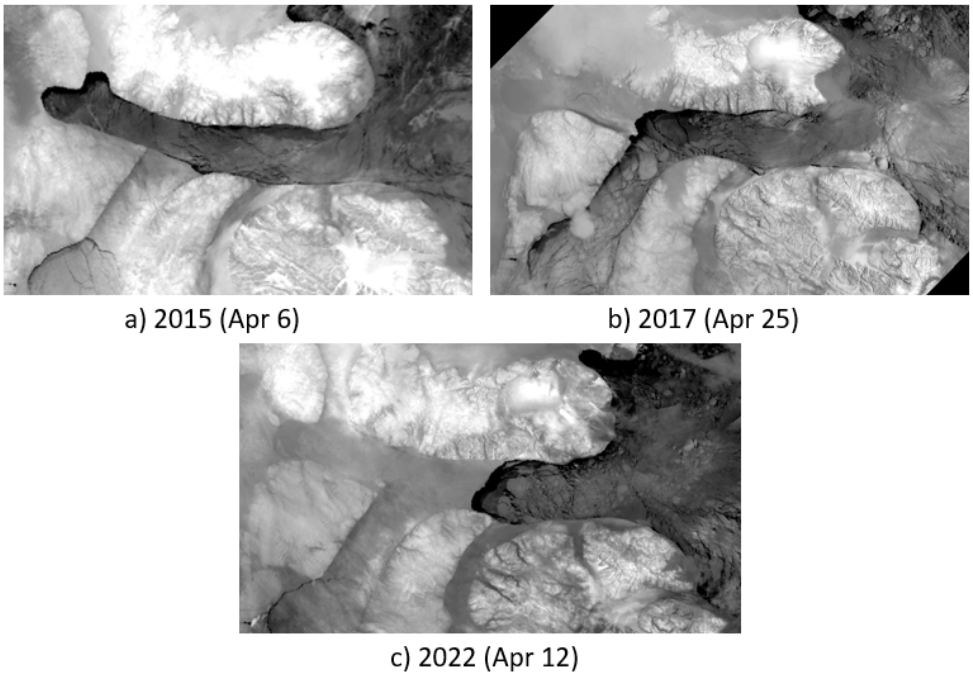

Figure 1.9: Example of Lancaster Sound ice arch and polynya formation in different geographical locations from year to year using satellite TIR imagery. Ice arch formed at the following locations: a) Resolute in 2015, b) Prince Leopold Island in 2017, and c) a location north of Arctic Bay in 2022.

1.7 Research Motivation

The Canadian Arctic is both strategically and tactically important for the Canadian Armed Forces and Canada as a whole, therefore studies in this region are operationally relevant. Polynyas in Lancaster Sound have been well studied over the past four decades [24], and accurate sea and ice surface temperature algorithms applicable to the Arctic Ocean environment have been developed [25–29]. However, TIR-based sea IC studies, especially those based on sea-surface and ice-surface temperature, are less prevalent. Therefore, research and development of a TIR-based IC algorithm, based on the Composite Arctic Sea Surface Temperature Algorithm (CASSTA) [29], and uses the Advanced Very High Resolution Radiometer (AVHRR) instrument, fills a gap in the literature. Such an IC algorithm could potentially provide more spatial resolution than passive microwave (PM) sources, more temporal

resolution than SAR sources, and be able to be generated rather quickly. The IC results would also allow recommendations to be provided for hydrophone and sonobuoy time of year deployment to support RMC's Audimus cubesat mission.

An IC algorithm, based on the CASSTA algorithm from [29], was used on non-cloudy AVHRR imagery to determine IC in Lancaster Sound. This algorithm provides a novel and rapid approach to analyzing IC in the arctic region. Further details are provided in the methodology in Chapter 2.

1.8 Research Goal

The goal of this research was to analyze the ice formation, retreat and concentration in Lancaster Sound between 2015-2024 inclusive, mainly based on MetOp AVHRR satellite images, and supplemented by Sentinel-1A/B and RADARSAT Constellation Mission (RCM) SAR satellite images. A TIR-based IC algorithm based on the CASSTA algorithm [29] was applied to the AVHRR images, and the accuracy of the IC trends were compared against published Canadian Ice Service (CIS) ice charts and PM satellite-based IC results. Once IC results were achieved, strategies and times of year for hydrophone and/or sonobuoy deployment within the waters of Lancaster Sound would be proposed, to contribute to RMC's Audimus cubesat mission.

1.9 Scope

The AVHRR CASSTA-based Ice Concentration (ACIC) applied in the research for this thesis was used on AVHRR satellite images of Lancaster Sound for 2015-2024 inclusive. Satellite image sources included MetOp-A, -B and -C AVHRR, Sentinel-1A/B SAR imagery for 2015-2019 inclusive, and RCM SAR imagery for 2020-2024 inclusive. RADARSAT-2 was not used, since access to RADARSAT-2 imagery was cost prohibitive. SAR images were obtained for days that were too cloudy for AVHRR image usage, when possible. AVHRR visible channel images were also used during warmer times of the year. Unsupervised isodata classification was used to determine IC, where possible, from SAR and AVHRR visible channel images. In addition, near concurrent AVHRR images of Lancaster Sound with MetOp-A, -B and -C were obtained to compare CASSTA and IC results, for substantiation of MetOp-B or MetOp-C CASSTA usage after November 2021, when MetOp-A ceased operations. ENVI remote sensing software version 5.7, using the *classic* interface display environment, was used for analysis. AVHRR imagery results

were also compared with the University of Bremen's PM-based Advanced Microwave Scanning Radiometer 2 (AMSR-2) IC results and CIS regional ice charts over the 2015-2024 research timeframe.

1.10 Thesis Outline

This thesis is comprised of five chapters. Chapter 2 details the data collection and methodology/processing techniques. This includes AVHRR-based and SAR-based satellite characteristics, previous AVHRR and SAR IC related research, ACIC algorithm accuracy assessment, previous melt/freeze related research, and specific research objectives. Chapter 3 details the results, which includes yearly ACIC results, 10-year averages, SAR results, ACIC algorithm accuracy assessment, and melt/freeze date determination. Chapter 4 is a discussion of the results, and Chapter 5 contains the conclusions, findings and recommendations.

2 Data Collection and Methodology

2.1 Satellite Remote Sensing Arctic SST Analysis

In 2019, the past 50 years of satellite remote sensing of SST was researched and reported [30]. SST obtained via Infrared (IR) is defined as skin SST, which is approximately the top 10 µms right below the ocean surface [30, 31]. SST derived from microwave frequencies is considered subskin SST, which is an integration of SST down to 1 mm below the ocean surface [30, 31]. These definitions are based on the universally accepted Group for High-Resolution SST (GHRSST) definitions [30,31]. The success of the application of satellite-derived SSTs to research and operational endeavours relies on an accurate and confident assessment of errors and uncertainties, which usually involves comparison with in-situ measurements. In such comparisons, the validating measurement has to be of greater accuracy and lower uncertainty than the satellite data [30]. In addition, satellite-derived SST retrievals have been validated using several approaches: satellite-derived SST compared with in-situ SST considered as a reference, three-way analyses using two satellite-derived SSTs and one in-situ SST, and a satellite-derived SST field compared to another satellite-derived SST field or an SST analysis [30]. The first two approaches aim to assess SST accuracy based on co-located coincident satellite and in-situ data (matchups), while the third approach may reveal defects or discrepancies undetected or hardly undetected using matchups [30].

Due to difficulties in access and the harshness of the conditions for both researchers and instruments in the Arctic Ocean, the area is poorly sampled by in-situ sensors, and thus a greater reliance is placed on satellite remote sensing [30]. Where sea ice exists, the underlying ocean mixed layer is generally at or very near to the freezing point, except in leads and polynyas on calm, sunny days when the ocean may become warm within a surface melt layer [27, 30].

SST in the Arctic has become more interesting, at least since approximately 2008 as ocean surface warming has become evident in many areas of the Arctic, with SST no longer remaining at or near the freezing point year-round [30]. However, remote sensing of SST in the Arctic Ocean can be challenging due to the frequent and extensive summer cloud cover which hides the surface from IR sensors, as well as the varying length of the sunlit part of the day during the year [30]. In sunlit conditions, measurements in the mid-IR window cannot be used because of scattering and reflection of sunlight, resulting in limited opportunities in summer for matchups with in-situ buoys at night, to generate atmospheric correction algorithm coefficients and assessing the accuracy of the derived SSTs [30]. As a result, these issues in the IR enhance the role of microwave SST products in this ROI, although their resolution is limiting, especially when OW is minimal during the early portion of the ice retreat season [30]. Since polar-orbiting satellites take many images per day of the Arctic, it could allow for a more detailed examination of diurnal warming and other processes, which have not yet been fully exploited [30]. It was concluded that deriving SST in seasonally ice-free Arctic waters is a new and relevant field [30].

2.2 MetOp Satellite and AVHRR Characteristics

2.2.1 AVHRR Characteristics

A common satellite instrument for measuring TIR is the AVHRR [32]. The AVHRR instrument has been in operation since 1978 on the National Oceanic and Atmospheric Administration (NOAA) Polar-Orbiting Environmental Satellites (POES), and is also onboard the European Organisation for the Exploitation of Meteorological Satellites (EUMETSAT) MetOp series satellites [33]. AVHRR was replaced on the POES series satellites by the Visible Infrared Imaging Radiometer Suite (VIIRS) instrument on the NOAA-20 mission [30], however AVHRR still remains operational on MetOp-B and MetOp-C.

For TIR, the measured parameter is emitted energy, which is a function of surface temperature and emissivity [32]. The emitted energy, expressed as the radiance received by the radiometer, is used as input to the Planck equation of radiation to find the surface temperature, assuming the emissivity of the surface is known [32]. For water, the emissivity value in the most-used thermal band of 10-12 µm is very high and stable at approximately 0.99, resulting in being able to obtain accurate measurements (to 0.1-0.2 K) of the water surface skin temperature [32]. Clear skies are required for TIR and visible channel observations.

Fig. 2.1 shows the AVHRR instrument that is aboard the MetOp satellites. The AVHRR instrument is an across-track scanner that senses Earth outgoing radiation from horizon to horizon, and uses an 8-inch diameter Cassegrain reflecting-type collecting telescope [34]. Cross-track scanning is achieved by a motor-driven continuously rotating scanning mirror. The scan mirror is oriented at 45° with respect to the axis of rotation to avoid variation in polarization effects across the swath [34]. The three IR detectors are cooled to 105 K by a 2-stage passive radiant cooler [34]. In-flight IR calibration is accomplished by a deep space view and an internal warm target temperature monitored to a precision better than 0.1 K [34].

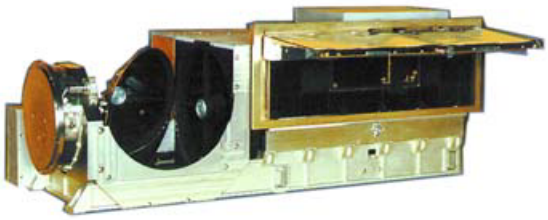

Figure 2.1: AVHRR/3 sensor onboard MetOp-A, -B and -C satellites [34]

Table 2.1 outlines the different channels/bands for AVHRR. The images in each channel are constructed by scanning the AVHRR field of view across the Earth's surface by a rotating plane mirror, with its surface inclined at 45° to its axis, which lies in the direction of flight [30].

Table 2.1: AVHRR specifications for NOAA and MetOp satellites - channel 3A added for AVHRR/3 (adapted from [24, 35])

Channel	Wavelength (µm)	Description	Satellites	Typical Use
1	0.58-0.68	Visible	All satellites	Daytime cloud & surface mapping
2	0.725-1.00	Near IR	All satellites	Land-water boundaries
3A	1.58-1.64	Near IR	NOAA-15 to -19 & MetOp series	Snow & ice detection
3B	3.55-3.93	Middle IR	NOAA-8 to -19 & MetOp series	Night cloud mapping; SST
4	10.30-11.30	Thermal IR	All satellites	Night cloud mapping; SST
5	11.50-12.50	Thermal IR	NOAA-8 to -19 & MetOp series	SST

2.2.2 MetOp Satellites

The MetOp series are sun-synchronous polar orbiting satellites, which circle the earth approximately 14 times per day, and contain the AVHRR instrument, amongst other equipment [36]. The MetOp satellites operate at an altitude of 817 km, and are European Union satellites used in operational weather forecasting [36]. MetOp-A was launched in October 2006, MetOp-B in September 2012, and MetOp-C in November 2018 [36]. MetOp-A was decommissioned in November 2021, MetOp-B is expected to operate until 2027, and MetOp-C is expected to operate until 2030 [36]. MetOp-A and -B were launched into the same orbital plane, while MetOp-C was launched in an orbital position about 120° apart from the other two [36].

Spatial resolution for AVHRR MetOp satellites at nadir, the point on the earth directly below the satellite, is 1.1 km, degrading to approximately 8 km at the edge of the swath [24]. The width of each swath is approximately 2700 km [30]. AVHRR data has been used in discriminating sea ice from OW, estimating sea and ice surface temperature, and melt ponds on ice, among other applications [22].

2.3 AVHRR Images Sources and Processing

2.3.1 Image Sources

Daily AVHRR images for 2015-2024 inclusive were obtained from the NOAA Comprehensive Large Array Data Stewardship System (CLASS) website [37]. MetOp-A, -B and -C satellites were selected, even though AVHRR was present on NOAA satellites up to NOAA-19, which was decommissioned in 2025 [38]. This was due to recent CASSTA work [29] using MetOp-A, and MetOp-C is expected to be in operation until 2030 [36]. To select images, the following steps were used:

1. AVHRR was selected from the top dropdown menu;
2. In the Spatial section, Region of Interest was selected as Lancaster Sound on the map;
3. In the Temporal section, date range and time of day range were selected;
4. In the Advanced Search Criteria, the selected datatype was Full Resolution Area Coverage (FRAC) 1 km Level 1B. For node, both ascending and descending passes were selected. For receiving station, Svalbard was selected. For satellite, MetOp-A, -B and -C were selected; and
5. An example of the format of an AVHRR image name from NOAA CLASS is: NSS.FRAC.M2.D19014.S1643.E1824.B6350506.SV, where FRAC is Full Resolution Area Coverage, M2 is MetOp-A (M1 is MetOp-B and M3 is MetOp-C), the date is 2019 day 014, the time of day is 1643 GMT, and the very last part means that the image was downlinked at Svalbard.

MetOp-A images were obtained from January 2015 - November 2021, when MetOp-A was phased out. MetOp-A was concentrated on since the CASSTA SST algorithm [29] was developed using it. During 2020 and 2021, MetOp-A, -B and -C were obtained for the purposes of comparing the three. For 2022-2024, MetOp-B images were obtained, as well as some MetOp-C. The time of day for image selection was on average between 00:00-03:30 Greenich Mean Time (GMT), or between 22:00-24:00 GMT. The ground station that processed the images was located at Svalbard, Norway. Svalbard is an island archipelago in the Barents Sea, north of mainland Norway. Obtaining the images in Level 1B format meant that the data had basic radiometric calibration to radiance values, as well as basic geometric correction.

ENVI version 5.7 software, using the *classic* interface display environment, which is a remote sensing image analysis and processing software made by NV5 Geospatial Software [39], was used to view and analyze AVHRR and SAR satellite images.

2.3.2 Image Selection and Pre-processing

The daily AVHRR images were observed in ENVI using channel 4 (TIR), and images that had clouds obstructing the Lancaster Sound ROI, or if the ROI was too close to the edge of the image, were removed. There were more non-cloudy images in the winter months than the summer months, for the times of day observed. Overall, 9010 AVHRR images were obtained and reviewed manually for the 10-year period, with a breakdown as per Table 2.2. Table 2.3 shows the number of assumed non-cloudy days per year, based on the observed times of day where the images showed the ROI as non-cloudy. An overall decreasing trend in assumed non-cloudy days per year was observed from the data in Table 2.3, with 2020 and 2021 being especially low in number of assumed non-cloudy days. The average number of assumed non-cloudy days per month over the 2015-2024 period, after checking each day in the 10-year period during 00:00-03:30 GMT and/or 22:00-24:00 GMT, are provided in Table 2.4. Some of the months in the May-September timeframe had as low as 0-3 assumed non-cloudy days per month based on the observed times of day, depending on the month and year. Table 2.5 also shows how the number of multiple-day streaks of non-cloudy days have reduced between 2015-2024.

Each selected AVHRR image was calibrated and geo-referenced in ENVI before additional SST analysis was completed on the image. The calibration converted the radiance data for channels 4 and 5 to brightness temperatures in degrees Kelvin, and the geo-referencing corrected for earth surface curvature and aligned the image to the Universal Transverse Mercator (UTM) map. Generally, presence of cloud cover could be determined using the TIR images, however, one additional method of identifying clouds was to apply band math of $b3\text{A}/b1$ (Near IR (NIR) channel 3A/Visible channel 1) on an AVHRR calibrated image in ENVI, because the clouds show up brightly and everything else appears darker, though it only worked if there was some solar illumination. The $b3\text{A}/b1$ method has been used previously [40].

Table 2.2: Number of AVHRR images of Lancaster Sound reviewed per year, 2015-2024

Year	# of Images Obtained*	MetOp Satellite
2015	824	A
2016	858	A
2017	784	A
2018	758	A
2019	739	A
2020	1522	A,B,C
2021	1347	A,B,C
2022	694	B,C
2023	557	B,C
2024	927	B,C

*Images observed within 00:00-03:30 GMT and/or 22:00-24:00 GMT.

Table 2.3: Number of assumed non-cloudy days per year in Lancaster Sound, 2015-2024, based on the review of available AVHRR images

Year	# of Non-Cloudy Days*
2015	197
2016	161
2017	141
2018	154
2019	109
2020	51
2021	42
2022	123
2023	127
2024	106
Avg	121

*Days assumed non-cloudy based on the 00:00-03:30 GMT and/or 22:00-24:00 GMT observed image times.

Table 2.4: Average number of assumed non-cloudy AVHRR days per month in Lancaster Sound, 2015-2024

Month	Average # of Non-Cloudy Days*	Standard Deviation (Days)
Jan	16.2	5.0
Feb	16.7	7.1
Mar	17.2	7.0
Apr	11.4	7.1
May	6.2	4.1
Jun	7.6	2.5
Jul	8.7	5.3
Aug	5.6	4.5
Sep	3.1	3.1
Oct	4.0	3.3
Nov	9.8	5.8
Dec	14.6	7.0

*Days assumed non-cloudy based on the 00:00-03:30 GMT and/or 22:00-24:00 GMT observed image times.

Table 2.5: Multi-day streaks of assumed non-cloudy AVHRR days for each year in Lancaster Sound, 2015-2024

Year	Multi-Day Streaks* of Non-Cloudy Days** (Calendar Day # Range and Month)
2015	21-31 Jan
	41-54 Feb
	61-69 Mar
	91-104 Apr
	311-316 Nov
	335-341 Dec
	351-362 Dec
2016	1-10 Jan
	22-30 Jan
	42-52 Feb
	71-90 Mar
	174-178 Jun
	183-188 Jul
	220-227 Aug
	344-350 Dec
2017	25-30 Jan
	31-47 Jan/Feb
	53-59 Feb
	74-84 Mar
	311-318 Nov
2018	27-31 Jan
	71-84 Mar
	93-98 Apr
2019	47-53 Feb
2020	none
2021	none
2022	106-110 Apr
2023	90-97 Mar/Apr
2024	20-27 Jan
	79-85 Mar

*MetOp satellite images reviewed: 2015-2019 was MetOp-A, 2020-2021 was MetOp-A/B/C, and 2022-2024 was MetOp-B/C.

**Days assumed non-cloudy based on the 00:00-03:30 GMT and/or 22:00-24:00 GMT observed image times.

2.4 AVHRR-based CASSTA Algorithm

2.4.1 CASSTA History

The work of [41, 42] is considered the pioneering basis of satellite-based SST estimates. Even though these algorithms [41, 42] were made for open ocean in temperate latitudes, they were used as a starting basis for Arctic SST work [27]. Other work that was important to the original CASSTA algorithm development, especially the ice surface temperature (IST) component, included [25, 26]. The original CASSTA was developed to accurately determine high latitude surface temperature in three different regimes: seawater, ice and MIZ [27], and is considered more accurate than the National Aeronautics and Space Administration (NASA) and NOAA's Pathfinder program SST retrieval system in the Arctic [43], where high brightness temperature differences between the 11 µm and 12 µm channels, BTD_{11-12}, are not indicative of atmospheric water vapour [27]. The original CASSTA was developed using AVHRR data from the NOAA-12 satellite [27].

The work of [27] was built upon by using a MetOp AVHRR Arctic Surface Temperature product, which is an integrated Ice Surface Temperature (IST), MIZ temperature and high-latitude/SST product [28]. The developed algorithm was compared with in-situ observations in the Arctic Ocean using drifting buoys and ships. Overall, it was concluded that because of the scarcity of conventional surface temperature or surface air temperature data in the Arctic at that time, the satellite IST data with its relatively good coverage could potentially add valuable information to model analysis for the Arctic atmosphere [28].

2.4.2 Single-Channel CASSTA Algorithm Description

In 2019, the original CASSTA work [27] was improved using a single-channel IST estimator in place of the CASSTA split window IST algorithm [29]. The Single-Channel CASSTA is applicable to SST, IST and MIZ in the Arctic [29]. This improved algorithm benefited from new in-situ sea ice data in 2011, through the Qaanaaq sea ice thermal emission experiment, on the east side of the North Open Water (NOW) polynya [29]. Based on comparison of CASSTA AVHRR data with the 2011 in-situ data, the revised single-channel IST solution is shown in Eqn 2.1. Although the original and Single-Channel CASSTA were developed using AVHRR from the NOAA-12 satellite, channel 4 brightness temperature spectral responses for NOAA-12 and MetOp-A were nearly identical and have been used interchangeably in previous research [29].

$$IST = 3.062524 + 0.997598(BT_{11}) \tag{2.1}$$

The mean average error of the single-channel IST was 0.283 K, with a standard deviation of 0.210 K, as opposed to the split window IST algorithm, which had a mean absolute error of 0.965 K with a standard deviation of 0.809 K [29]. This means that the 12 µm AVHRR channel, channel 5, was not required for the Single-Channel CASSTA. When the single-channel IST was then used in the overall revised Single-Channel CASSTA, minor error reductions were determined for both the ice regime and MIZ regime [29]. Two other studies [44, 45] also found increased accuracy when using a single-channel IST algorithm for TIR sensors when observing the arctic maritime environment [29].

There are some considerations when applying the Single-Channel CASSTA. First, cloud-free conditions are required for accurate thermal mapping, which is true for all satellite surface temperature algorithms using TIR. The arctic maritime environment is very cloudy, with persistence of stratus clouds during the warmer months [29]. Second, $BTD_{11-12} > 2.0^{\circ}$ C is indicative of ice fog, which commonly occurs during colder months in the vicinity of ice leads [29]. Ice fog occurs under apparent clear sky conditions and prevents accurate surface temperature assessment. Third, unrealistic results occur when $BTD_{11-12} < 0^{\circ}$ C, where negative values indicate the presence of mineral dust aerosols [46]. Fourth, sensor zenith angles $< 45^{\circ}$ will generally yield better results, because high sensor zenith angles result in decreased emissivity of snow and ice in the BT_{11} band due to the non-Lambertian nature of snow/ice [27]. A summary is presented in Table 2.6.

Table 2.6: Considerations for using CASSTA or Single-Channel CASSTA (adapted from [29])

Consideration	Comment
Cloud	Cloud free conditions required.
$BTD_{11-12} > 2.0\,^{\circ}$C	Indication of ice fog. Inaccurate surface temperature returned.
$BTD_{11-12} < 0\,^{\circ}$C	Indication of dust. Inaccurate surface temperature returned.
Sensor Zenith Angle	Sensor zenith angle $< 45^{\circ}$ for best results.

The Single-Channel CASSTA equation is formed using three eqns from [29], used during different conditions. The brightness temperature variable BT_{11} in [29] is channel/band 4, which is approximately 11 µm in the TIR

range. The variable BT_{12} corresponds to channel/band 5, which is approximately 12 µm in the TIR range. Within ENVI, BT_{11} corresponds to $b4$ and BT_{12} corresponds to $b5$. Eqn 2.2 is for the Arctic ocean region, where ASST is Arctic SST. It was determined that a single channel ASST was most applicable [27]. The small amount of atmospheric absorption in the BT_{11} regime is accounted for in the a and b coefficients, and hence calculation of the difference between BT_{11} and BT_{12}, which is $BTD_{11\text{–}12}$, is not required [29].

$$ASST = a + b(BT_{11}) \tag{2.2}$$

The coefficients a and b for Eqn. 2.2 are then taken from Eqn 5 from [27], and -273.15 is added to put the equation in °C, resulting in Eqn. 2.3:

$$ASST = -4.012372 + 1.016284(BT_{11}) - 273.15 \tag{2.3}$$

Eqn. 2.4 is for the IST region, and also only requires BT_{11}, where other factors have been built into the coefficients, based on improved analysis on the original CASSTA IST using in-situ data results [29]:

$$IST = 3.062524 + 0.997598(BT_{11}) \tag{2.4}$$

Eqn. 2.5 is for the MIZ Surface Temperature (MIZST) region. This portion of the overall Single-Channel CASSTA equation falls between the ASST and IST, so it uses a weighted average, with the result in °C. The ASST temperature limit is 270.95 K (-2.2° C), and IST temperature limit is 268.95 K (-4.2° C).

$$MIZST = [(BT_{11} - 270.95)(-0.5)IST] + [(BT_{11} - 268.95)(0.5)ASST] \tag{2.5}$$

Now, the Single-Channel CASSTA is combined in Eqn 2.6 using the single-channel IST instead of a split window IST. Therefore, when $BT_{11} > 270.95$ K, ASST (Eqn. 2.3) is used. When $268.95\,\text{K} \geq BT_{11} \leq 270.95$ K, MIZST (Eqn 2.5) is used. When $BT_{11} < 268.95$ K, IST (Eqn. 2.4) is used. To get the temperature in °C, 273.15 is subtracted from the whole CASSTA eqn once it has been combined in Eqn. 2.6.

$$\begin{aligned} CASSTA_{SingleChannel} = [&((BT_{11} < 268.95)(IST))+ \\ &((268.95 \geq BT_{11} \leq 270.95)(MIZST))+ \\ &((BT_{11} > 270.95)(ASST))] - 273.15 \end{aligned} \tag{2.6}$$

2.4.3 Applicability to this Research

The Single-Channel CASSTA is applicable for monitoring climate change, contributing to climate models, and, when fused with other sensors such as SAR, could be an aid in determining the composition of ice surface types for arctic shipping or naval operations [29]. The Single-Channel CASSTA using MetOp AVHRR satellite data has been previously applied to Lancaster Sound polynya [24] and NOW polynya [47] research. This algorithm forms the basis of the ACIC used in the research reported for this thesis. From here on, any reference to CASSTA implies the improved Single-Channel CASSTA, unless the original form is specified.

2.4.4 CASSTA Analysis Method

CASSTA [29] was applied to the selected non-cloudy AVHRR images of Lancaster Sound obtained from NOAA CLASS, after they were calibrated and geo-referenced in ENVI, to create SST images. In addition, since the CASSTA was developed for MetOp-A, applicability to MetOp-B and MetOp-C images had to be verified.

CASSTA was applied in ENVI as follows:

1. MetOp AVHRR grey scale image first calibrated, then geo-referenced using UTM Zone 17.
2. CASSTA algorithm, *CASSTA MetOp A.exp*, employed using Basic Tools / Band Math function, where $b4$ was selected (band 4) for the already calibrated/geo-referenced image.
3. The resulting new image was then shown in pseudocolour using Tools / Colour Mapping / Density Slice function. The *M30_0.dsr* scale was restored and applied, which is a lookup table assigning temperatures (between 0°C and -30°C) to brightness temperatures; and
4. Then the *Baffin Bay.evf* coastlines outline was applied using the Vector / Open Vector File function.

When generating CASSTA images, temperature scales from -30°C to 0°C were used, with an occasional range of -20°C to 0°C for warmer parts of the year in late May or early June. The range of SSTs were mapped to a colour spectrum that was then applied to the images.

Ice fog checks were completed before deciding if a specific day was useful for CASSTA image formation. The presence of ice fog corrupts surface temperatures and is almost impossible to detect on visible or infrared bands/channels. Ice fog checks were conducted on CASSTA images in ENVI as follows:

1. MetOp AVHRR grey scale image first calibrated, then geo-referenced using UTM Zone 17.

2. Basic Tools / Band Math function using $b4-b5$ (BTD_{11-12}) was applied, where $b4$ was band 4 and $b5$ was band 5 of the calibrated/geo-referenced AVHRR image.
3. Then the image was shown in pseudocolour using Tools / Colour Mapping / Density Slice function and used the following colour assignments: red for a range of 2 to 10, green for a range of 1-2, and blue for a range of -10 to 1. All other colours from the look up table were deleted. Any ice fog, shown by $BTD_{11-12} > 2.0$°C appeared as red; and
4. Then the *Baffin Bay.evf* coastlines outline was applied by using the Vector / Open Vector File function.

2.4.5 Comparison of MetOp-A/B/C using CASSTA

CASSTA was developed for MetOp-A, however, MetOp-A ceased operating by December 2021. Therefore, an analysis of the similarity of the results using MetOp-B and MetOp-C was required to apply CASSTA to the AVHRR images from December 2021 to December 2024 inclusive. Near-concurrent images of the three satellites were obtained for the years 2020 and 2021, and then this selection was reduced due to filtering out cloudy images. The months with the most non-cloudy images for all three satellites were February 2020 (9 days), March 2020 (6 days) and June 2020 (4 days). An analysis was done for a selected day for all three months to see if there were any differences based on time of year. Not all three satellite passes had Lancaster Sound at the same incidence angle, which was a good test for the CASSTA algorithm. For February, calendar day 44 (Feb 13) was chosen. The MetOp-A, -B and -C images were taken at 0:13, 0:44 and 0:41 GMT respectively. For March, day 67 (Mar 6) was chosen. The MetOp-A, -B and -C images were taken at 0:37, 0:56 and 1:05 GMT respectively. For June, day 168 (Jun 16) was chosen. The MetOp-A, -B and -C images were taken at 0:48, 1:07 and 1:16 GMT respectively.

The Change Detection/Compute Difference Map function in ENVI was used to quantitatively compare the MetOp-A, -B and -C images, along with reviewing the change detection statistics. The difference was computed by subtracting the initial state image from the final state image, and the classes were defined by change thresholds. A positive change identified pixels that became brighter, while a negative change identified pixels that became dimmer. Percent difference and 5 classes were selected as the comparison parameters. The resulting Difference Map classification image was colour coded to indicate the magnitude of the change between the two images. Positive changes displayed in shades of red, grading from grey for no change to bright red for

largest positive change. Negative changes displayed in shades of blue, grading from grey for no change to bright blue for the largest negative change. This process compared the two images pixel for pixel. If the percent difference was deemed small enough, then the CASSTA was also considered applicable to MetOp-B and MetOp-C images. Solar zenith angle was not corrected for, and use of Lancaster Sound near the edge of the image swath for the MetOp-A and MetOp-C images allowed for testing the limits at maximum sensor zenith angles. These images at the edge of an AVHRR swath were spot checked for sensor zenith angle in ENVI using the following method:

1. Opened a MetOp AVHRR grey scale image, uncalibrated and not georeferenced;
2. Used Basic Tools / Preprocessing / Data-Specific Utilities / AVHRR / Build Geometry File;
3. Selected the image, then selected sensor zenith angle (solar zenith angle is also an option);
4. Output the result to memory in a new display, and linked the resulting display to the original image; and
5. Used the Cursor Location/Value to determine the senzor zenith angle across the image.

2.5 AVHRR CASSTA-based IC (ACIC)

2.5.1 Previous AVHRR-based IC Research

One of the first studies on IC algorithms using AVHRR satellite imagery analyzed images from June/July 1984 in Fram Strait, located between Greenland and Svalbard, Norway [48]. Results were compared with previous aircraft-based SAR and PM radiometer imagery, coincident aerial photography, and photometer measurements from helicopters [48]. Due to the 1.1 km resolution of AVHRR, only ice floes and leads with size scales greater than 1.1 km were visible in the images. The sensitivities of the five AVHRR channels to distinguish clouds from OW and ice cover were employed in a developed algorithm [48]. Since the algorithm relied heavily on the visible and NIR channels, it was determined to be suitable for seasons in polar regions with sufficient sunlight [48]. IC for AVHRR reflectance data using pixelwise correction for solar zenith angle was recommended to obtain consistent estimates [48].

AVHRR satellite data and algorithm developed by the EUMETSAT Ocean & Sea Ice Satellite Application Facility was then used to determine ice/water differentiation in the Svalbard, Norway, Scandinavia, and eastern Greenland

regions [33]. AVHRR channels 1-4 were used in various ratios, a Bayes theorem was used to form the basis of the algorithm, and results were compared with RADARSAT-1 data [33].

Investigation of AVHRR satellite data for IC analysis was conducted in the Canadian Arctic [40]. During winter, reflectance cannot be used in high latitude regions because of low solar illumination [40]. However, the data set used late April to early May in the Canadian Arctic, so some sunlight was present for the study [40]. Four different AVHRR channel combinations were attempted: channel 1, the ratio between channel 2 and 1, the ratio between channel 3A and 1, and the difference between channel 4 brightness temperature and the 2 m surface air temperature [40]. Important differences between the details observable using each channel are: channels 1 (visible) and 2 (NIR) both have good separability between ice and water and hence can discriminate between the two under cloud-free conditions; channel 3A (Short-Wave Infrared (SWIR)) shows clouds with high reflectance, and ice and OW with low reflectance, meaning channel 3A is a good discriminator between clouds and ice/OW; and channel 4 (TIR) is used to measure sea skin temperature and can provide discrimination between ice, water and clouds even in low solar illumination conditions [40]. The study recommended more accurate calculation of surface temperature using a split-window technique, as well as including channel 3B (SWIR) for which reflectance data are less sensitive to ice thickness and surface melt. In addition, due to the April/May time of year observed, potential meltwater on top of the ice would lower the reflectance, in particular the channel 1 reflectance, bringing the value closer to that of OW. As a result, such areas could have been incorrectly classified as OW in the model used [40].

A sea IC comparison using AVHRR and PM, using four different previously established PM algorithms was conducted: Comiso Bootstrap, Cal/Val, NASA Team, and NASA Team 2 [49]. These algorithms used data from the 19 GHz, 37 GHz and/or 85 GHz channels. AVHRR channels 2 (VNIR) and 4 (TIR) data were used. The PM source was the Special Sensor Microwave/Imager (SSM/I), a precursor to the AMSR series, with half the spatial resolution of the newer instruments. Three study areas were used: Baffin Bay, Barents Sea, and Greenland Sea, for a summer period of June-August 2001 and a winter period of November 2001 - March 2002. A threshold method (a pixel is either 100% ice or 100% water) from channel 4 was used during winter, and a mixing method (a pixel has an IC of 0 to 100%) from channel 2 was used during summer [49]. The threshold temperature used was 271 K (-2.15° C), where any pixels below this temperature were identified as ice. It was concluded that the NASA Team, Comiso Bootstrap, and NASA Team 2 SSM/I-based

algorithms tended to underestimate IC, particularly during summer, while Cal/Val tended to overestimate IC, also particularly during summer [49].

2.5.2 ACIC Analysis Method

IC images were generated in ENVI using the ACIC, which was applied to images that had CASSTA already implemented. During colder months in the Arctic region, open sea water is at -1.8° C. The surrounding snow/ice pack will tend to be the same as the 2 m surface air temperature [50]. In an image, if the the snow/ice pack is -30° C and the CASSTA is showing -18°C, the algorithm compares the difference between what the temperature would be if it was completely frozen (-30° C in this case) and if it was OW (-1.8° C) and gives a percentage of OW in that pixel. The relationship between the two temperatures is linear. Based on the comparison check of the MetOp-A, MetOp-B and MetOp-C CASSTA results, the ACIC was applicable to all three satellites. Eqn 2.7 is the equation used for calculating ACIC for MetOp AVHRR images that have already had the CASSTA applied (see also the related Technical Note [51] in Appendix A). IC is calculated in tenths, ranging between 0/10 to 10/10. The value of $b9$ is replaced with the mean temperature in ° C of the pixels of the selected snow/ice pack area in the image. The value of $b1$ is the CASSTA result for the specified image.

$$IC = \left[\frac{(b1 + 1.8)}{(b9 + 1.8)}\right] (10) \tag{2.7}$$

The ACIC was applied in ENVI as follows:

1. MetOp AVHRR grey scale image first calibrated, then geo-referenced using UTM Zone 17;
2. CASSTA algorithm employed using Band Math function, then the image was shown in pseudocolour using Tools / Colour Mapping / Density Slice function. The *M30_0.dsr* scale was restored and applied, which is a lookup table assigning temperatures to brightness temperatures (between 0°C and -30°C). No coastlines were applied;
3. The cursor was placed on a snow/ice pack region close to OW. Then the Tools / Spatial Pixel Editor function was used, and all the cells in the array, which was approximately 50 x 50 pixels, were highlighted and replaced with the mean value calculated by ENVI;
4. Using the Band Math function, the *Ice Concentration.exp* equation file was selected, and band 9 ($b9$) was replaced by the mean value from the previous step. The CASSTA image was selected for $b1$. Then the resulting image was opened in a new Display; and

5. Using Tools / Density Slice, the *Ice Concentration.dsr* lookup table was restored and applied. The lookup table maps a continuous colour spectrum to IC gradations from 0 to 10. Then the *Baffin Bay.evf* coastlines outline was applied using the Vector / Open Vector File function. The ACIC reports IC in tenths coverage (i.e. 0/10 is no ice while 10/10 is fully covered by ice).

The ACIC was only accurate during part of the year, when the SST was still cold enough. The $b9$ limit was determined via analysis, and accuracy could also be confirmed via visual inspection of the resulting ACIC image and its comparison of ice/water characteristics to the corresponding geo-referenced TIR image. The workable limit for $b9$ was determined during image analysis to be $<$ -3° C on the ice pack. Once $b9 >$ -3° C, this corresponded to SST $>$ -1.8° C.

2.6 SAR Satellite Characteristics

2.6.1 General

Spaceborne C-band SAR satellites such as Sentinel-1A/B and RCM, used for the research for this thesis, can provide high-resolution and wide swath Arctic sea ice observations, and have the potential to provide more accurate and detailed sea ice information than is possible from radiometer or scatterometer sensors [52]. The C-band has a frequency range of 4-8 GHz [53]. Both Sentinel-1A/B and RCM are at 5.405 GHz, which corresponds to approximately 5.55 cm wavelength. The wavelength determines how the radar signal interacts with the surface and how far a signal can penetrate into a target [53].

SAR satellites can operate in various polarizations. Typically, they transmit linearly polarized [53]. Horizontal polarization is denoted by the letter H, and vertical by the letter V. Polarizations can be different on the transmit signal path and the receive signal path. For example, a signal emitted in V by the satellite and received in H would be denoted VH. There are also HH, VV, VH and HV combinations. Each of these combinations provide different information about the structure of the surface being imaged, based on the following types of scattering: rough surface, volume, and double bounce [53]. Surface scattering and volume scattering are the main interactions between SAR waves and sea ice [54]. SAR sensors can penetrate clouds, dry ice cover and snow due to its relatively long wavelength [54].

2.6.2 Sentinel-1A/1B

Sentinel-1A became operational in October 2014, and Sentinel-1B in 2016 [54–56]. Each Sentinel-1 satellite has a revisit time of 12 days, or six days overall if both satellites are used for the exact same pass [32]. The satellites operate at an altitude of 693 km [57]. Sentinel-1A and -1B SAR data are frequently used in sea ice research and operational applications because the European Space Agency (ESA) and European Commission's policies have made data free for registered users [32, 54].

Four modes are available on the Sentinel-1 satellites: StripMap (SM), Interferometric Wide Swath (IW), Extra-Wide Swath (EW) and Wave (WV). IW and EW are most useable in sea ice applications [32]. Specifications are provided in Table 2.7. Both IW and EW offer single polarization (HH or VV) or DP (HH+HV or VV+VH) [32].

Table 2.7: Sentinel-1 imaging beam modes characteristics [32, 58]

Imaging Beam Mode	Nom. Res. (m)	Swath Width (m)	Noise Floor (dB)
Extra Wide (EW)	20 x 40	410	-22
Interferometric Wide (IW)	5 x 20	250	-22
StripMap (SM)	5 x 5	80	-22
Wave (WV)	5 x 5	80	-22

2.6.3 RADARSAT Constellation Mission (RCM)

Launched in June 2019, the RCM aims to ensure continuity of operational SAR imagery for RADARSAT-2 users, as well as drawing from the constellation approach to enable new applications [59]. Together, the three RCM satellites provide a four-day exact revisit, allowing coherent change detection. The constellation configuration consists in flying three C-band SAR satellites evenly spaced at 120° on the same orbit. The satellites operate in a sun-synchronous polar low-earth orbit, at an altitude of approximately 600 km, translating into the satellites following each other by 30 minutes [59]. Marine surveillance applications, including sea ice monitoring, is one of the core RCM applications [60]. RCM was also expected to fulfill the need for operational sea ice monitoring by the CIS [60]. The various RCM beam modes are provided in Table 2.8.

RCM also includes the ability to steer the receive beam in elevation in discrete steps during the receive window. This improves SAR imaging performance by reducing the Noise-Equivalent Sigma-Zero (NESZ), which is the

noise floor of an image, as well as the range ambiguity levels compared to conventional operation with a fixed beam position during the receive window. This capability provides the most improvement in wide swath cases, and thus, it is used operationally in all the ScanSAR modes of operation [59]. RCM provides multiple polarization modes, which use a compact polarimetric (CP) architecture, a major technological improvement in in-orbit earth-observing SAR satellites [60].

Since the launch of RCM, the main RCM modes used for Canadian Arctic sea ice have been: ScanSAR 50 m (SC50M) and ScanSAR Low Noise (SCLN), both with HH-HV DP and 350 km swath size [61]. ScanSAR 100 m (SC100M) with 500 km swath size and HH-HV polarized, has been used for the Eurasian part of the Arctic [61]. Noise floor maps in both SC50M and SC100M exhibit scalloping patterns due to one look in the azimuth direction, whereas in SCLN no scalloping pattern is present due to two looks in the azimuth direction [61].

Table 2.8: RCM imaging beam modes characteristics (adapted from [60])

Imaging Beam Mode	Nom. Res. (m)	Swath Width (km)	# of Looks (rng x az)	Noise Floor (dB)
Low Res. 100 m (SC100M)	100	500	8 x 1	-22
Low Noise (SCLN)	100	350	4 x 2	-25
Ship Detection (ScanSAR mode)	Variable	350	Variable	Variable
Med. Res. 50 m (SC50M)	50	350	4 x 1	-22
Med. Res. 30 m (SC30M)	30	125	2 x 2	-24
Med. Res. 16 m (StripMap)	16	30	1 x 4	-25
Quad-Polarization (StripMap)	9	20	1 x 1	-25
High Res. 5 m (StripMap)	5	30	1 x 1	-19
Very High Res. 3 m (StripMap)	3	20	1 x 1	-17
Spotlight	1 (az) x 3 (rng)	5	1 x 1	-17

2.7 SAR Images Sources and Processing

2.7.1 Sentinel-1A/1B Images Source

Sentinel-1 SAR images were downloaded using the ESA's Copernicus Open Access Hub for 2015-2019 [62]. Access to Sentinel imagery was possible once a free account was created. The Sentinel images used were Level 1 Ground Range Detected (GRD), in HH decibel γ^0 polarized format and already orthorectified. The decibel γ^0 displays a grayscale visualization of the γ^0 of the HH polarization, and also represents backscatter radiometrically terrain-corrected to account for topographic variations. The HH polarization is less sensitive to surface roughness compared to the VV polarization, and it provides good contrast between water and land surfaces [62]. Compared to the

linear γ^0 visualization, the decibel γ^0 visualization includes a logarithmic scaling of the data [62]. In addition, the Sentinel-1 HH polarized images provided more ice detail and contrast than the HV polarized images. The majority of the images were from the EW mode, though a few IW mode images were also used. Sentinel-1 image time of day ranges over Lancaster Sound were approximately 12:00-13:00 GMT and 22:00-24:00 GMT, though the daily decibel γ^0 composite images were used instead for the main analysis.

The year 2015 was chosen as the starting point for the 10-year study, since Sentinel-1A only became operational in October 2014 [56]. Sentinel-1 images were obtained for the cloudy days during 2015-2019, mostly centred on the weekly CIS ice chart dates where there were AVHRR image gaps.

2.7.2 RCM Images Source

RCM SAR images were downloaded from the National Resources Canada Earth Observation Data Management System (EODMS) for 2020-2024 [63]. RCM images were obtained in GEOTIFF format, and were already calibrated and geo-referenced. The polarizations provided in the RCM image downloads were HH and HV. The metadata for the images were provided in accompanying text files [64]. RCM images were obtained for the cloudy days during 2020-2024, mostly centred on the weekly CIS ice chart dates where there were AVHRR image gaps. The HH polarized RCM images provided better ice detail and contrast than the HV polarized images. RCM image time of day ranges over Lancaster Sound were approximately 12:00-13:00 GMT and 22:00-24:00 GMT.

2.7.3 Image Selection and Pre-processing

Substantial numbers of Sentinel-1 and RCM images were downloaded, however in general, they were only analyzed if they filled a gap in the AVHRR weekly intervals for the 2015-2024 research period. Overall, 60 Sentinel-1 images were used for gap-filling in 2015-2019, and 46 RCM images were used for gap-filling in 2020-2024. Due to the smaller swath widths of SAR images (410 km for Sentinel-1 EW and 500 km for RCM SC100M) as compared to AVHRR (2700 km), the entire Lancaster Sound ROI did not appear in many of the SAR images.

Sentinel-1 HH JPG files were used in ENVI. The Sentinel-1 Level 1 GRD images were generated using a multi-look format, which provided some speckle reduction in the image, but phase information was lost. They were also already

projected to ground range. The pixels were square with reduced speckle at a cost of reduced spatial resolution [62].

RCM HH TIF files were processed in ENVI. The RCM images were in GRD format, and did not require pre-processing, as they were already calibrated and geo-referenced from EODMS.

2.8 Other IC Data Sources used for Comparison

2.8.1 Canadian Ice Service (CIS) Ice Charts

The CIS creates weekly regional ice charts for the Eastern Arctic [65, 66]. IC data is presented in tenths in Egg Code format. The World Meteorological Organization (WMO) Egg Code describes IC and ice type in a section of an ice chart [66, 67]. CIS ice charts show the analysis of ice conditions for a given region and are released on Mondays [65]. They are based on an analysis and integration of data from satellite imagery such as SAR imagery in linear polarization, weather and oceanographic information, and visual observations from ships and aircraft [60,65]. Satellite imagery is collected over a few days to have complete coverage of the area [65]. No widely published specific spatial resolution is identified for the regional ice charts, though one study reported it as 1 km [68]. CIS Eastern Arctic regional ice charts were obtained for every week between 2015-2024 [65]. Lancaster Sound ROI IC were decoded using the Egg Code. The main method of comparison was via graphs as detailed in Section 2.9.1.

The uncertainty on a CIS ice chart IC value was set as 10% of the IC value for this research, based on the literature [69, 70]. Fig 2.2 shows an example of an Eastern Arctic weekly regional ice chart. The egg shaped items that contain numbers are the egg code. The number at the very top of each egg is the IC for the related region. In this case, G, B, GG, Y and W are all present in Lancaster Sound. The ice chart is also colour coded by IC in tenths. The IC value was the information of interest for this research.

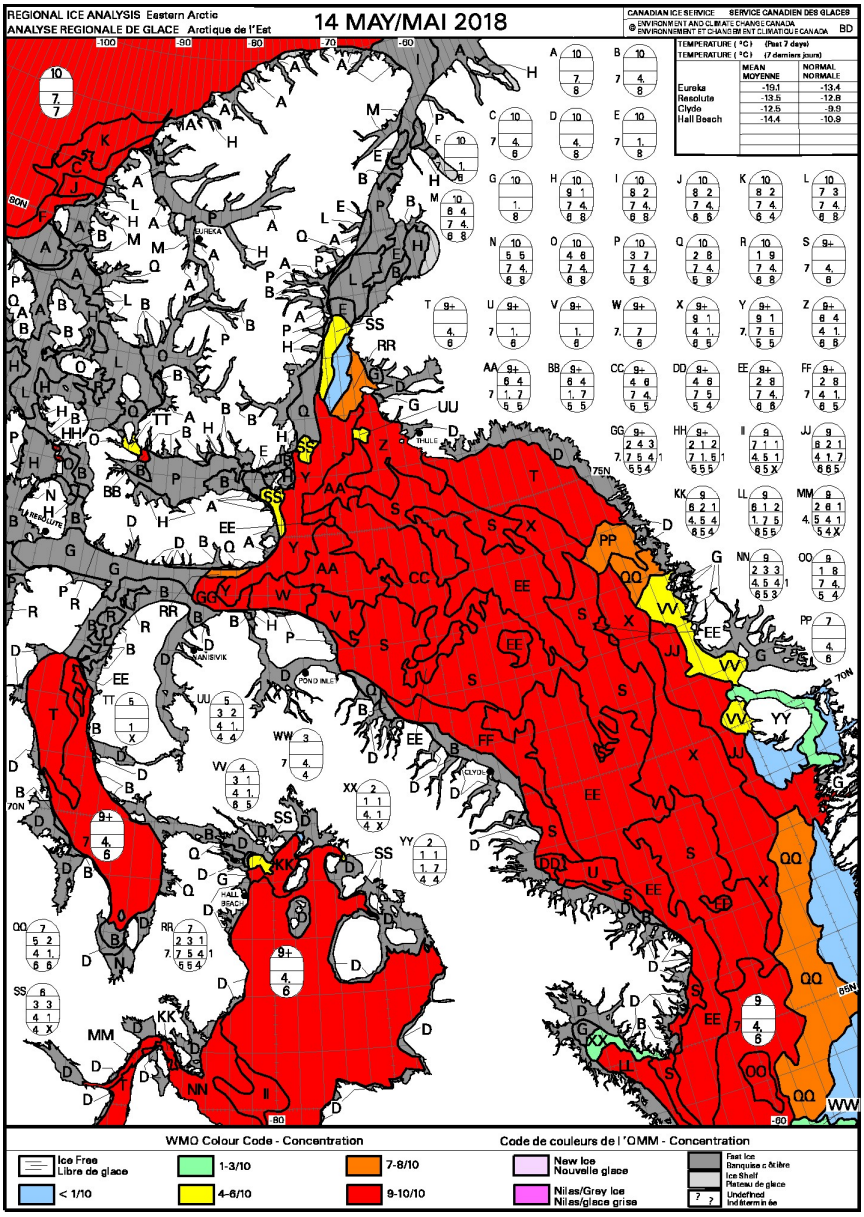

Figure 2.2: Canadian Ice Service Eastern Arctic weekly regional ice chart example [65]

2.8.2 University of Bremen IC Maps using Passive Microwaves

The Institute of Environmental Physics at the University of Bremen has created freely available IC maps derived from the AMSR-2 data, available at their website [71]. The AMSR-2 was launched in May 2012 aboard the Global Change Observation Mission Water "Shizuku" (GCOM-W1) satellite by the Japan Aerospace Exploration Agency (JAXA), and is the successor to the AMSR-E PM radiometer that was aboard NASA's Aqua satellite [72]. Part of Aqua's mission was SST, ice, and snow [32,73]. AMSR-2 has multi-frequency, total-power microwave radiometer systems with DP channels for all frequency bands, and continues AMSR-E observations including SST and sea IC [72]. The U Bremen-created AMSR-2 IC maps are based on the Arctic Radiation and Turbulence Interaction Study Sea Ice (ASI) algorithm work [74]. The ASI algorithm combined a model for retrieving the sea IC from SSM/I 85-GHz data proposed by [75] with an ocean mask derived from the 18-, 23-, and 37 GHz AMSR-E data using weather filters [74]. The ASI algorithm provided nearly three times the spatial resolution of SSM/I [74]. Among the geophysical implications of the ASI algorithm are: its higher spatial resolution allows better estimation of crucial variables in numerical atmospheric and ocean models, for example, the heat flux between ocean and atmosphere, especially near coastlines and in polynyas; and it provides an additional time series of ice area and extent for climate studies [74].

The AMSR-2 IC maps are 6.25 km spatial resolution, available in RGB visible colours, or false colours (termed *NIC*) which gives a colour spectrum based on range of IC [32,71]. Fig. 2.3 shows a daily IC image in false colours, with the Lancaster Sound region also zoomed in. The U Bremen website [71] also has 1 km resolution maps created from Moderate Resolution Imaging Spectroradiometer (MODIS)-AMSR-2 data starting in October 2019, and melt pond maps (12.5 km resolution) from Sentinel-3 data starting in 2024, though neither were used for this research because they did not cover the full 10-year research period.

U Bremen sea IC maps were obtained as follows: at the U Bremen website, within "Sea Ice Maps University of Bremen", selected "Data Archive" then "Data browser", chose the Northwest Passage, and obtained AMSR-2 IC maps for the days in the past. The Lancaster Sound region could be zoomed-in by a small amount.

The uncertainty on the AMSR-2 map IC values was set as 10% of the IC value for this research. The literature stated that for the AMSR-2 data, the ASI algorithm that the IC maps are based on is reported to produce IC

with errors less than 10% for middle and high IC (above 65% or 6.5 tenths) [69, 74]. The errors for low IC may have substantial variations depending on the atmospheric conditions [69, 74], which is mostly related to using weather filtering to reduce the effect of atmospheric contamination. Since it could not be determined what the uncertainty was for the AMSR-2 IC maps for IC less than 6.5 tenths, the simplified assumption of 10% of any IC values was used.

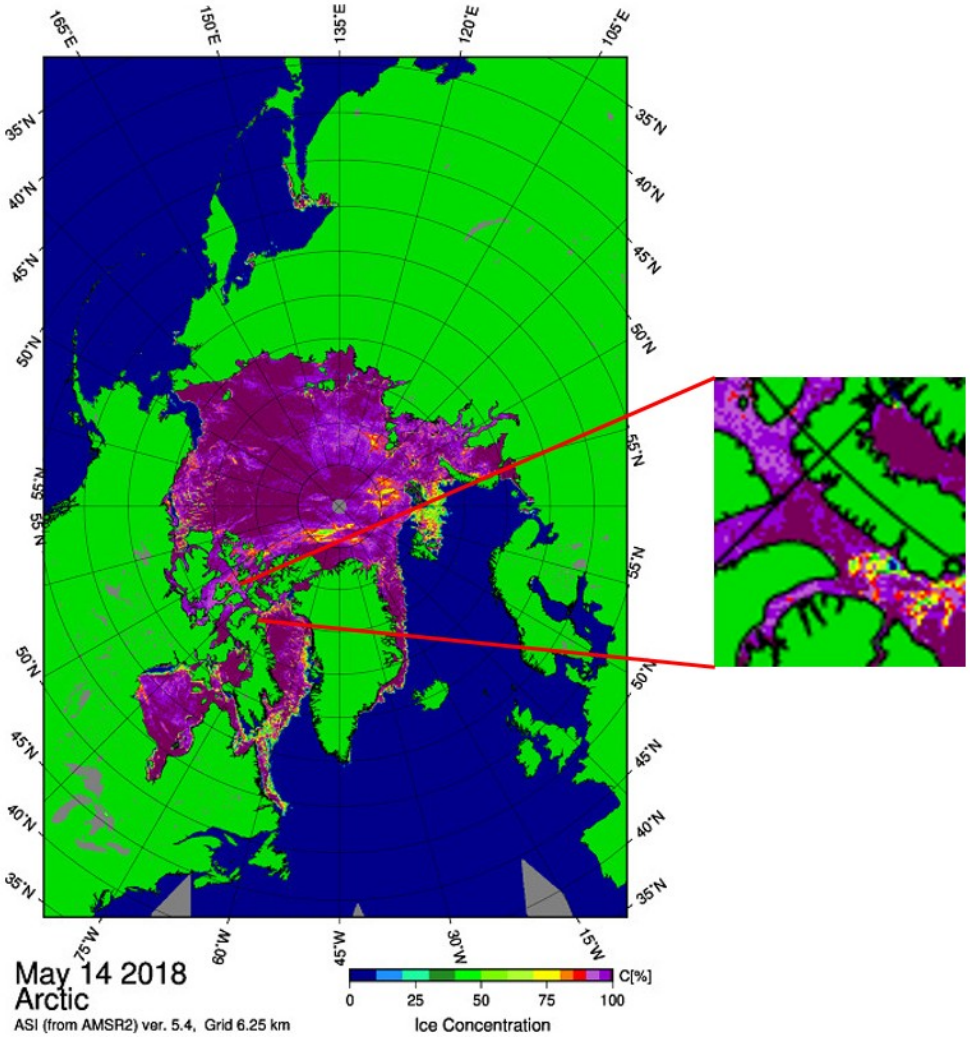

Figure 2.3: University of Bremen Arctic AMSR-2 passive microwave-based IC daily map example with Lancaster Sound area enlarged [71]

2.9 ACIC Applied to Lancaster Sound 2015-2024

2.9.1 Weekly ACIC Results (with Gap-filling) for 2015-2024

To determine a 10-year trend from 2015-2024, weekly cloud-free AVHRR images were analyzed using CASSTA and ACIC. The day chosen for each week was aligned with the CIS ice chart date, however, ± 2 days from the CIS ice chart date was allowed for AVHRR images to maximize the number of useable images. When AVHRR gaps occurred, SAR images were used (Sentinel-1 during 2015-2019, and RCM for 2020-2024), also with a ± 2 day allowance, with isodata unsupervised classification applied in ENVI for IC estimation. For times of the year where non-cloudy AVHRR images were available but it was too warm for the ACIC, visible channel visual inspection and/or isodata unsupervised classification was used. The results were amalgamated and graphed per year and compared to the CIS ice chart IC results. Calendar days for the graphs were aligned with the CIS ice chart dates for the specific year. IC values were taken at four locations within Lancaster Sound/Barrow Strait and then averaged: Resolute, Prince Leopold Island, directly north of Arctic Bay, and the eastern edge of Devon Island, which are shown by the red vertical lines in Fig. 2.4. Sometimes the IC varied along one of those vertical lines on a particular day, so an overall average value was chosen for that area. On some days, one of the particular locations was clouded, so no value was used that day for that location.

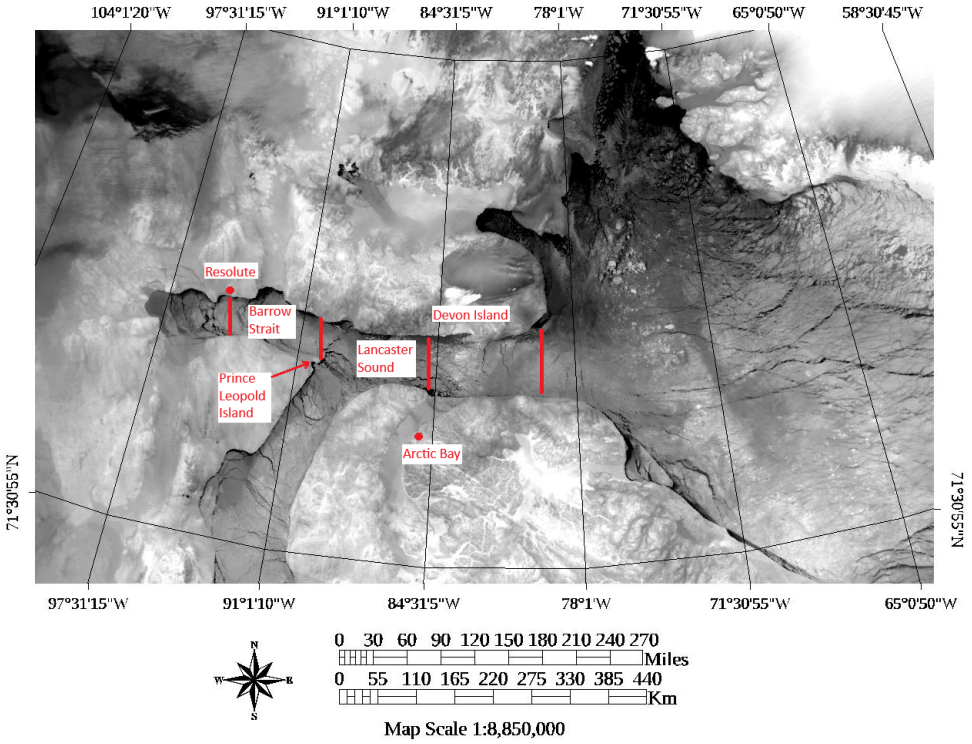

Figure 2.4: Lancaster Sound satellite TIR imagery map (Jan 14, 2019) with four locations identified identified for IC data recording. An average daily IC for Lancaster Sound was determined by averaging the IC at these four locations on that day.

The following graphs were created to visualize the results:

1. Yearly IC vs calendar day # for each of the 10 years (ACIC results, gap-filled with SAR and AVHRR visible channel, compared to CIS ice chart IC results);
2. 10-year average IC vs calendar day # for 2015-2024 (ACIC results, gap-filled with SAR and AVHRR visible channel, compared to CIS ice chart IC results);
3. Regional (Resolute, Prince Leopold Island, location north of Arctic Bay, and eastern edge of Devon Island) 10-year average IC vs calendar day # for 2015-2024 (ACIC results, gap-filled with SAR and AVHRR visible channel, compared to CIS ice chart IC results);
4. 10-year comparison of: ice arch formation, ice arch collapse, full OW start date, full OW end date, and date limiters for when the ACIC

starts and stops working in a calendar year; and
5. 10-year accuracy assessment graph comparing ACIC-only results (no SAR or AVHRR visible channel) with CIS ice chart IC results and U Bremen AMSR-2 IC results for times of the year when ACIC worked accurately.

2.9.2 Uncertainty Analysis

For a single-year graph, the uncertainty (u_{ACIC-1}) on an ACIC value in tenths was calculated as per Eqn. 2.8:

$$u_{ACIC-1} = u_{image} + u_{accuracy} \tag{2.8}$$

The value of u_{image}, the uncertainty of the IC values read from the ACIC images, was set to 0.5 tenths based on ability to read the colour accurately, as well as account for potential various ICs within a small area. The value of $u_{accuracy}$, the uncertainty in tenths for the ACIC depending on IC value and SST, was determined using the graph in the related Technical Note [76] in Appendix A. For each IC value, the CASSTA image was examined to determine whether the average SST was closer to -20° C or -30° C. In general, $u_{accuracy}$ was more precise at higher IC, meaning the uncertainty value was smaller.

For a single-year graph, the uncertainty on a SAR IC value (u_{SAR}) was set as an assumed conservative value of 1.0 tenths, due to the results obtained from the isodata unsupervised classification and the lower precision of those results. The same uncertainty of 1.0 tenths was also selected for AVHRR visible channel results, (u_{vis}) for similar reasons. This uncertainty applied to both AVHRR visible channel isodata and visual inspection results.

For a single-year graph, the uncertainty on a CIS ice chart IC value (u_{CIS-1}) was set as 10% of the IC value, based on the literature [69, 70]. This resulted in a maximum uncertainty of 1.0 for an IC value of 10 tenths, and reduced for lower IC values.

For the 10-year average IC graph, the uncertainty ($u_{ACIC-10}$) on an ACIC value in tenths was calculated as per Eqn. 2.9:

$$u_{ACIC-10} = \frac{\sigma_{ACIC}}{\sqrt{n}} + u_{image} + u_{accuracy} \tag{2.9}$$

The first term in Eqn. 2.9 is the uncertainty on a calculated average [77], where σ_{ACIC} is the standard deviation of all the values used to calculate an average, and n is the number of values. For example, if 10 numbers were used to calculate the average, n=10. The distribution of values was assumed to be a

normal (Gaussian) distribution for all of the calculations of uncertainties on a calculated average used for the various data sources (ACIC, CIS and AMSR-2) in this subsection. The value of u_{image} was still 0.5 tenths. For $u_{accuracy}$, the average SST for the 10-year period for each average IC value was calculated, so that the graph in the related Technical Note [76] in Appendix A could be applied. This graph in Appendix A provided error in IC tenths coverage based on SST and IC value obtained by the ACIC. For simplicity, even though some of the IC values used to generate the ACIC lines in the 10-year average graphs were based on SAR or AVHRR visual channel, $u_{accuracy}$ was applied in Eqn. 2.9 as if all the values in a calculated average were ACIC data, for simplicity.

For the 10-year average IC graph, the uncertainty on a CIS ice chart IC value was calculated as per Eqn. 2.10

$$u_{CIS-10} = \frac{\sigma_{CIS}}{\sqrt{n}} + u_{CIS-1} \tag{2.10}$$

The first term is applied similar to the ACIC average, and the (u_{CIS-1}) was still set as 10% of the IC value, based on the literature [69, 70].

For the 10-year ACIC accuracy assessment graph that contained ACIC-only (no SAR or AVHRR visible channel gap-filling), CIS ice chart IC and U Bremen AMSR-2 IC data, the uncertainty method for the ACIC and CIS data was calculated in the same manner as for the 10-year average IC graph. The only difference for the ACIC data was that SAR and visible channel data points were removed in calculation of the averages, which meant the value n in the first term of Eqn. 2.9 was reduced to the appropriate number for that week, for example n=8 if 8 ACIC values were used in calculation of the average ACIC value.

For the 10-year ACIC accuracy assessment graph for the U Bremen AMSR-2 data, the uncertainty ($u_{AMSR2-10}$) was calculated using Eqn. 2.11:

$$u_{AMSR2-10} = \frac{\sigma_{AMSR2}}{\sqrt{n}} + u_{image} + u_{AMSR2} \tag{2.11}$$

The first term is applied similar to the ACIC average. The value of u_{image} was also set as 0.5 tenths based on ability to read the colour accurately on the U Bremen AMSR-2 IC images, as well as account for potential various ICs within a small area. The value of u_{AMSR2} was set similar to the CIS uncertainty, which was 10% of the IC value. The literature stated that for the AMSR-2 data, the ASI algorithm that the IC maps are based on is reported to produce IC with errors less than 10% for middle and high IC (above 65% or 6.5 tenths) [69, 74]. The errors for low IC may have substantial variations

depending on the atmospheric conditions [69, 74], which is mostly related to using weather filtering to reduce the effect of atmospheric contamination. Since it could not be determined what the uncertainty was for the AMSR-2 IC maps for IC less than 6.5 tenths, the simplified 10% of any IC values was used.

2.9.3 Seven-Day Continuous ACIC Analysis

To determine how the ACIC performed over a several-day span, three of the seven+ multi-day streaks from Table 2.5 were chosen and analyzed: calendar days 32-37 (31 Jan - Feb 6) in 2017, 71-77 (Mar 12-18) in 2018, and 91-97 (Apr 1-7) in 2023. A seven-continuous day analysis allowed for study of the ACIC on a smaller scale than the weekly analysis. Choosing three different times of year allowed for observation of different ice dynamics. Comparison with U Bremen AMSR-2 images for those same seven-day periods, as well as the weekly CIS ice chart, was completed to observe similarities and differences.

2.9.4 Time of Year Limits for CASSTA and ACIC

To determine the limits on CASSTA and ACIC on the MetOp-A AVHRR images of Lancaster Sound in ENVI, data from 2016 was used at first, since it was one of the most non-cloudy years for all months of the year. The following were checked:

1. Determined if/when CASSTA's accuracy encountered problems based on amount of ice in Lancaster Sound or certain time of year. To determine accuracy, referred to geo-referenced AVHRR band 4 image. Mainly looked to see if ice/water/land differentiated properly;
2. Determined if/what different temperature scale than the M30_0 would be better for warmer months;
3. Determined if/when IC accuracy encountered problems based on amount of ice in Lancaster Sound or certain time of year. To determine accuracy, referred to geo-referenced AVHRR band 4 image, CIS ice chart, and U Bremen AMSR-2 IC map; and
4. Documented observed limitations, which were used to inform the applications of the algorithms to the other years (2015 and 2017-2024 inclusive).

Once any limits were determined for 2016, CASSTA and ACIC analysis was conducted for the other years in the 2015-2024 period. The information learned from the 2016 analysis allowed better prediction/identification of the ACIC limits for the other nine years. In general, SST became too warm,

which occurred when SST > -1.8° C, for the ACIC to work between roughly end May/early June to late September/October, depending on the year.

2.10 AVHRR Visible Channel/Band use for Gap-filling

2.10.1 Times of Year Used

During times of the year when non-cloudy AVHRR images were available, but it was too warm for the ACIC to work, which was determined to be when SST was warmer than -1.8° C, isodata unsupervised classification or visual inspection in the visible channel (channel 1) was conducted to estimate IC. This usually occurred in the June/July/August/September timeframe, though many weeks in late July/August/early September were also fully OW in Lancaster Sound, depending on the year.

2.10.2 Isodata Unsupervised Classification and Visual Processes

Isodata unsupervised classification process was applied to AVHRR visual channel images. Isodata calculates class means evenly distributed in the data space then iteratively clusters the remaining pixels using minimum distance techniques [78]. Each iteration recalculates the means and reclassifies pixels with respect to the new means. Iterative class splitting, merging, and deleting is done based on input threshold parameters, such as # of classes, # of iterations, and minimum # of pixels per class [78]. All pixels are classified to the nearest class unless a standard deviation or distance threshold is specified, in which case some pixels may be unclassified if they do not meet the selected criteria. This process continues until the number of pixels in each class changes by less than the selected pixel change threshold or the maximum number of iterations is reached [78]. Isodata was chosen over K-Means, the other unsupervised classification process in ENVI [79], because isodata allows for different number of pixel clusters while the K-Means assumes that the number of clusters is known apriori. Therefore using isodata provided some more flexibility in the analysis.

When isodata analysis was performed, a subsection of Lancaster Sound without land was chosen. Then an isodata unsupervised classification was performed in ENVI with 3 to 5 classes, 3 iterations, and 3 pixels min per class. In general, 4-5 colour classes resulted (red, green, blue, yellow, teal). Red corresponded to OW the majority of the time, and sometimes it made

sense to add the green or green+blue results to the OW percentage as well. The criteria for when to add green and/or green+blue to the OW percentage was based on cross-referencing with the water and ice features in the related AVHRR visual channel image, and sometimes also cross-referencing with the U Bremen AMSR-2 PM image from the same day. Using the statistics window, the overall IC percentage of the pixels in the selected section of the satellite image could be calculated. Analyst interpretation was required to determine if the results were acceptably accurate or not.

Application of isodata analysis in ENVI was as follows:

1. Opened MetOp AVHRR grey scale visible channel image, which was then geo-referenced using UTM Zone 17;
2. Selected Classification / Unsupervised / Isodata;
3. Selected the image, and chose spatial subset. From the spatial subset screen, selected Image, then modified the Samples and Lines values to change the size of the box that was used for the isodata analysis. In general, the box was maximized as much as possible within Lancaster Sound, without including any sections of land;
4. In the Isodata Parameters screen, number of classes used was min 3 to max 5, with 3 iterations, 3 min pixels per class, and a change threshold of 5 percent. Some trials of various settings were conducted before deciding on this set of criteria;
5. Linked the isodata display with the AVHRR image display;
6. Using Cursor Location/Value on the isodata image, it was determined which colour corresponds to which class; and
7. In general, 4-5 colour classes resulted (red, green, blue, yellow, teal). Red corresponded to OW the majority of the time, and sometimes it made sense to add the green or green+blue results to the OW percentage as well. The statistics window allowed for a calculation of overall IC within the selected section of the satellite image. Using Cursor Location/Value allowed determination of which colour corresponded to which class #. Class colours could then be changed, if required, by selecting Tools/Colour Mapping/Class Colour Mapping, though this was not used as the colours mapped in the same order for each image.

For cases where visual-only inspection of the AVHRR visible channel (channel 1) was used, there had to be sufficient sunlight and the mixture of OW and ice had to be easily differentiated. IC could then be estimated based on the visual guide in Fig. 1.8.

2.11 SAR Isodata Unsupervised Classification IC Analysis

2.11.1 Previous General SAR-based IC Research

SAR is advantageous because it can penetrate clouds, dry ice cover and snow [54]. In the literature, the majority of previous SAR IC work involved training data sets, algorithms and Neural Network (NN) methods such as Multilayer Perception (MLP), Convolutional NN (CNN) or Bayes Theorem [54]. Other options included thresholding, empirical model, and data assimilation [54]. For SAR on its own, pixels with homogeneous contents can be acquired using SAR sensors in fine resolution, whereby sea IC estimation can be transformed into pixel classification [54]. Then, sea IC can be derived by dividing the number of ice pixels by the total number of pixels excluding land in a region [54]. However, the SAR backscatter from the wind-roughened water surface can overlap with the backscatter from some ice types, which is a challenge for estimating sea IC using SAR data [54]. It was determined that the median of C-band is still significantly better than X-band and L-band, with the least sea ice classification inaccuracy, showing C-band SAR's robustness in sea ice classification [54]. In addition, C-band reliably provides the outline of the ice floes' edges, while L-band provides improved performance for the discrimination between thin ice and calm water [54]. For SAR scattering characteristics, C-band SAR data could not be used alone to classify FYI and MYI during the melt season, due to their physical and electromagnetic properties being similar when imaged using microwave scattering energy [54]. A classification method known as the Wackerman classification has been used in the past for SAR imagery, which is a type of supervised classification that can separate multiyear, undeformed FYI, and to some extent, deformed FYI and young ice in the leads [32].

To have a data-driven method for SAR ice-water classification, the most important procedure is to create a high-quality training data set, which requires accurate ice-water segmentation reference ("ground truth") and a large number of SAR images [52]. Ordinarily, the ground truth is derived from visual interpretation of SAR images and manually derived sea ice charts from operational ice service divisions, however, the disadvantage of this visual interpretation is that it is time consuming and tends to lead to inaccurate label results, especially for small objects such as leads and ice floes [52]. In addition, visual inspection also leads to mislabeling when sea ice and OW have very similar backscattering characterizations, which can occur under certain incidence angle and wind conditions [52].

A study of RADARSAT-2 fine quad-pol mode (HH, HV, VH, VV) images from October 2008 to September 2019, including the arctic region, resulted in the following observations regarding ice characteristics: wind-roughened OW and MYI-covered areas have very similar backscatter intensities; HV-pol SAR images exhibited higher ice-water contrast than the HH and VV-pol images, especially in the complicated MIZ; small ice floes and leads were more clearly visible in the HV-pol SAR image than HH and VV-pol; and the MIZ, sea ice and OW had comparable HV-pol radar backscattering [52].

Sea IC of the Baltic Sea near Finland was analyzed using RADARSAT-2 DP (HH/HV combination) ScanSAR wide mode data, though only the HH polarization was used for the study, and AMSR-2 PM Level 1B brightness temperature data [80]. Incidence angle corrections were applied to the SAR images, after they were calibrated and rectified to Transverse Mercator projection. The SAR image resolutions were 500 m, while the AMSR-2 resolution was 10 km. Computation of the IC then required a MLP NN [80]. One benefit of using SAR imagery for IC was that typically at the OW-ice boundary, there are mixed ice-water pixels, and the concentration estimates are blurred. The improved SAR resolution reduces the blurring at the edges and thus produces sharper boundaries [80]. The generated IC algorithm was compared to Finnish Meteorological Institute ice charts, an AMSR-2 algorithm from the literature, and an ASMR-2 algorithm from JAXA, with promising results [80].

2.11.2 Previous Sentinel-1 IC Research

Sentinel-1 was used to study sea ice in the Victoria Strait and M'Clintock Channel waterways in the Canadian Arctic in March/April 2017 using EW beam mode [81]. Over Arctic sea ice, EW scenes were acquired in DP (HH and HV) modes, however, only the HH polarization images were utilized for their study due to the lower signal-to-noise ratio of the HV channel, particularly over low-intensity targets such as smooth FYI [81].

Sentinel-1 SAR effects over open ocean were also studied [82]. One phenomenon often observed in Sentinel-1 SAR images acquired over the open ocean are areas of very high radar backscatter, often referred to as bright patches, which are observed when rain is present [82]. As a result, it was determined that such bright patches visible in Sentinel-1 SAR images are related to rain cells, rain bands and larger rain areas, with volume scattering being the dominant scattering mechanism [82].

A sea IC estimation in the Baltic Sea using Sentinel-1 SAR and AMSR-2 PM radiometer data was completed using approximately 102 Sentinel-1 EW mode HH/HV images from January 2016 [83]. It was concluded that SAR

alone can be used for sea IC estimation, but the results were more reliable and accurate for combined SAR and AMSR-2. In addition, the SAR IC results were more detailed than the ice charts, as it is impossible for ice chart analysts to delineate all of the small details within their limited time frames for the ice charts [83].

2.11.3 Previous RCM IC Research

Arctic sea ice topography was studied using RCM SAR backscatter, specifically focusing on the McClintock Channel in the Canadian Arctic [84], located southwest of Lancaster Sound, as shown in Fig. 1.4. The ROI included a range of ice conditions, including a mixture of smooth and deformed FYI, as well as MYI [84]. The area was studied from summer 2021 to winter 2022. Images were obtained in the Low Noise (SCLN) mode, because of the lack of scalloping in the azimuth direction in the HV channel compared to ScanSAR mode, and its low noise floor compared to other modes and instruments [84]. RCM's SCLN noise floor was determined to be -34 dB (though nominally advertised as -28 dB), while the nominal ScanSAR mode noise floor is -26 dB (for comparison, it is -22 dB for Sentinel-1's EW and IW swath modes) [84]. Both HH and HV bands for each image were radiometrically calibrated, speckle-filtered using a Lee 7x7 filter and map-projected, and converted to dB for analysis [84]. The late-winter period was focused on because the effect of meltwater on SAR backscatter after melt onset was expected to alter the relationship between sea ice topography and backscatter [84]. Images were collected at an incidence angle range of 25° to 55° on multiple days on different paths [84]. It was found that backscatter from the HV band had a stronger correlation with FYI surface roughness than HH. The relationship was also strongest at near-range incidence angles, though all incidence angles may be used [84].

Simulated RCM CP SAR imagery was compared to actual RADARSAT-2 SAR images for classification between FYI and MYI in two locations in the CAA, Victoria Strait and the M'Clintock Channel [85]. These two locations are shown in Fig. 1.4. The differences in classification results between RCM and RADARSAT-2 were minor, and FYI classification accuracies were >96% in both regions [85].

RCM first year in-orbit performance was compared with RADARSAT-2 images for sea ice analysis [60]. For operational sea ice monitoring, CP SAR imagery is beneficial, given its similar spatial coverage to linear polarization, yet with increased radar target information [60]. However, HH linearly polarized RCM images were used for the research for this thesis due to image availability, better characteristics than HV polarization, and using the same

HH polarization as the Sentinel-1 SAR images. The peak IC period in the region was identified as March, where the ice cover usually shows stable conditions that do not affect the backscatter from radar sensors [60]. A statistics analysis of the RADARSAT-2 and RCM images had the following results for HH and HV polarizations: thin and deformed ice exhibited the highest contrast between HH and HV; thin and rough ice provided the lowest contrast between HH and HV [60]. Overall, more detail was visible in the HH polarized images versus the HV polarized images [60].

An approach for deriving IC from RADARSAT-2 (ScanSAR Wide DP HH-HV) was adjusted for RCM data (ScanSAR beam modes with same HH-HV polarization option) over a one-year period (August 2020 to July 2021) [61]. The impact of assimilating RCM ICs on resulting ice analyses was evaluated against various ice data sources. It was stated that the only data source for IC analysis at a much finer spatial resolution than 5 km are the ice charts produced by the CIS [61]. However, the human process for creating ice charts is a lengthy and tedious task [61]. It was also mentioned that orbit degradation of the NOAA-19 satellite that carries an AVHRR sensor occurred, and as a result AVHRR data has not been assimilated operationally in the ice analysis system since April 2019 [61]. However, the MetOp series satellites are separate from NOAA-19, and AVHRR aboard MetOp-B and -C are still operational. MetOp-A ceased operations in December 2021. Large training datasets were built over a five-year period, matching SAR data with CIS ice chart data for 0% and 100% ICs [61]. Intermediate concentrations were intentionally avoided during the training process [61]. A method was also developed for quality control to suppress erroneous ice and water [61]. Comparison against the MODIS optical-based product for non-cloudy days at 4 km resolution, along with visual comparison with NASA Worldview application tool colour images were performed [61]. It was concluded that there was agreement between the RCM and CIS image analysis ICs [61]. For the visual assessment against cloud-free optical data, it was determined that RCM data was very important in resolving high resolution ice features, for example in the MIZ, and that RCM data is of great importance for efficient guidance of Arctic marine traffic [61].

2.11.4 Isodata Unsupervised Classification Process Used

Isodata unsupervised classification was used in ENVI on a subset of a SAR image using as much of Lancaster Sound as possible without including land. It appears that this process has not been used in the literature, and allowed for a quick, straightforward method of evaluating IC for a region within a SAR image. In general, this process only worked well if there was a substantial

amount of both ice and OW in the image. If there was too much ice or too much water, the analysis did not work properly due to high levels of noise in the image, which then made it difficult to properly identify/classify water and ice. If isodata analysis did not work on a particular day, sometimes visual inspection of the SAR image was sufficient to estimate IC. It was found that for both SAR satellites, Sentinel-1 and RCM, adaptive image filtering in ENVI (Lee, Frost, Gamma) did not measurably aid in producing better IC results using the isodata method. Step-by-step instructions were provided earlier in Section 2.10, as the process and analysis settings for the SAR isodata unsupervised classification was the same as that used for the AVHRR visible channel satellite images, except for the chosen starting image was either the Sentinel-1 HH-polarized or RCM HH-polarized image.

2.12 ACIC Accuracy Assessment

2.12.1 General

For evaluation of IC accuracy in general, a set of validation data should be used, with typical sources being shipboard observations, field measurements, airborne camera survey, operational ice charts and, to a lesser extent, ice motion maps [22]. Field measurements are the closest dataset to truth data, however, they are unavailable in the polar region during polar night and they are limited in spatial coverage. Operational ice charts are usually used as validation data though they cannot be considered truth data because the information is generated subjectively, and the charts are deliberately made conservatively, i.e: tend to exaggerate thicker and older ice percentage [22]. In addition, both temporal and spatial resolution of the ice charts are much coarser than the footprint of the radiometer or scatterometer system from which the ice chart is generated [22]. Therefore, it was recommended that the best method to assess the accuracy of a sea IC algorithm is to compare results to IC data from as many sources as possible and also conduct intercomparison between results from different algorithms [22]. This is not considered a strictly validation approach, but, in the absence of truth data, would facilitate validation in at least a gross sense [22]. Therefore, using the term "accuracy assessment" versus "validation" for this comparison method was recommended [22].

2.12.2 Ten-year ACIC Accuracy Assessment Graph

To determine how accurately the ACIC measured IC over the 2015-2024 10-year period in Lancaster Sound, a graph was created to compare the ACIC results with the CIS ice charts IC and the U Bremen AMSR-2 PM IC results. The numbers sourced from the CIS ice charts and U Bremen AMSR-2 IC maps were interpreted by the author of this thesis from analyzing those charts/maps. For the ACIC results for this graph, any SAR and AVHRR visible channel gap-filling data was removed, which sometimes required re-averaging of certain data points. In addition, the comparison was only done for the periods of the year when the ACIC was determined to be working accuratly. Uncertainties for the ACIC, CIS ice charts IC and U Bremen AMSR-2 IC data were calculated as per Eqn. 2.9, Eqn. 2.10 and Eqn. 2.11 respectively, detailed in Section 2.9.2.

2.12.3 ACIC and SAR Near-Concurrent Images Comparison

Sentinel-1 and RCM SAR imagery obtained near-concurrent in day/time with analyzed AVHRR imagery was used to evaluate the accuracy of the ACIC. Isodata unsupervised classification and visual observation of the SAR image were used as comparison tools. It was determined to be difficult to find many examples of near-concurrent non-cloudy AVHRR and SAR imagery due to numbers of non-cloudy AVHRR images and how much of Lancaster Sound was captured in a SAR image at a near-concurrent time period.

2.13 Sea Ice Melting/Freezing in Lancaster Sound

2.13.1 Previous Research on Lancaster Sound Polynyas

The formation and collapse of the Lancaster Sound ice arch and polynya from 1979-2022 was analyzed [24]. From 1979-2000, the linear trend [24] indicated that the ice arch formed more than two months later, with a weak statistical trend of a modest decrease in the ice arch collapse over that span [24]. From 2001 to 2022, no trend was found in either the timing of the ice arch formation or collapse [24]. Nonetheless, an ice arch and polynya has formed every year in Lancaster Sound from 1979-2022, and in general, the ice arch forms in mid-February and collapses in late June [24].

The three major findings from [24] were as follows:

1. Ice arch location had a high interannual variability (over the 1979-2022 span) with 512 km between the eastern and western extremes. The ice

arch generally formed at various locations within Lancaster Sound, Barrow Strait, and even in the vicinity of eastern Somerset Island. The overall trend was a statistically weak trend of a westward movement of the ice arch by 115 km;
2. The data indicated that the ice arch location had no bearing on either the formation or collapse of the structure; and
3. Although highly variable, a linear trend from 1979 to 2022 showed a reduction of 48 days in ice arch duration.

For the time period of 2015-2024 examined by the research for this thesis, the formation and collapse of the ice arch was also highly variable for 2015-2022 [24], with the formation date ranging from calendar day 1 (Jan 1) in 2015 to day 105 (Apr 15) in 2018, and the collapse date ranging from calendar day 160 (Jun 9) in 2017 to day 195 (Jul 14) in 2021 [24]. In-year, 2015 had the longest ice arch duration of 179 days, and 2018 had the shortest duration of 67 days [24]. Table 2.9 summarizes these ice arch start and end dates from [24]. Ice arch formation and collapse dates for 2023 and 2024 were determined during this research from visual analysis of the TIR and visible channels of the Lancaster Sound AVHRR images.

Table 2.9: Ice arch formation and collapse in Lancaster Sound, 2015-2022 (values approximated from [24])

Year	Formation Month & Day (±3 Days)	Formation Calendar Day # (±3 Days)	Collapse Month & Day (±3 Days)	Collapse Calendar Day # (±3 Days)	Ice Arch Duration (±6 Days)
2015	Jan 1	1	Jun 29	180	179
2016	Feb 29	60	Jul 3	185	125
2017	Mar 11	70	Jun 9	160	90
2018	Apr 15	105	Jun 21	172	67
2019	Feb 4	35	Jun 19	170	135
2020	Mar 2	62	Jun 23	175	113
2021	Mar 1	60	Jul 14	195	135
2022	Feb 19	50	Jun 29	180	130

2.13.2 Previous Melt/Freeze Research in the CAA and NWP

The CAA is a collection of small islands located west and northwest of Lancaster Sound, seen in Fig. 1.2 and 1.4, and a section is considered part of the NWP. Ice melt was studied in the CAA between 1997-2014, and an algorithm

for Arctic sea ice melt onset was developed using RADARSAT ScanSAR HH polarization SAR images (RADARSAT-1 from 1997-2007, and RADARSAT-2 from 2008-2014) [86]. Overall, no significant melt onset date trend was found over the 18 year period [86]. During melt onset, the presence of liquid water within the snow cover affects the dielectric properties of the snow and sea ice [86]. It was determined that for efficient melt onset detection and to avoid changes in dielectric and backscatter, only descending passes (colder local morning times) were used in their study [86]. Results, such as locations of MYI and FYI in images, were cross-referenced with CIS weekly ice charts [86]. SAR images were corrected for incidence angle variation, as ScanSAR mode incidence angles vary from 26° to 29° which results in a variation of up to 7 dB in backscatter intensity across an image [86]. Overall, the mean melt onset date in the northern CAA from 1997-2014 was calendar day 164 ± 4 days (Jun 13) [86]. This information is useful for narrowing the possible melt onset date window for Lancaster Sound.

Late winter snow cover on FYI in the CAA was analyzed using the C-band advanced scatterometer (ASCAT) microwave scatterometer aboard MetOp-A and MetOp-B, and MODIS optical imagery [87]. The seasonal evolution of snow covered Arctic FYI was described/summarized according to five categories: *freeze-up*, *winter*, *early melt*, *melt onset*, and *advanced melt* [87]. The initial freezing of Arctic seawater marks the beginning of freeze-up, which generally occurs in October and November due to decreasing solar radiation and surface air temperature [87]. As these decreases occur, thin sea ice grows thicker and a layer of snow begins to accumulate on the surface. Winter conditions generally occur from December to April, where FYI typically accumulates an increasingly thicker snow cover. In late April or early May, the early melt stage begins as snow temperatures increase with increasing solar input, and the diurnal temperature range in the snow increases [87]. Melt onset occurs in May or June when liquid water begins to accumulate near the top of the snow cover and among the meeting points of the snow grains within the snow volume [87]. Once warming above 0°C occurs, the water drains to the base of the snow cover. Advanced melt stage occurs when the snow continues to melt such that ponds begin to appear (*pond onset*) on the FYI surface, resulting in a dynamic mosaic of melt ponds, bare ice and snow patches [87]. As summer progresses, the ponds drain through the FYI until the sea ice breaks up and OW results.

Ice area extent in the CAA and northern route of the NWP from 1991-2024 was reported [16]. IC data was sourced from the CIS regional ice charts, and AVHRR 25 km resolution albedo data from the NOAA website. It was determined that 2024 was the most ice-free year for the northern route of the

NWP that was studied [16]. Table 2.10 shows the calendar day of melt onset in the northern route of the NWP from 2015-2024 [16].

Table 2.10: Timing of melt onset in the northern route of the Northwest Passage, 2015-2024 (adapted from [16])

Year	Melt Calendar Day	Date
2015	155	Jun 4
2016	157	Jun 5
2017	142	May 22
2018	155	Jun 4
2019	147	May 27
2020	154	Jun 2
2021	153	Jun 2
2022	165	Jun 14
2023	147	May 27
2024	153	Jun 1
Avg	153	Jun 2*

*Based on a non-leap year.

2.14 Audimus Mission-related Hydrophones/Sonobuoys Deployment

Lancaster Sound, over the time period 2015-2024 has been relatively ice free between mid-July to mid-September according to Section 1.4. Therefore, hydrophones could be deployed or sonobuoys could be dropped almost anytime in the water within that period. The more difficult predictions are the melting and freezing periods. By using the ACIC results, as well as SAR image and AVHRR visible channel image IC results, times of year to use hydrophones and/or sonobuoys in the water in melt/freeze seasons were determined. Since accuracy of dropping sonobuoys in water with high IC is risky for the sonobuoy and difficult for aircraft to track targets after initial detection, the AVHRR and SAR imagery were analyzed to determine when the majority of the Lancaster Sound IC reduced to 4/10, the lower limit of the open drift range as per Fig 1.8 in the melt season, and built up to 6/10, the upper limit of the open drift range in the freezing season. As a result, recommendations based on the 2015-2024 research period could be made for when hydrophones and sonobuoys could start to be used in the waters of Lancaster Sound during melt season, and when their use would need to be stopped in the freeze season.

2.15 Specific Research Objectives

The following specific research objectives for the Lancaster Sound ROI, from 2015-2024 inclusive, guided how the results were obtained and analyzed:

1. Create a 10-year data set of sea IC in Lancaster Sound from 2015-2024 using ACIC, gap-filled by SAR and AVHRR visible channel data;
2. Determine the applicability and accuracy of using MetOp-B and -C AVHRR satellite images for ACIC, since MetOp-A ceased operations in December 2021;
3. Evaluate the effectiveness and accuracy of ACIC, including time of year limits;
4. Use SAR imagery (Sentinel-1 for 2015-2019 and RCM for 2020-2024) and AVHRR visible channel imagery to gap-fill for cloudy AVHRR images, and determine IC using a manual unsupervised isodata classification method;
5. Provide melt and freeze date determination for 2015-2024 using ACIC results and a threshold of 4/10 IC for melt and 6/10 IC for freeze (lower and upper limits of the open drift range). Also determine ice arch formation and collapse dates for 2023 and 2024; and
6. Provide time of year recommendations, based on the ACIC results and melt/freeze dates, to locate hydrophones and/or sonobuoys in the waters of Lancaster Sound to support the Audimus cubesat mission.

3 Results

All results images, including those in Appendix B, were generated using ENVI remote sensing software version 5.7, using the *classic* interface display environment, unless otherwise stated.

3.1 MetOp-A/B/C use, ACIC Time of Year Limits, and Daylight

3.1.1 MetOp-A/B/C CASSTA Images Comparison

Three days in 2020 were tested for MetOp-A, -B and -C (Feb 13, Mar 6, and Jun 16) near-concurrent images. CASSTA and ice fog images were generated for each MetOp for each day, and the ENVI Change Detection tool was used to compare percent difference between MetOp-A and -B, -A and -C, and -B and -C CASSTA images. The percent difference was based on a non-zero pixel difference pixel count between the images.

Fig. 3.1 shows Feb 13, 2020 CASSTA images for MetOp-A, -B and -C, as well as the change detection for MetOp A/B, MetOp A/C and MetOp B/C. No land mask was applied. Fig. 3.1 a), b) and c) CASSTA images appear near identical, especially within Lancaster Sound. Fig. 3.1 d), e) and f) show the change detection percent results, where blue is a negative difference between final and initial images, and red is a positive difference. The values of the red and blue areas are approximately 1.4% for Fig. 3.1 d), 1.0% for e), and 2.4% for blue and 1.3% for red for f). The main difference is represented in the area east of Lancaster Sound, which coincided with some detected ice fog. For the main analysis in this research, every AVHRR image was checked for minimal or no ice fog before being used for CASSTA and IC analysis.

Fig. 3.2 shows Mar 6, 2020 CASSTA images for MetOp-A, -B and -C, as well as the change detection for MetOp A/B, MetOp A/C and MetOp B/C. No land mask was applied. There was no appreciable ice fog at that time and day. The CASSTA results between MetOp-A, -B and -C, as shown in Fig. 3.2 are

in agreement due to minimal red and blue on the grey images. In Fig. 3.2 d), e) and f), the values of the red and blue areas are approximately 0.9%, 0.6% and 0.5%, respectively, of the image. These near identical results include the factors that the solar zenith angle was not corrected for, and Lancaster Sound was near the edge of the image swath for the MetOp-A and -C images.

The maximum sensor zenith angle for these images at the edge of the AVHRR swath was approximately 52°, which provided a test of a non-ideal case. Therefore, images where Lancaster Sound was closer to nadir for the satellite would provide even better results. Therefore, due to the minimal percent differences determined during the change detection process for MetOp-A, -B, and -C, MetOp-B and -C satellite images were acceptable for use.

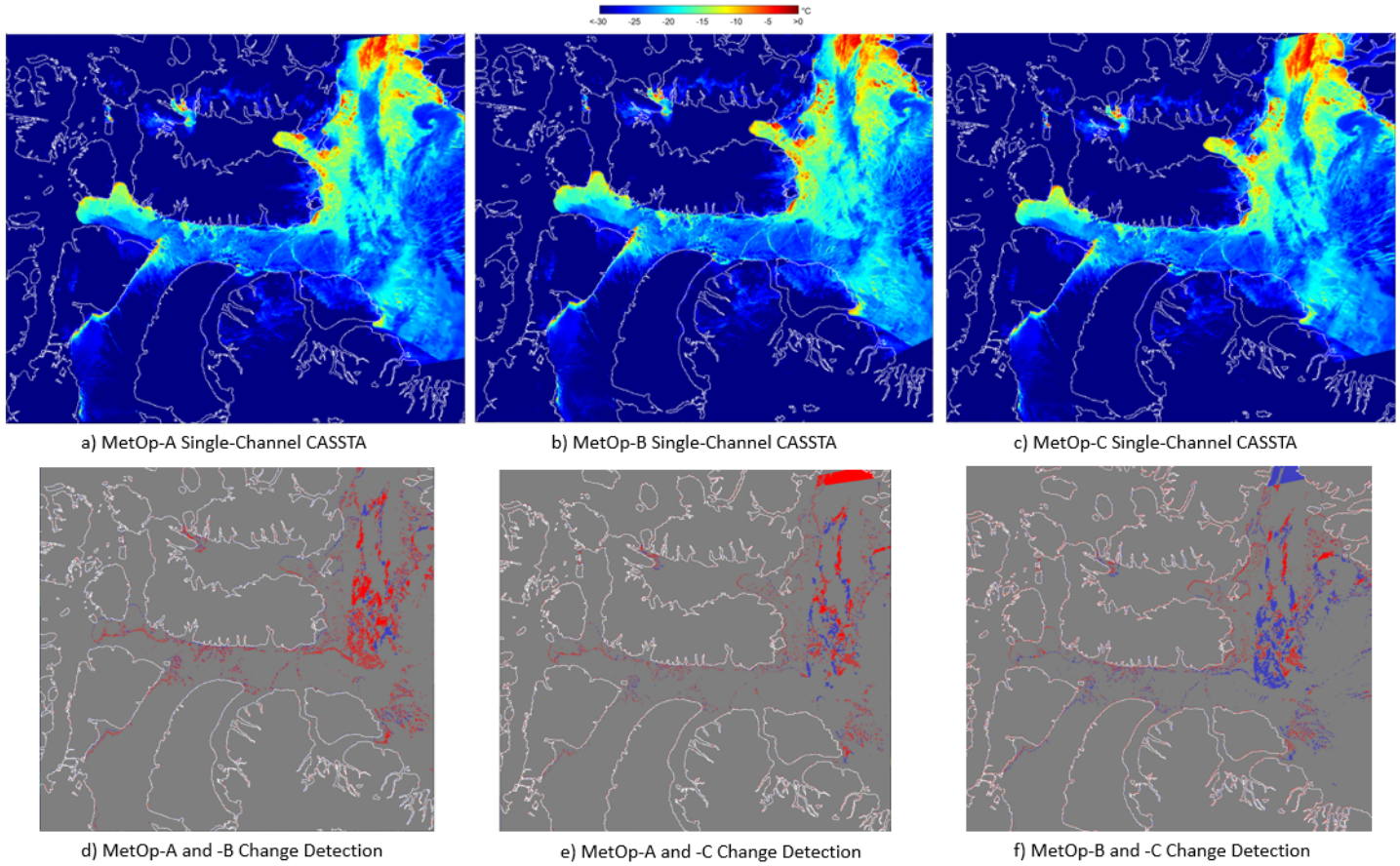

Figure 3.1: Feb 13, 2020 CASSTA and IC change detection for MetOp-A, -B and -C: a), b) and c) are near-concurrent CASSTA images, while d), e) and f) are the percent change detection results between two CASSTA images, where red indicates positive difference between final and initial images, and blue indicates negative difference between final and initial images. All differences were 2.4% or less. The temperature scale corresponds to the CASSTA images. No land mask applied.

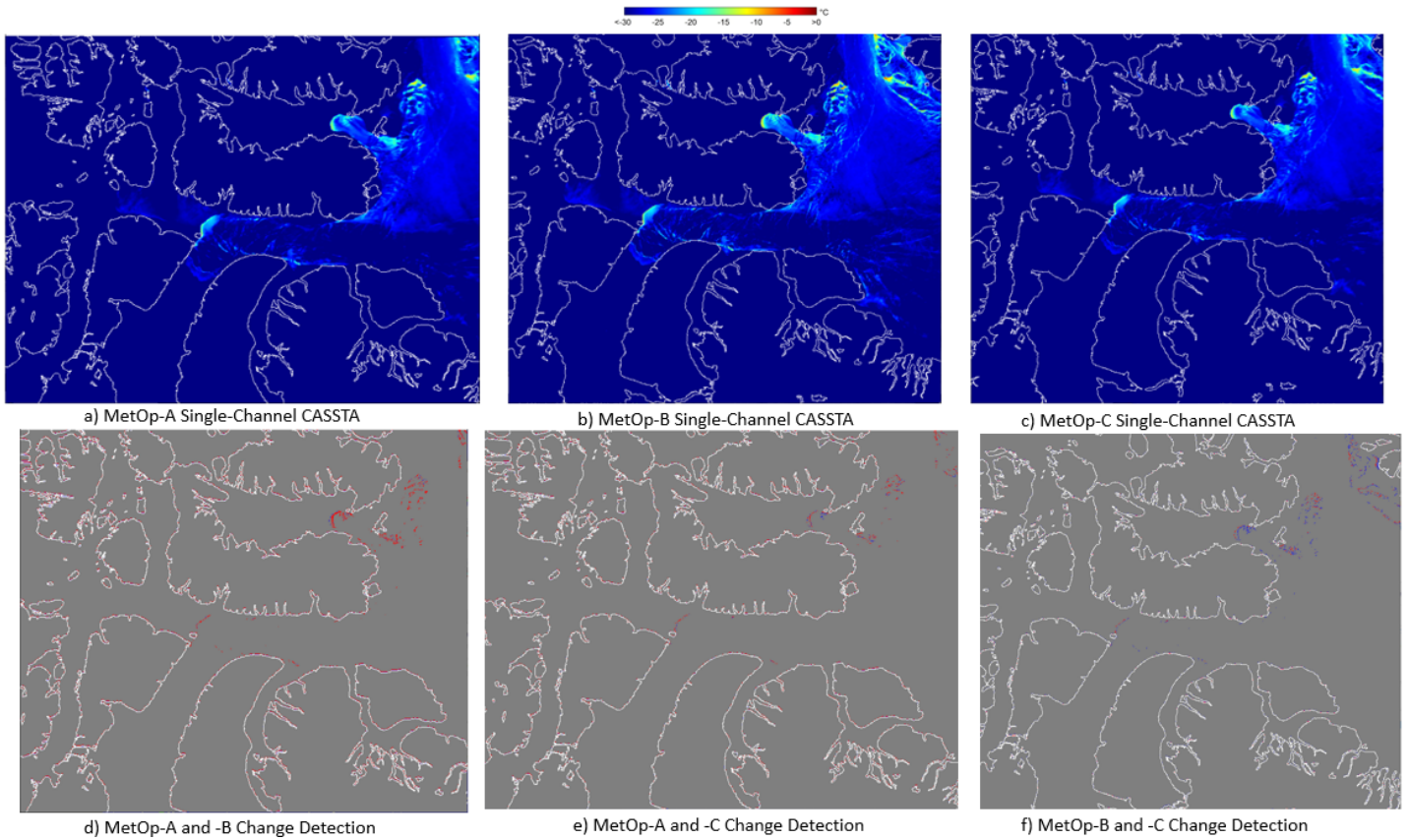

Figure 3.2: Mar 6, 2020 CASSTA and IC change detection for MetOp-A, -B and -C: a), b) and c) are near-concurrent CASSTA images, while d), e) and f) are the percent change detection results between two CASSTA images, where red indicates positive difference between final and initial images, and blue indicates negative difference between final and initial images. All differences were 0.9% or less. The temperature scale corresponds to the CASSTA images. No land mask applied

3.1.2 ACIC Initial Time of Year Limits Test

Data from 2016 was used to determine initial time of year working limits for ACIC, which provided guidance when the other nine years were analyzed. Three dates in 2016 were checked in this initial test, Oct 29, Nov 23 and Dec 18. The *M30_0* temperature colour spectrum (-30° C to 0° C) for CASSTA images did not work as well for June-September inclusive as it did not provide enough differentiation for warmer temperatures, so sometimes *M20_0* (-20° C to 0° C) was used. In 2016, it was determined that the ACIC worked up to approximately the end of May (May 24 analyzed), and then started working at the end of September again (Sep 27 analyzed). The determining factor was that the ice pack value for the spatial pixel editor, the $b9$ value from Eqn. 2.7, had to be $<$ -3° C for ACIC to be working accurately, which corresponded with the SST needing to be $<$ -1.8° C. It was straightforward to detect when ACIC no longer worked, as the ACIC image did not look accurate to the author of this thesis, based on observed discrepancies in ice and water identification when cross-referencing with the geo-referenced TIR image. Therefore, ACIC was expected to work approximately January-May inclusive and October-December inclusive (up to 8 months of the year), which was beneficial knowledge when analyzing the other nine years. The ice arch collapsed on Jul 3 in 2016, so ACIC did not work up to the arch collapse date.

3.1.3 Daylight During the Year in Lancaster Sound

The Lancaster Sound AVHRR images were obtained either between 0:00-03:00 GMT daily (18:00-21:00 local or 19:00-22:00 local the previous day, depending on west or east end of the Sound), or 22:00-24:00 GMT (16:00-18:00 local or 17:00-19:00 local depending on west or east end of the Sound). Resolute, at the west end, is GMT -6 hrs, while Pond Inlet at the east end is GMT -5 hrs. The majority of these images had Lancaster Sound at or near nadir in the image swath. Using a National Research Council sunrise/sunset calculator website [88], sunrise/sunset was calculated for Resolute, Nunavut for 2016. Sunset started later than 16:00 local as of Feb 22, though when the 10-years of AVHRR images were checked on a weekly basis, the visible channel only started showing some ambient light in early to mid-April. Sunset in Resolute on Apr 1, 2016 was at 20:00 local [88]. By Apr 25, Resolute was in full sun all day. In the fall of 2016, sunset reached 16:00 local by Oct 14. However, by observing the AVHRR images, the visible channel no longer showed any ambient light by end of September. Therefore, at least some daylight was present in the selected images between early/mid-April to end of September.

3.2 ACIC Results (SAR and AVHRR Visible Gap-filled) 2015-2024

3.2.1 ACIC (Gap-filled) Yearly Results vs CIS Ice Charts

Graphs of yearly average IC from 2015-2024 were created using weekly intervals. Each data point was an average of the IC at the four selected locations within Lancaster Sound on that particular day: Resolute, Prince Leopold Island, directly north of Arctic Bay, and the eastern edge of Devon Island, which are shown by the red vertical lines in Fig. 2.4. The data was based mostly on ACIC results, with SAR and AVHRR visible channel gap-filling as required. The corresponding weekly ACIC images showing the IC colour mapping are presented by year for the 2015-2024 period in Appendix B. The data points on Figures 3.3 to 3.12 are aligned with the CIS ice chart dates, so the corresponding images in Appendix B may be ± 2 days from those dates. Figures 3.3 to 3.12 show a comparison by year versus the CIS ice chart results. Any SAR gap-filling data points are marked with green dots on the graphs, and any AVHRR visible channel gap-filling data points are marked with purple dots. The error bars for ACIC data points were calculated using Eqn. 2.8. Error bars for SAR and AVHRR visible channel data points were set at ± 1.0 tenth based on the uncertainty method as detailed in Section 2.9.2. CIS ice chart error bars were set as ± 10% of the IC value, as per the related uncertainty method in Section 2.9.2. On the graphs, where the CIS ice chart value was shown as 9.5, that was an interpretation of the 9+ values given by the CIS ice charts, which were assigned a value of 9.5 for the research for this thesis. For the ACIC results during the coldest parts of the year, either a 9 or 10 for IC was assigned, as it was too difficult to accurately assign a 9.5 vice a 9 or 10 based on the colour spectrum. The uncertainty on a calculated average method was not used for the yearly graphs. This was due to each data point being an average of four values, corresponding to the four selected locations within Lancaster Sound, and, if there was a high variability in IC across the Sound on a particular day, including the presence of the ice arch and polynya, it would skew such uncertainties toward high values. As previously mentioned in the initial 2016 time of year limits test in Section 3.1.2, and confirmed during analysis of the other nine years, the ACIC was accurate between January-end May and October-December. For reference when reading the graphs, May 31 is calendar day 151 (152 on leap years such as 2016, 2020, 2024) and Oct 1 is calendar day 274 (275 on leap years). Table 3.1 maps calendar day numbers to dates for the first of each month. A full table for normal years and leap years are included in Appendix C. When average calendar dates are calculated

and reported in this thesis, the day and month assigned to it is based on a non-leap year.

Table 3.1: Calendar day number and date mapping

Date	Calendar Day # (Normal Year)	Calendar Day # (Leap Year*)
Jan 1	1	1
Feb 1	32	32
Mar 1	60	61
Apr 1	91	92
May 1	121	122
Jun 1	152	153
Jul 1	182	183
Aug 1	213	214
Sep 1	244	245
Oct 1	274	275
Nov 1	305	306
Dec 1	335	336

*2016, 2020 & 2024 are leap years within the 2015-2024 period.

The following are comments by year between the ACIC (gap-filled by SAR and AVHRR visible channel) and CIS ice chart IC results:

1. 2015 (Fig. 3.3) - There was significant ACIC variability from day 5-75 (Jan 5 - Mar 16), though the error bars overlapped with the CIS data. However, there was a noticeable difference, where error bars did not overlap, from day 82-138 (Mar 23 - May 18). Another significant difference was between days 280-292 (Oct 7-19). The ACIC results also showed more variability from mid-October to end-December (day 288 onwards). Furthermore, the visible channel results on days 180 and 187 (Jun 29 and Jul 6) showed OW while the CIS ice chart reported an IC of almost 1.3/10.
2. 2016 (Fig. 3.4) - There was significant ACIC variability from day 4-166 (Jan 4 - Jun 14), with only nine data points in that range overlapping with the CIS ice chart data, including error bars. This included significant lower ACIC from day 1-25 (Jan 1-25). There was less variability in the mid-October to end-December timeframe. Furthermore, the SAR result on day 256 (Sep 12) showed OW while the CIS ice chart results reported an IC of 2.5/10.
3. 2017 (Fig. 3.5) - There was some variability in ACIC from day 2-65 (Jan 2 - Mar 6), though the error bars generally overlapped with the CIS

data. The ACIC values then dipped lower between days 72-135 (Mar 13 - May 15). A specific observation for this year is the increase in IC during a portion of the summer, shown both by ACIC and CIS ice chart results. In the fall, the ACIC values were lower for days 290-345 (Oct 17 - Dec 11), though the error bars did overlap with the CIS ice chart data.

4. 2018 (Fig. 3.6) - There was a significant period of lower ACIC values from day 50-99 (Feb 19 - Apr 9). In the fall, the ACIC was lower from day 240-310 (Aug 28 - Nov 6). This year showed the highest IC values over the summer period, as reported by both ACIC and CIS ice chart data. However, the CIS ice chart data had a higher IC peak on days 218 and 225 (Aug 6 and Aug 13), while the corresponding SAR data points had lower IC values.
5. 2019 (Fig. 3.7) - In general, 2019 was one of the best matches of ACIC values with CIS ice chart values, error bars included. There was one anomalous low ACIC data point on day 133 (May 13).
6. 2020 (Fig. 3.8) - The year 2020 required significant gap-filling with SAR and AVHRR visible channel. There was a period where the ACIC values were much lower than the CIS ice chart data, between days 97-138 (Apr 6 - May 17). A second low period occurred in the early fall between days 250-300 (Sep 6 - Oct 26).
7. 2021 (Fig. 3.9) - The year 2021 was also one of the best matches of ACIC values with CIS ice chart values, including error bars. The main discrepancy is in the summer between days 192-256 (Jul 11 - Sep 13), where the CIS data reported IC up to 2.8/10 while the ACIC mostly reported OW in that timeframe.
8. 2022 (Fig. 3.10) - The year 2022 had very similar trajectories for the ACIC and CIS ice chart IC curves, though the ACIC values were lower for days 52-108 (Feb 21 - Apr 18). In the fall, there was a lower ACIC period of day 290-311 (Oct 17 - Nov 7).
9. 2023 (Fig. 3.11) - The year 2023 followed a pattern very similar to 2022. There was a period of lower ACIC from day 51-149 (Feb 20 - May 29). In the fall, there was another lower ACIC period, though most of the data points, error bars included, overlapped with the CIS ice chart data.
10. 2024 (Fig. 3.12) - There was significant variability in ACIC between day 1-141 (Jan 1 - May 20). The biggest discrepancy occurred on day 141 (May 20). In the summer, there was a small period between days 204-225 (Jul 22 - Aug 12) where the CIS ice chart data reported IC up to 2/10, while the AVHRR visible channel showed OW. In the fall, there was a lower ACIC period from day 300-344 (Oct 26 - Dec 9).

Fig. 3.13 shows the 10-year average graph for the 2015-2024 time period. Not all years had data up to day 365, so an average was not calculated at the very end of the year. In Fig. 3.13, there was a lower ACIC period in the early part of the year than the CIS ice charts data, from day 1-142 (Jan 1 - May 22), and a small lower IC period in the late fall from day 302-344 (Oct 29 - Dec 10). The error bars for ACIC data points were calculated using Eqn. 2.9 in Section 2.9.2. Error bars for SAR and AVHRR visible channel data points were set at $\pm$ 1.0 tenth based on the uncertainty method as detailed in Section 2.9.2. CIS ice chart error bars were calculated as per Eqn. 2.10 in Section 2.9.2. On the graph, where the CIS ice chart value is 9.5, that was an interpretation of the 9+ values given by the CIS ice charts, which were assigned a value of 9.5 for the research for this thesis. For the ACIC results during the coldest parts of the year, either a 9 or 10 for IC was assigned, as it was too difficult to accurately assign a 9.5 vice a 9 or 10 based on the colour spectrum. During the rest of the year onwards, the ACIC results were consistently just below the CIS ice chart results, however the error bars either touched or overlapped. Ice charts tend to be made more conservatively [22], which might explain the extended period of 9+ values in the CIS charts up to calendar day 120 (Apr 30) over a 10-year average. Overall, the difference between the two data sets ranged from 0.2-2.8 tenths, depending on the time of year. The two dates where the error bars did not touch or overlap were calendar days 92 (Apr 2) and 127 (May 7).

Fig 3.14 shows the 10-year average for the four selected locations within Lancaster Sound from west to east: Resolute, Prince Leopold Island, north of Arctic Bay, and the eastern edge of Devon Island. The data is shown without error bars for better visual clarity, since the majority of the error bars overlapped. The 10-year average IC line for all of Lancaster Sound is also shown as a comparison. Not all years had data up to day 365, so an average was not calculated at the very end of the year. Overall there was a general trend of melting in the direction from east to west in Lancaster Sound. Resolute, the westernmost point, retained an IC of at least 4/10 up to day 183 (Jul 2), which is much later in the year than the 10-year average, which drops below 4/10 IC as of day 151 (May 31). In the fall freeze season, all of Lancaster Sound freezes uniformly and rapidly, as shown between days 268-302 (Sep 25 - Oct 29), though the eastern entrance lags slightly for a short period.

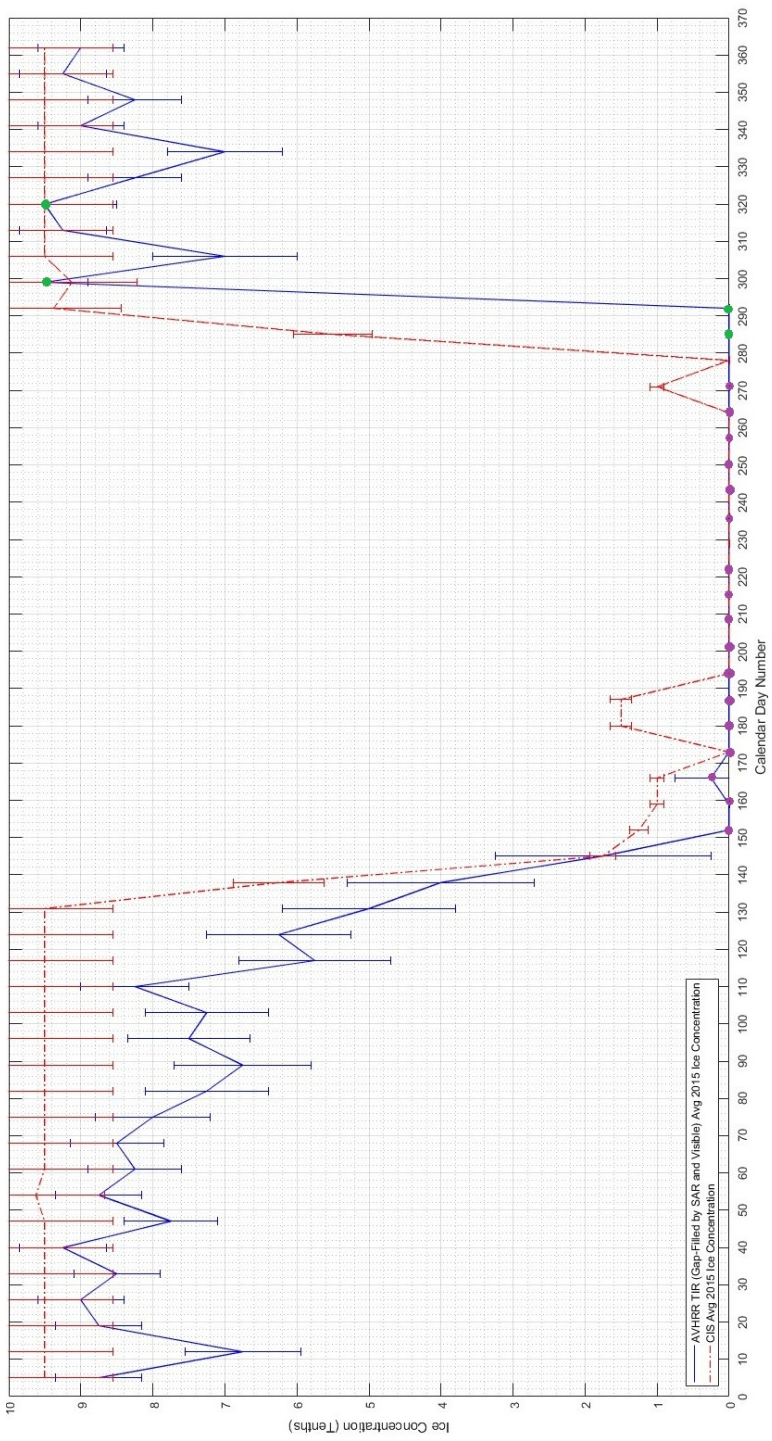

Figure 3.3: 2015 average IC results for Lancaster Sound using ACIC (gap-filled by SAR and AVHRR visible channel) and CIS ice charts. SAR used on calendar days 285, 292, 306, 320 (green dots). AVHRR visible channel used on calendar days 152-222 and 236-271 (weekly intervals)(purple dots). Days 229 and 278 had no data, but assumed as OW.

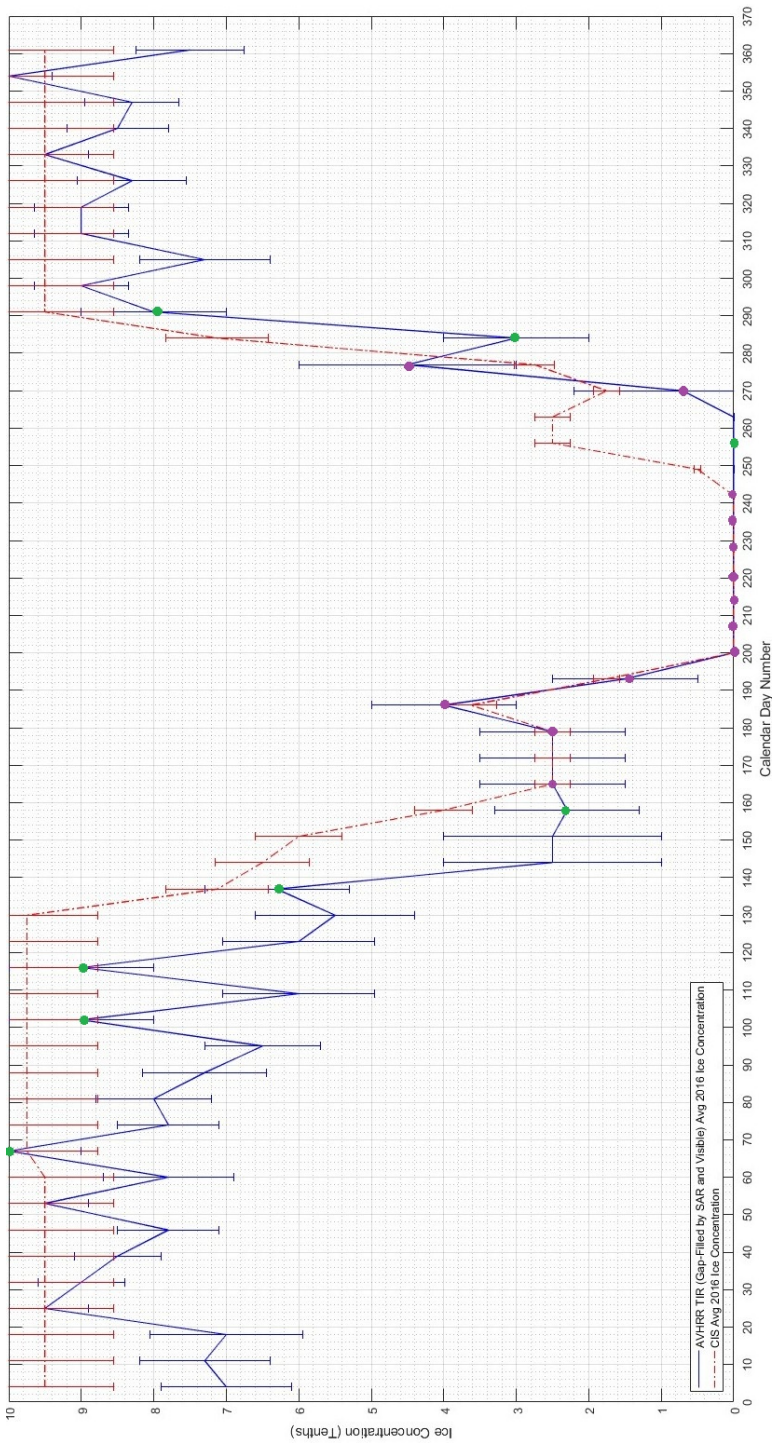

Figure 3.4: 2016 average IC results for Lancaster Sound using ACIC (gap-filled by SAR and AVHRR visible channel) and CIS ice charts. SAR used on calendar days 67, 102, 116, 137, 158, 256, 284, 291 (green dots). AVHRR visible channel used on calendar days 165, 179-242 (weekly intervals), 270, 277 (purple dots). Day 249 had no data, but assumed as OW. Day 172 and 179 had insufficient data, so concentration assumed same as day 165. For day 256 and 263, no data on Resolute in SAR image.

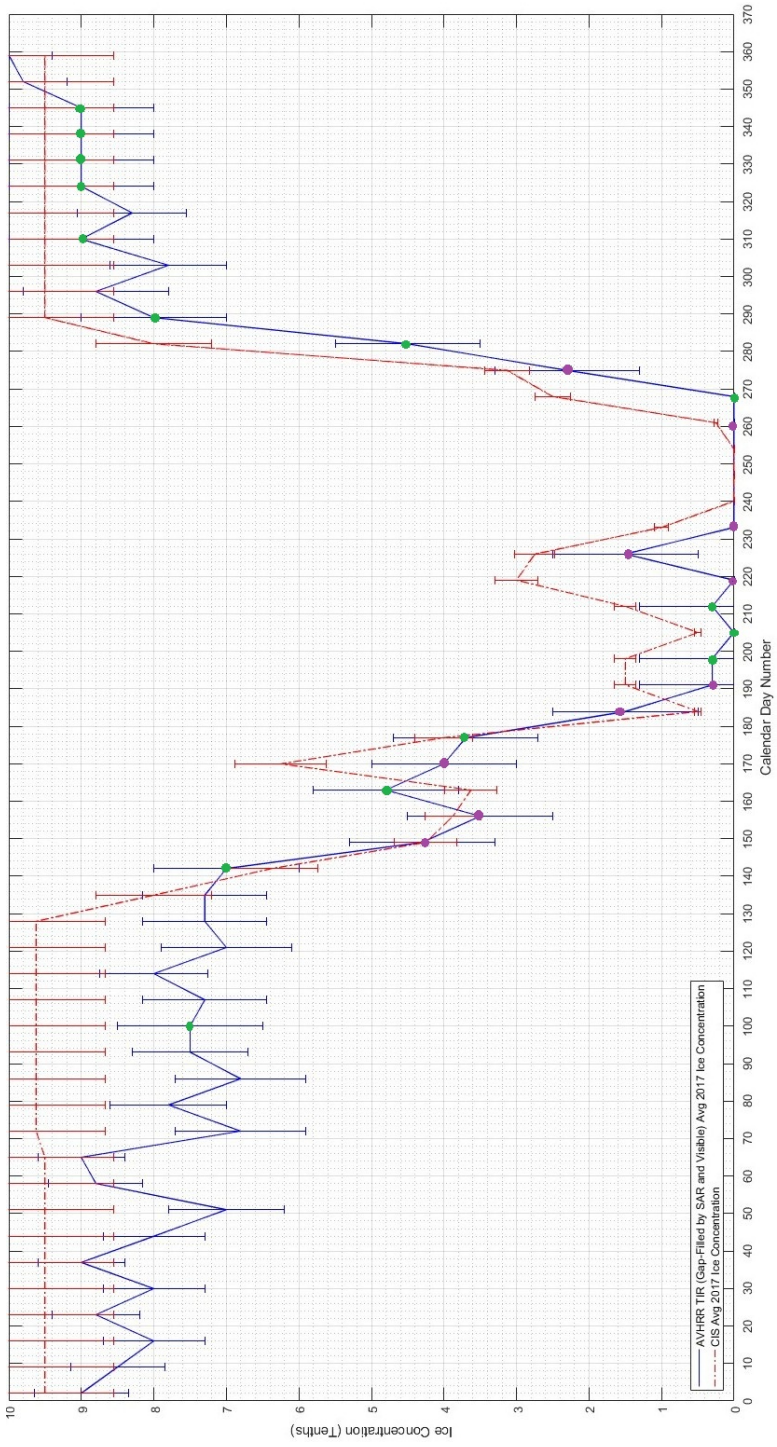

Figure 3.5: 2017 average IC results for Lancaster Sound using ACIC (gap-filled by SAR and AVHRR visible channel) and CIS ice charts. SAR used on calendar days 100, 142, 163, 177, 198, 205, 212, 268, 282, 289, 296, 310, 324, 331, 338, 345 (green dots). AVHRR visible channel used on calendar days 149, 156, 170, 184, 191, 219, 226, 233, 261, 275 (purple dots). Days 240, 247 and 254 had no data, so assumed as OW.

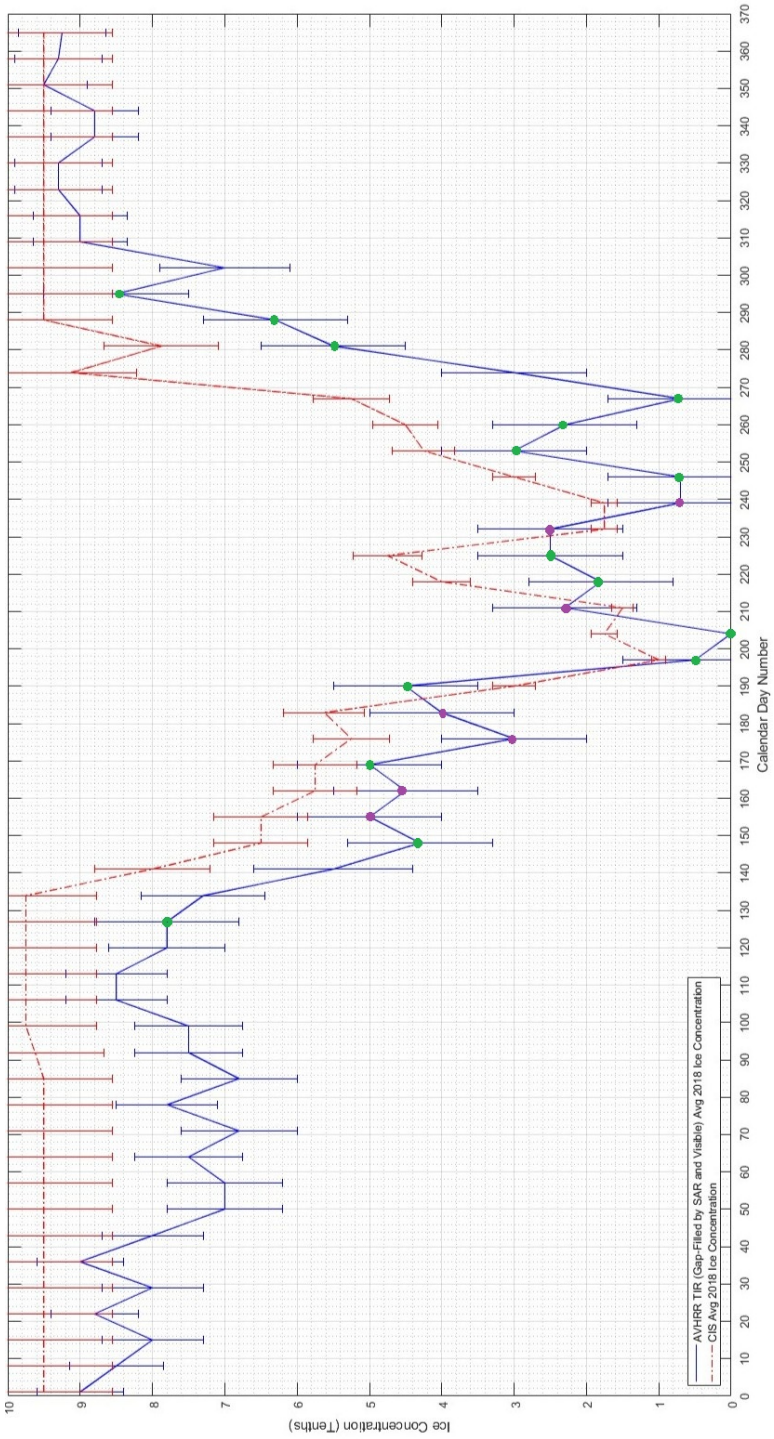

Figure 3.6: 2018 average IC results for Lancaster Sound using ACIC (gap-filled by SAR and AVHRR visible channel) and CIS ice charts. SAR used on calendar days 127, 148, 169, 190, 197, 204, 218, 225, 246, 253, 260, 267, 281, 288, 295 (green dots). AVHRR visible channel used on calendar days 155, 162, 176, 183, 211, 232, 239 (purple dots).

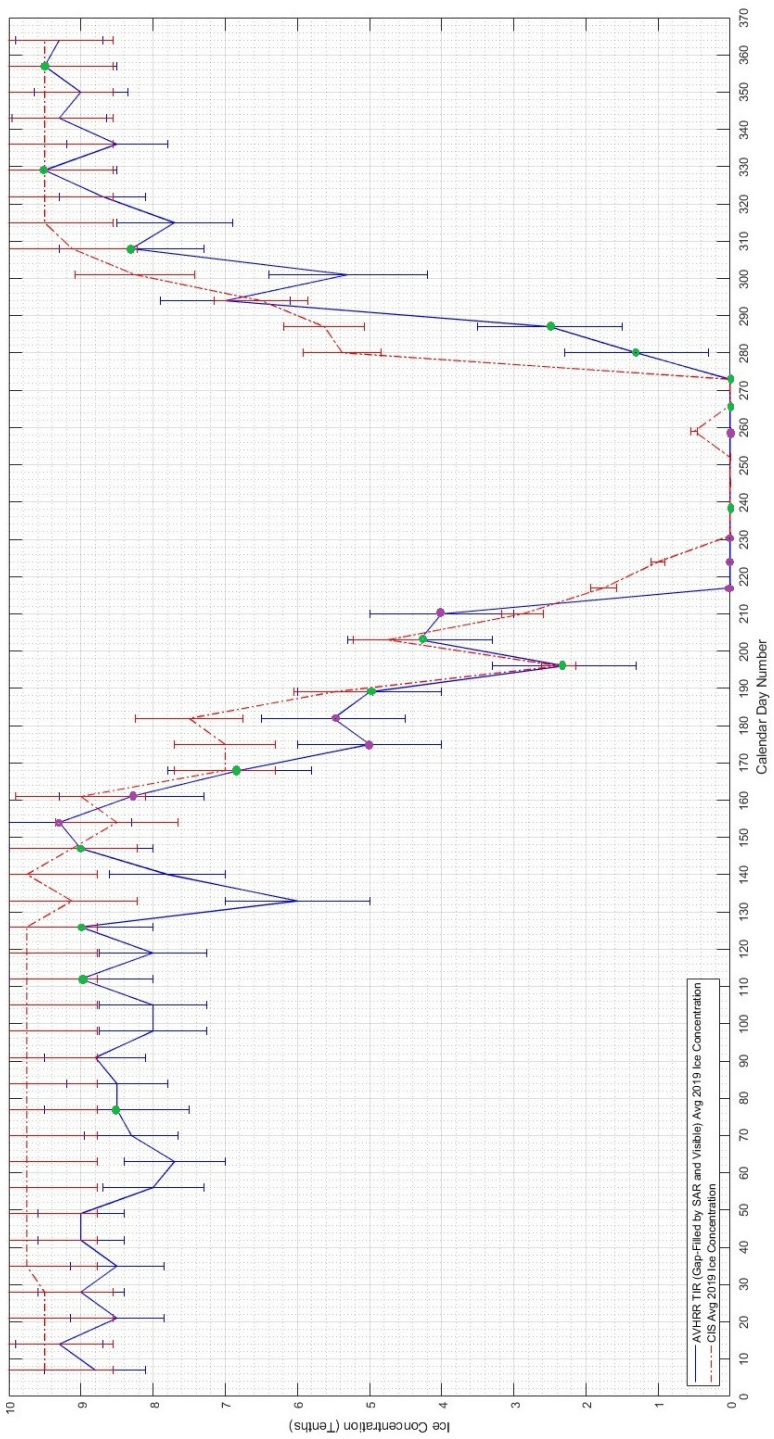

Figure 3.7: 2019 average IC results for Lancaster Sound using ACIC (gap-filled by SAR and AVHRR visible channel) and CIS ice charts. SAR used on calendar days 77, 112, 126, 147, 168, 189, 196, 203, 238, 266, 273, 280, 287, 308, 329, 357 (green dots). AVHRR visible channel used on calendar days 154, 161, 175, 182, 210, 217, 224, 231, 259 (purple dots). Days 245 and 252 had no data, so assumed as OW.

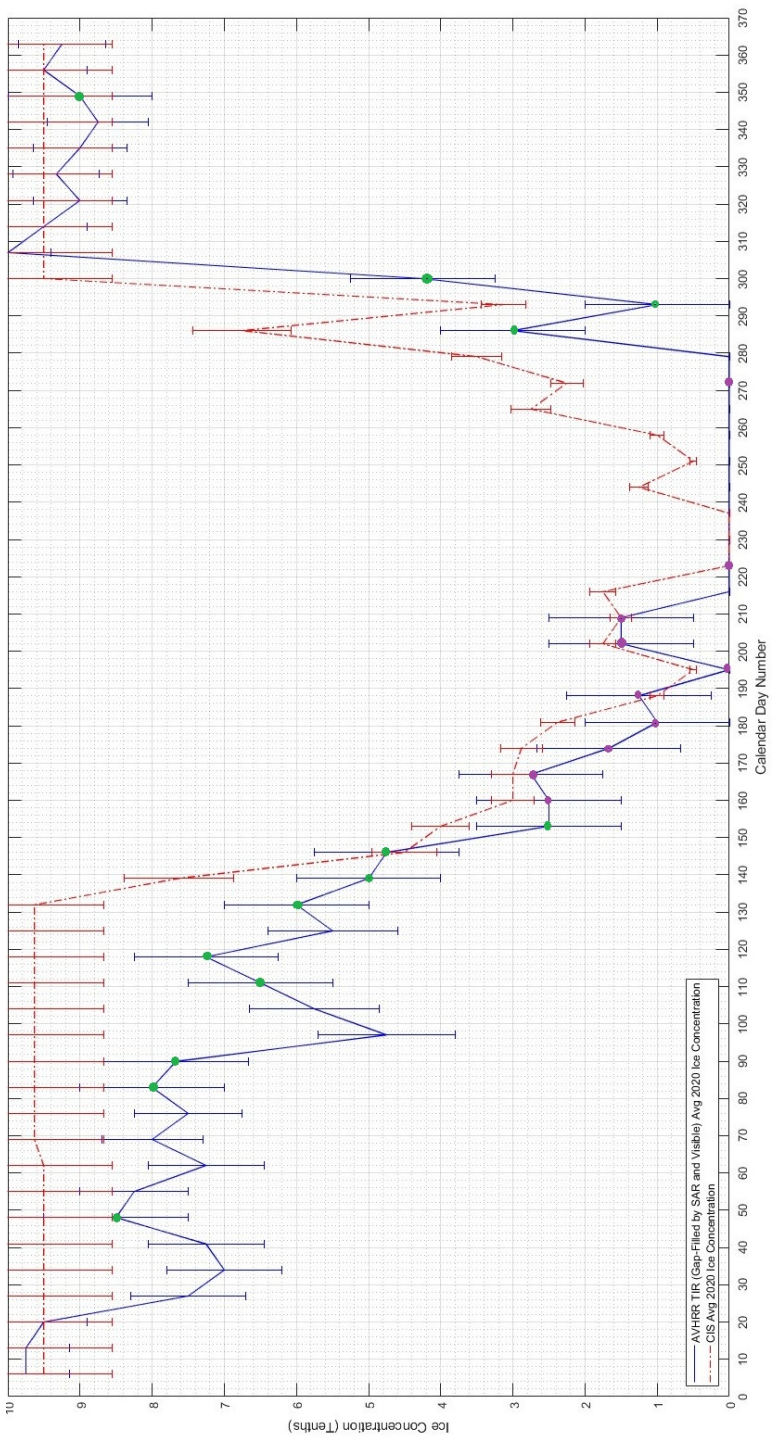

Figure 3.8: 2020 average IC results for Lancaster Sound using ACIC (gap-filled by SAR and AVHRR visible channel) and CIS ice charts. SAR used on calendar days 48, 83, 90, 111, 118, 132, 139, 146, 153, 286, 293, 300, 349 (green dots). AVHRR visible channel used on calendar days 160-209 (weekly intervals), 223, 272 (purple dots). Days 216, 230-265 (weekly interval) and 279 had no data, so assumed as OW. Day 335 had no data, so used average IC between week prior and after.

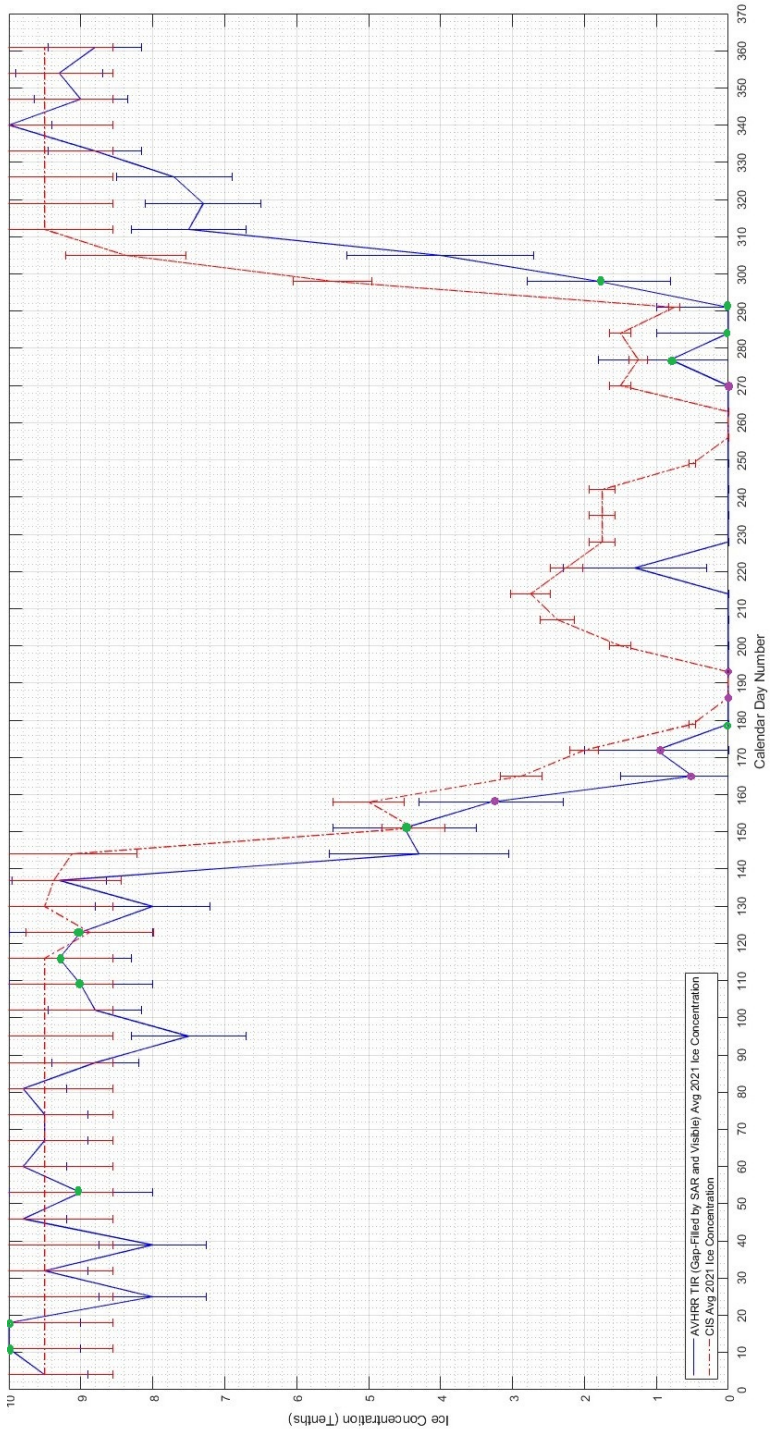

Figure 3.9: 2021 average IC results for Lancaster Sound using ACIC (gap-filled by SAR and AVHRR visible channel) and CIS ice charts. SAR used on calendar days 11, 18, 53, 109, 116, 123, 151, 179, 277, 284, 291, 298 (green dots). AVHRR visible channel used on calendar days 158, 165, 172, 186, 193, 270 (purple dots). Days 200, 207, 214, 228-263 (weekly intervals) had no data, so assumed as OW.

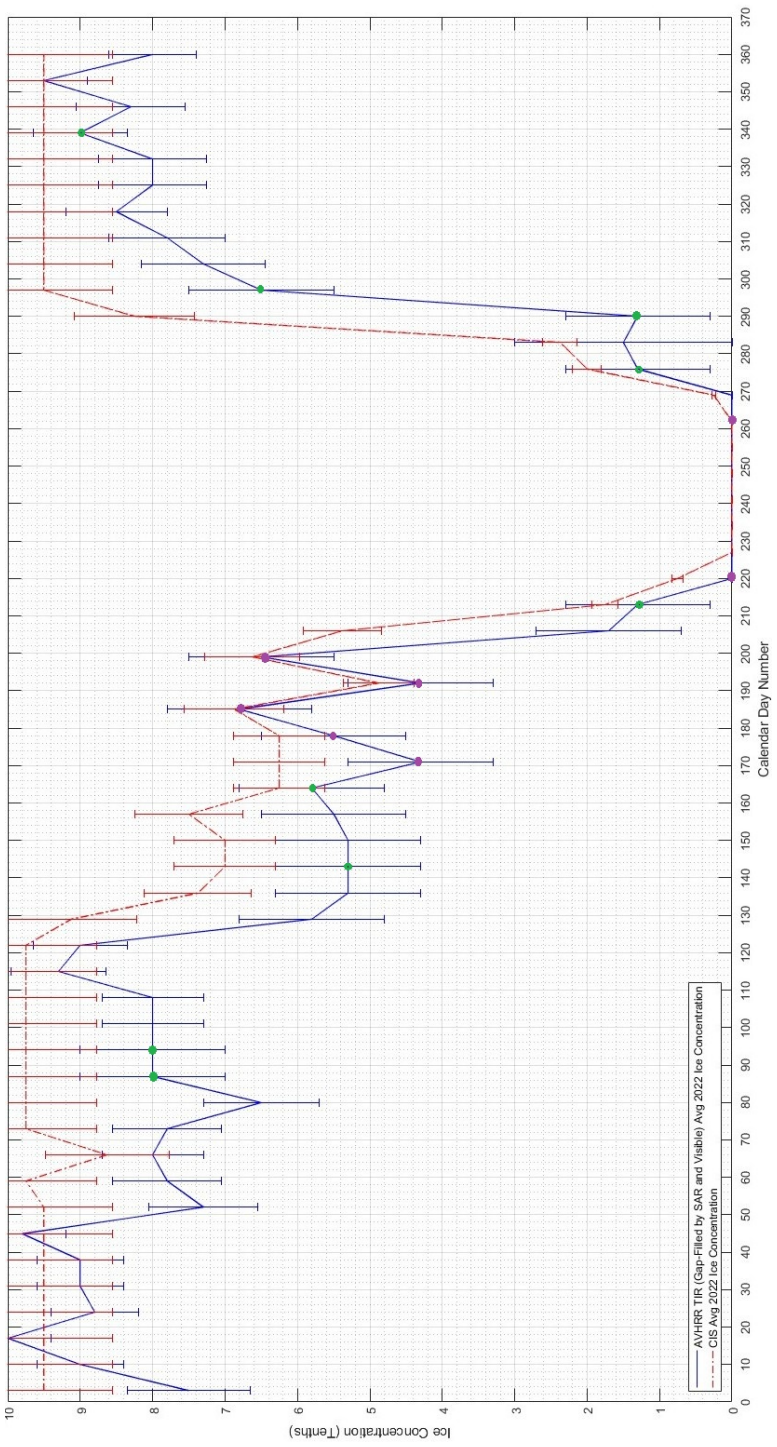

Figure 3.10: 2022 average IC results for Lancaster Sound using ACIC (gap-filled by SAR and AVHRR visible channel) and CIS ice charts. SAR used on calendar days 87, 94, 143, 164, 213, 276, 290, 297, 339 (green dots). AVHRR visible channel used on calendar days 171-206 (weekly intervals), 220, 262 (purple dots). Days 227-255 (weekly intervals) and 269 had no data, so assumed as OW.

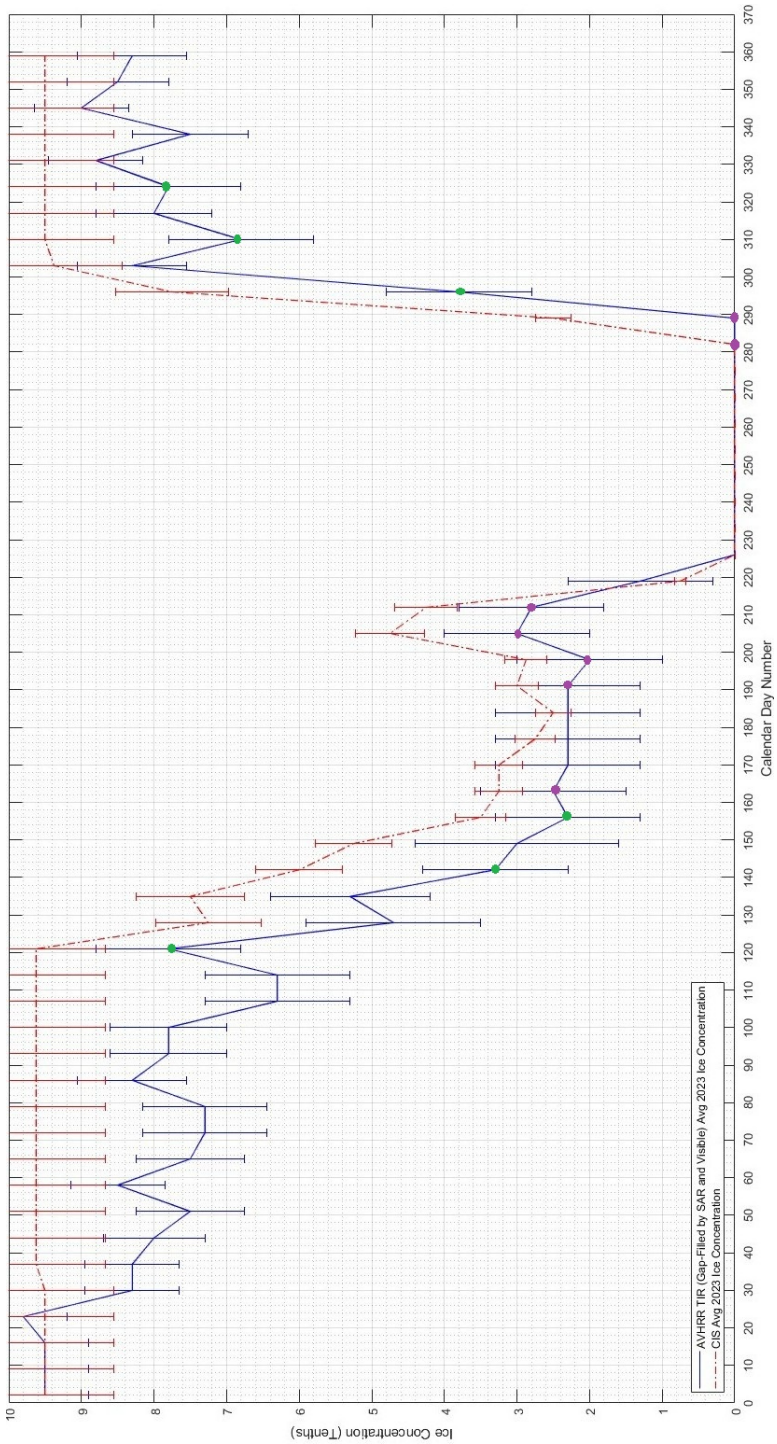

Figure 3.11: 2023 average IC results for Lancaster Sound using ACIC (gap-filled by SAR and AVHRR visible channel) and CIS ice charts. SAR used on calendar days 121, 142, 156, 296, 310, 324 (green dots). AVHRR visible channel used on calendar days 163, 191, 198, 205, 212, 282, 289 (purple dots). Days 170, 177 and 184 had no data, but IC assumed same as day 191. Days 219, 233, 240, 247, 254, 275 had no data, so assumed as OW.

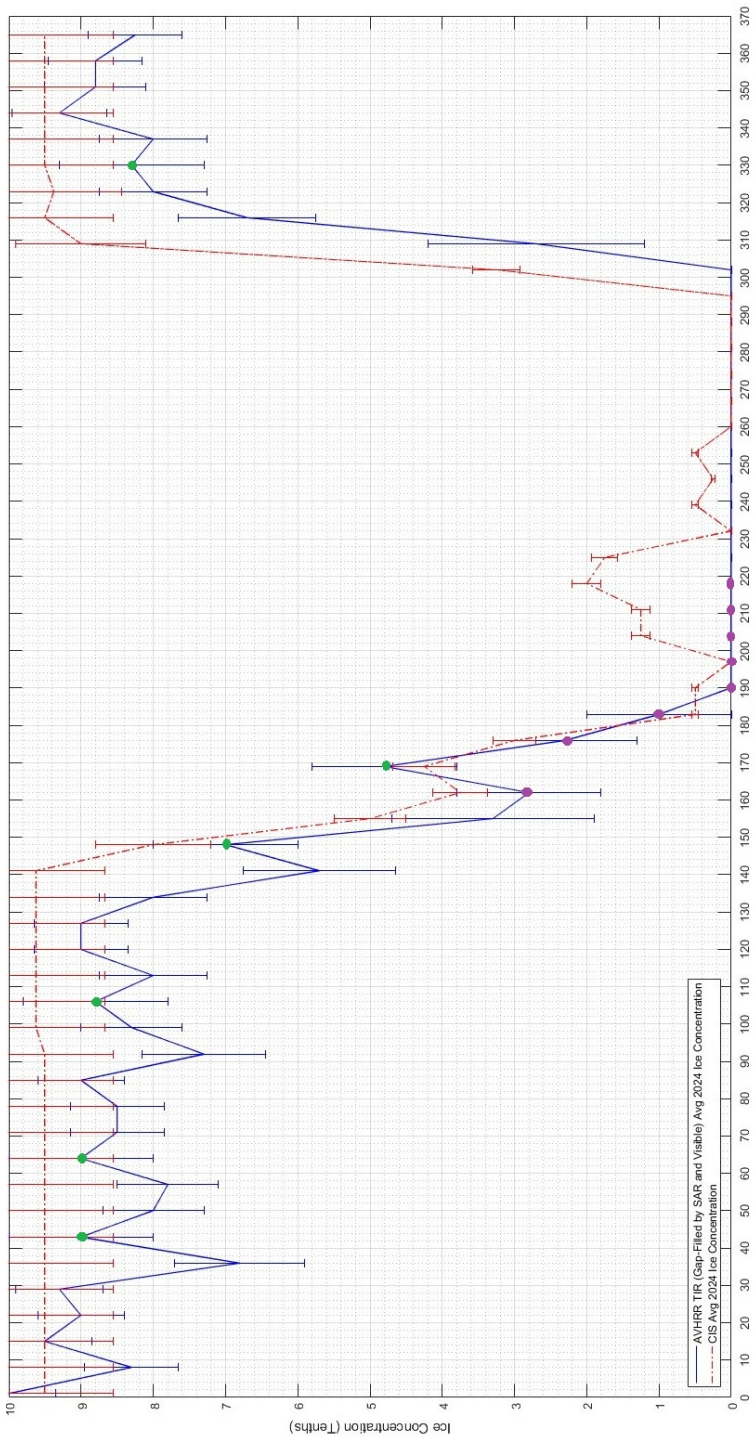

Figure 3.12: 2024 average IC results for Lancaster Sound using ACIC (gap-filled by SAR and AVHRR visible channel) and CIS ice charts. SAR used on calendar days 43, 64, 106, 148, 169, 330 (green dots). AVHRR visual used on calendar days 162, 176-218 (weekly intervals)(purple dots). Days 225, 232, 239, 246, 260, 267, 281, 295, 302 had no data so assumed as OW.

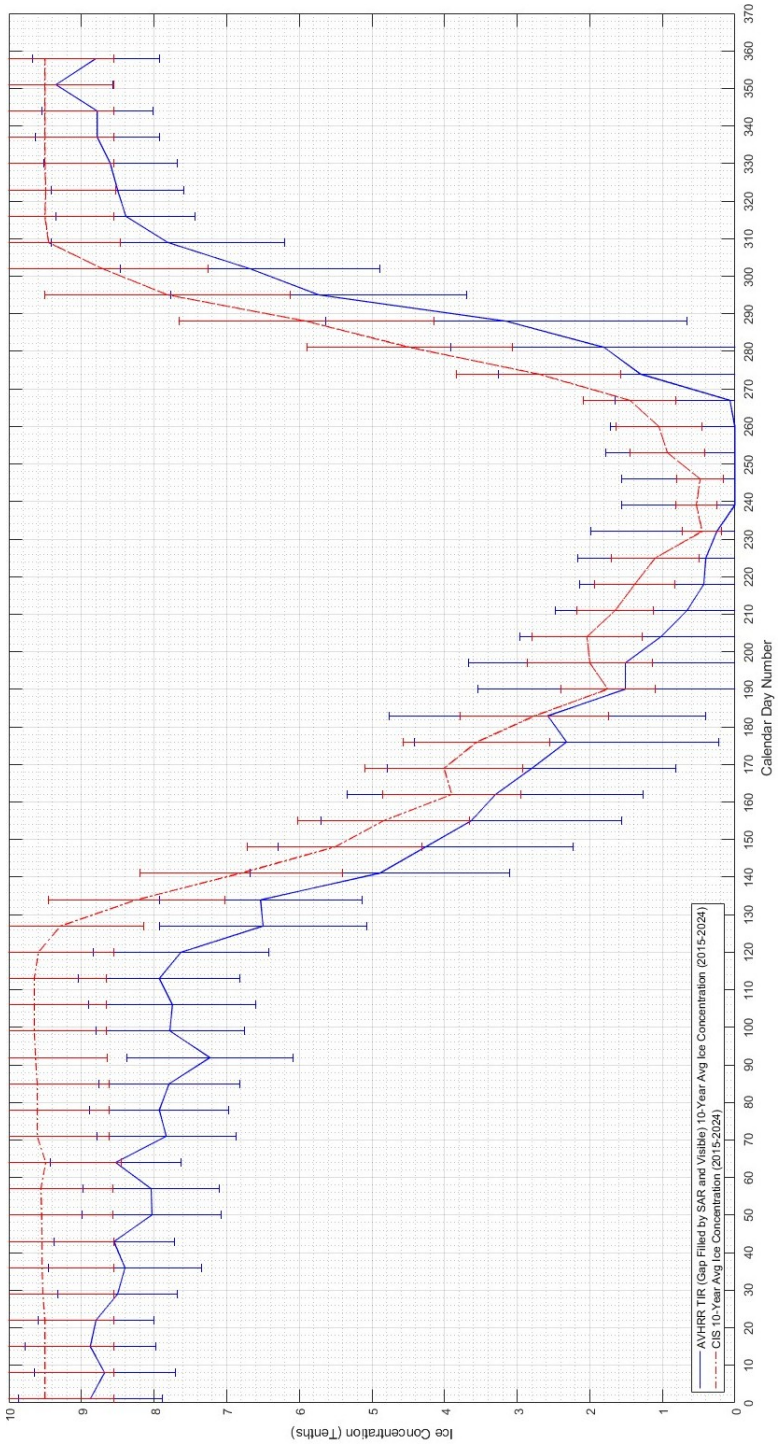

Figure 3.13: 10-year average (2015-2024) IC results for Lancaster Sound using ACIC (gap-filled by SAR and AVHRR visible channel) and CIS ice charts. For the CIS IC near 9.5, the CIS charts state 9+, which was set as 9.5 for this study. Not all years had data for day 365, so this data was not shown. Including uncertainty ranges, all data points overlapped except for days 92 (Apr 2) and 127 (May 7).

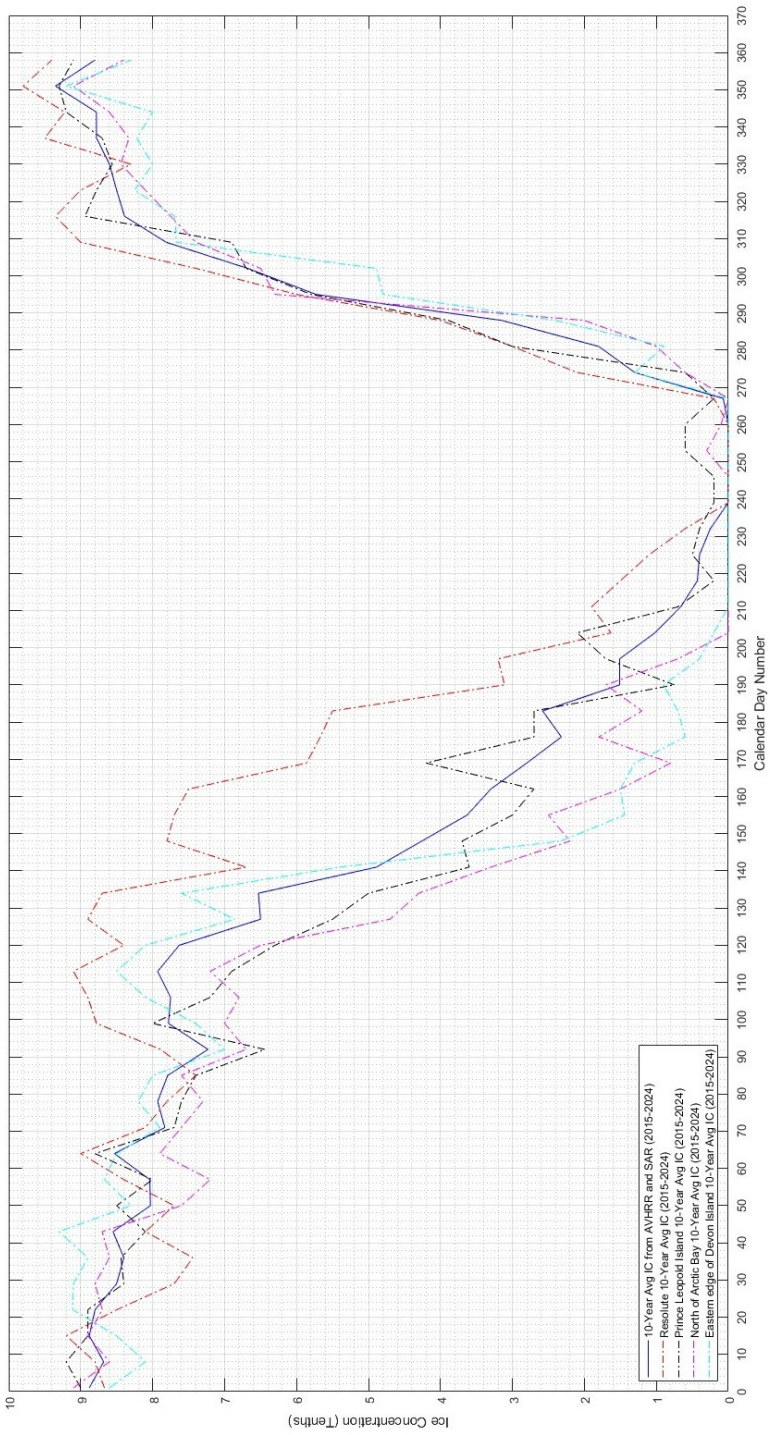

Figure 3.14: 10-Year average (2015-2024) ACIC (gap-filled by SAR and AVHRR visible channel) results for four locations in Lancaster Sound: Resolute, Prince Leopold Island, north of Arctic Bay, and eastern edge of Devon Island (ordered west to east). Error bars were removed for more clarity, as there was significant overlap.

3.2.2 Important Start/End Dates & ACIC Time of Year Limits

In the spring, the ACIC stopped working due to warm ocean temperatures between approximately 5-15 days before the ice arch collapses, depending on the year. According to the ACIC details in the Technical Note [51] in Appendix A, ACIC was expected to stop working in the spring/summer once SST $>$ -1.8° C. From analysis, this was confirmed, and it also corresponded to when the temperature of the snow/ice pack, used for $b9$ in Eqn. 2.7, was approximately $>$ -3° C, as shown in Fig. 3.15.

The ACIC begins to work again in late September or early October, within 10-15 days after full OW season has concluded, except for years 2017 and 2018. The start of full OW also starts after the ice arch collapses, except for 2021, where the ice arch formed west of Resolute, which was outside the defined Lancaster Sound ROI for the research for this thesis. Table 3.2 provides 10-year averages and standard deviations of important start/end dates from 2015-2024 such as time of year limits for the ACIC, ice arch formation and collapse dates, and full OW start and end dates. Fig. 3.16 shows the same information as Table 3.2, but on a yearly basis, with data uncertainties set at $\pm$ 3 days.

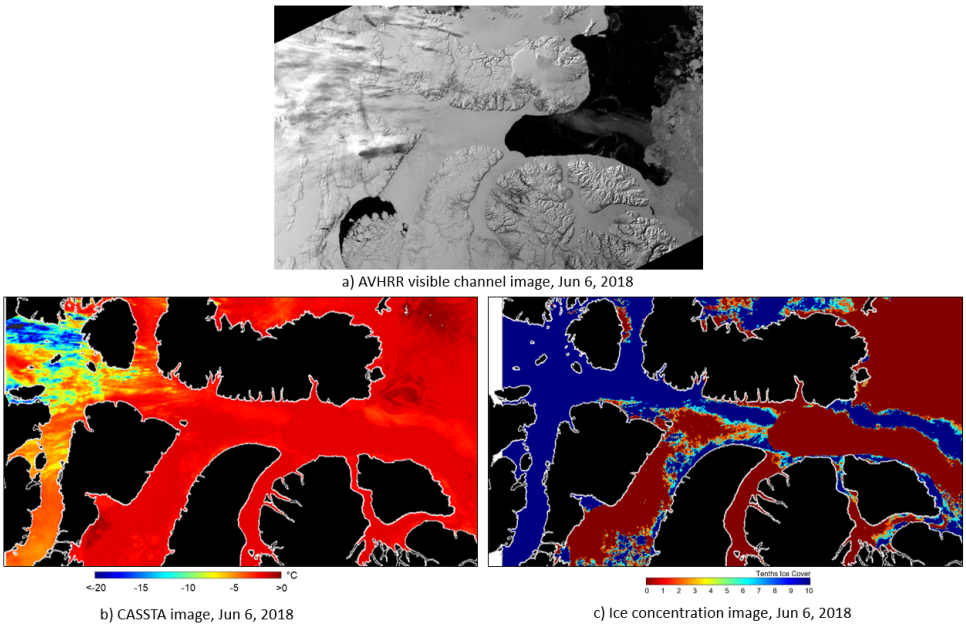

Figure 3.15: ACIC workable limit reached in 2018 on Jun 6: a) AVHRR visible channel shows presence of an ice arch, b) CASSTA SSTs near 0° C, and c) ACIC image generated, where the temperature of the ice pack was -2.2° C. This correlates an approximate ice pack temperature limit of -3° C to a SST limit of -1.8° C. Land mask was applied to b) and c).

Table 3.2: 10-year average ACIC time of year limits, ice arch formation/collapse dates, and full OW start/end dates, 2015-2024

	Day IC Algorithm Stopped Working	Day IC Algorithm Worked Again	Ice Arch Formation Day #	Ice Arch Collapse Day #	Full OW Start Day #	Full OW End Day #
Avg	161	298	60	181	207	270
Std Dev	5	10	32	12	14	26
Date	Jun 10	Oct 25	Mar 1	Jun 30	Jul 26	Sep 27

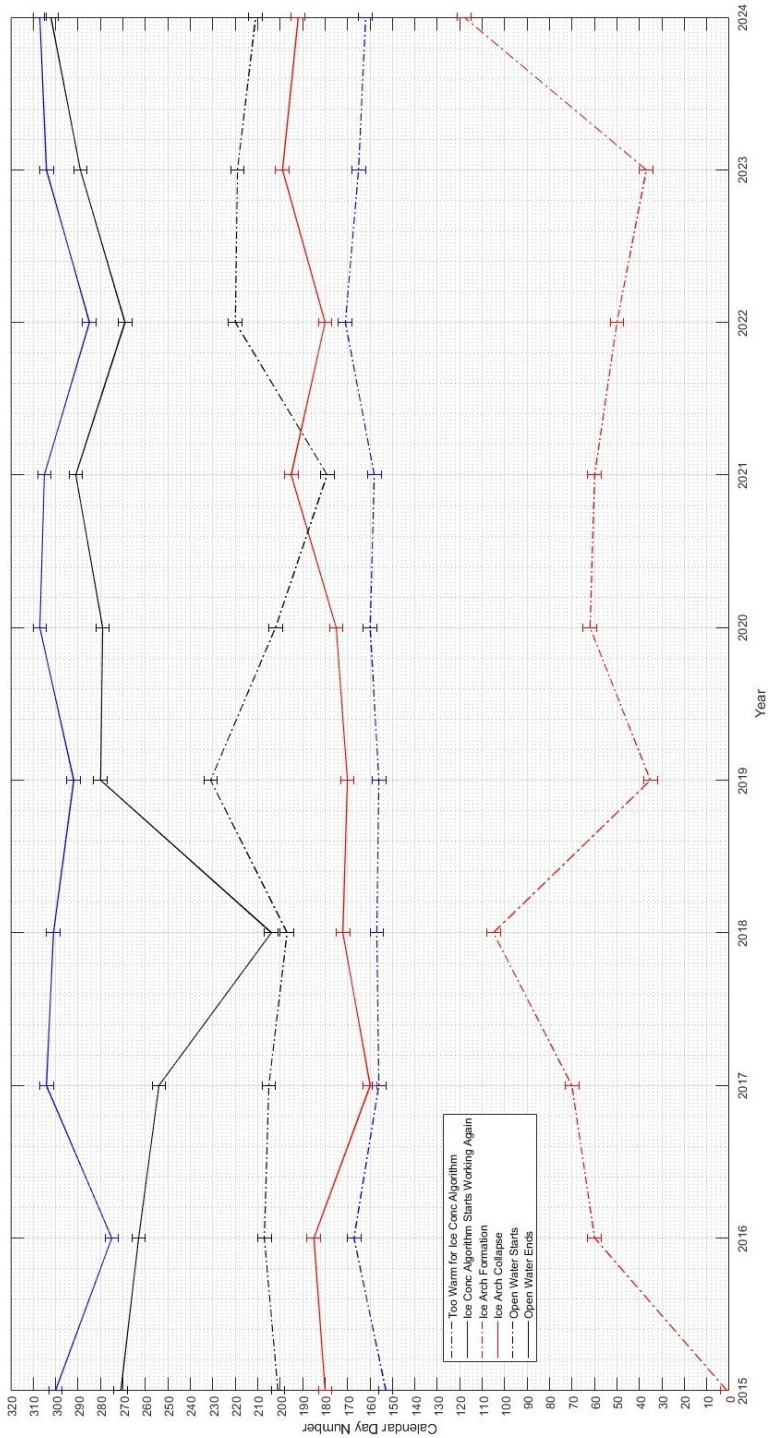

Figure 3.16: Important start/end dates in Lancaster Sound (2015-2024): ice arch formation/collapse, open water start/end, and ACIC working limits. In 2021, the ice arch formed west of Resolute and beyond the Lancaster Sound, which is why OW starts before ice arch collapse that year.

3.2.3 Seven-Day Continuous ACIC Results

The time period of April 1-7, 2023 (calendar days 91-97), Jan 31 - Feb 6, 2017 (days 31-37) and Mar 12-18, 2018 (days 71-77) were used as seven-day continuous non-cloudy periods to analyze with the CASSTA and ACIC, to see how fast changes occurred from day to day. During the April 1-7, 2023 time period, the ice arch was starting to form. Fig. 3.17 shows the ACIC results per day at near-concurrent times of day, and Fig. 3.18 shows the U Bremen AMSR-2 PM-based results for the same days. The ACIC images, Fig. 3.17, showed the formation of the ice arch much more clearly than the U Bremen IC images in Fig. 3.18.

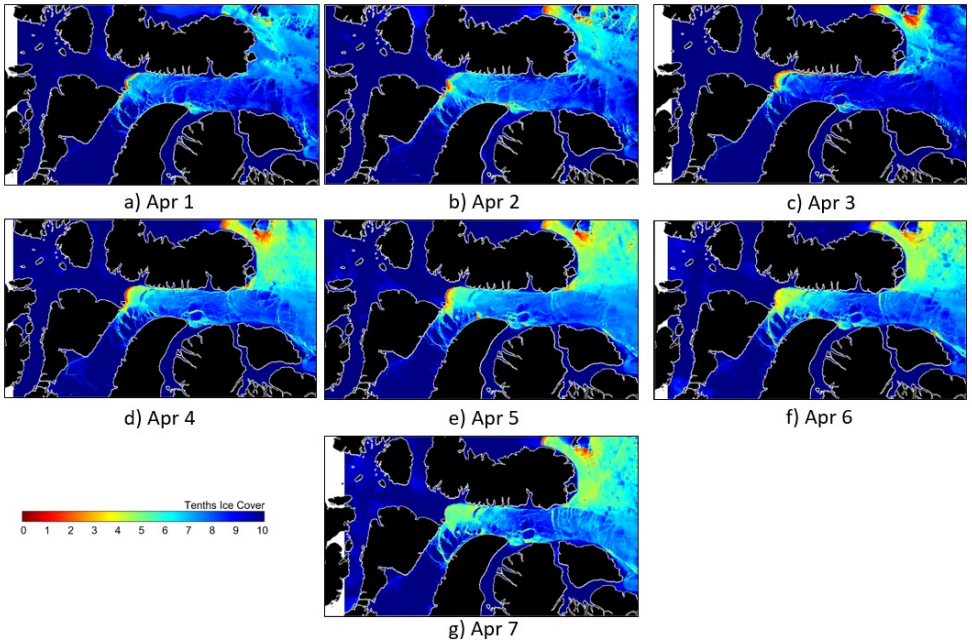

Figure 3.17: April 1-7, 2023 (calendar days 91-97) seven-day continuous ACIC results in Lancaster Sound at near-concurrent times of day. Blank white areas means that the ACIC image did not fill the entire area that the black land mask template covers.

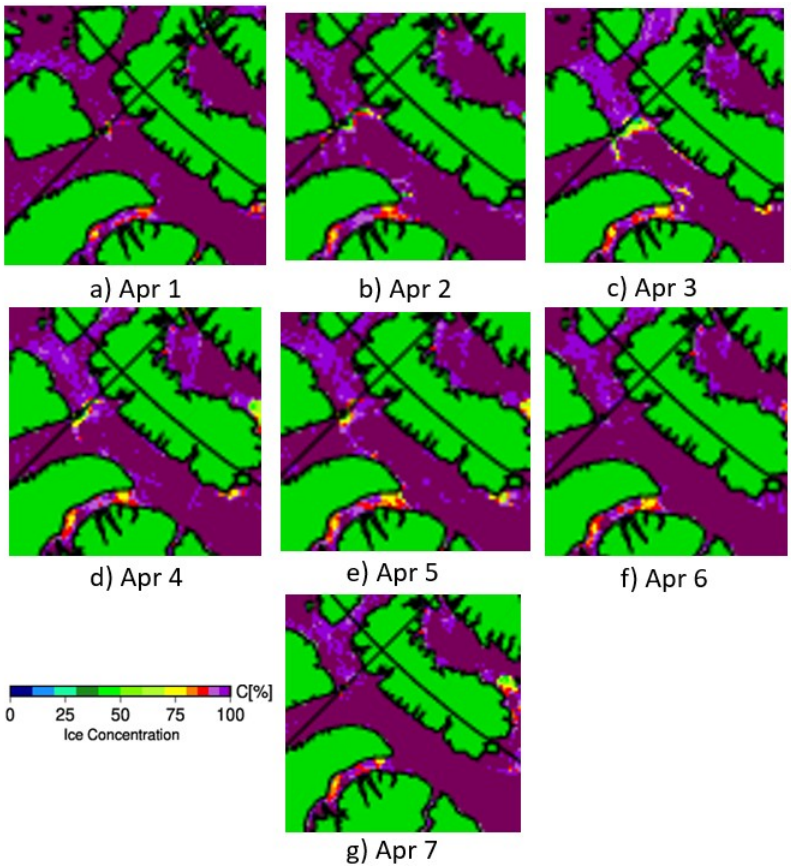

Figure 3.18: April 1-7, 2023 (calendar days 91-97) seven-day continuous U Bremen AMSR-2 PM-based IC results in Lancaster Sound (images sourced from [71]).

For the Jan 31 - Feb 6, 2017 time period, the ice arch has not yet formed, but the IC in Lancaster Sound was very high. Fig. 3.19 shows the ACIC results per day at near-concurrent times of day, and Fig. 3.20 shows the U Bremen AMSR-2 PM-based results for the same days. The same IC changes can be seen around Resolute and Prince Leopold Island in both image types. The ACIC images in Fig. 3.19 show more ice detail in the rest of the Sound compared to the U Bremen IC images in Fig. 3.20 due to better spatial resolution of 1.1 km vs 6.25 km.

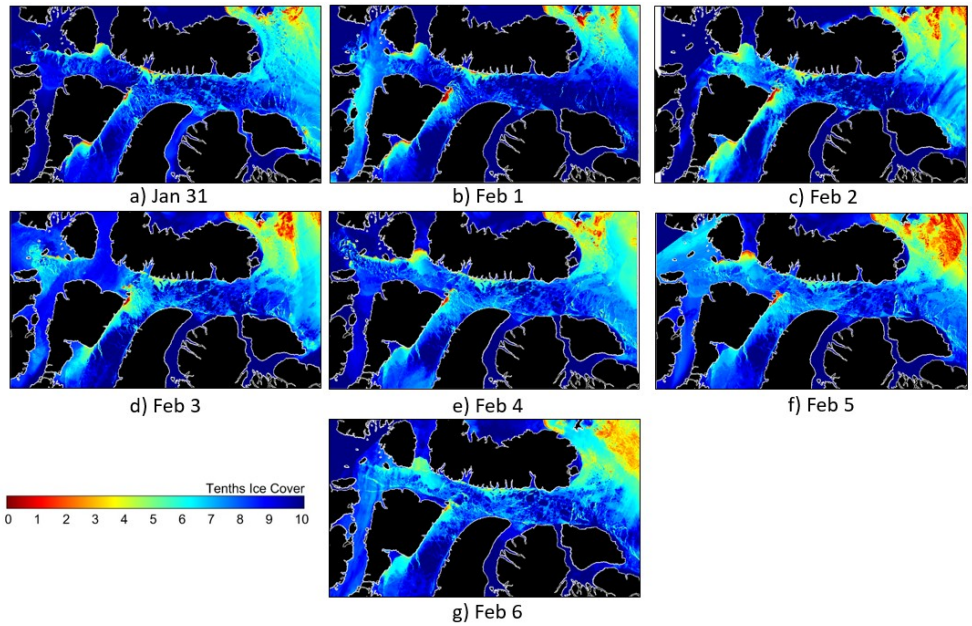

Figure 3.19: Jan 31 - Feb 6, 2017 (calendar days 31-37) seven-day continuous ACIC results in Lancaster Sound at near-concurrent times of day. Blank white areas means that the ACIC image did not fill the entire area that the black land mask template covers.

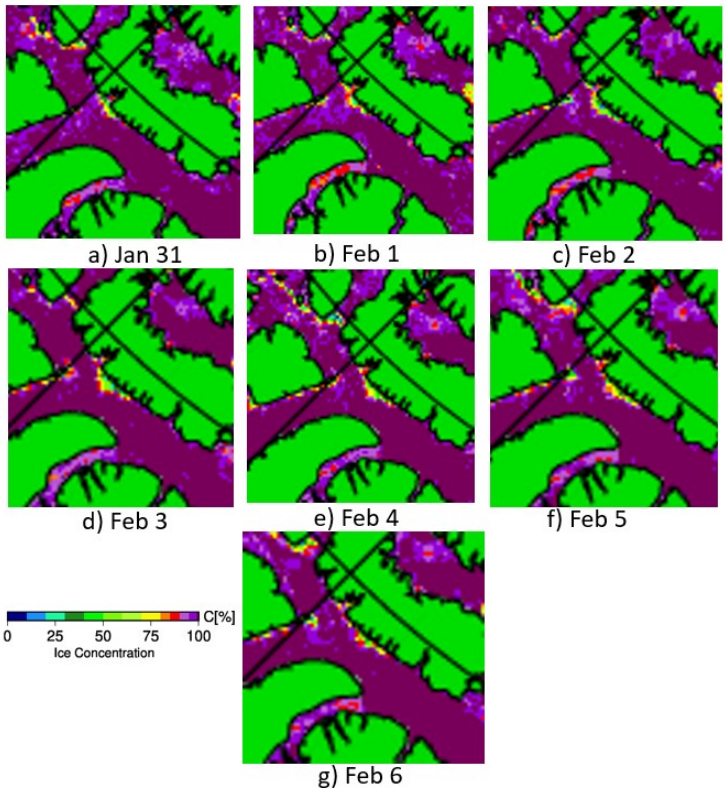

Figure 3.20: Jan 31 - Feb 6, 2017 (calendar days 31-37) seven-day continuous U Bremen AMSR-2 PM-based IC results in Lancaster Sound (images sourced from [71]).

For the Mar 12-18, 2018 time period, the ice arch had not yet formed. The IC was high, in the 7-9/10 range, but lower than the CIS ice chart value of 9+/10 during the same time period. Fig. 3.21 shows the ACIC results per day at near-concurrent times of day, and Fig. 3.22 shows the U Bremen AMSR-2 PM-based results for the same days. The ACIC images, Fig. 3.21, show more ice detail in the rest of the Sound compared to the U Bremen IC images in Fig. 3.22.

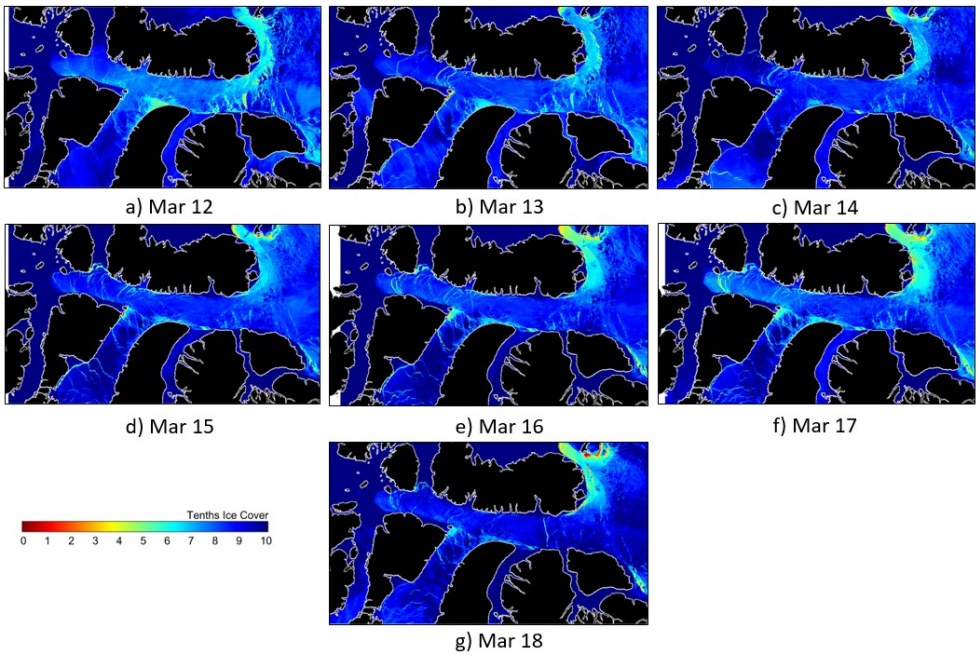

Figure 3.21: Mar 12-18, 2018 (calendar days 71-77) seven-day continuous ACIC results in Lancaster Sound at near-concurrent times of day. Blank white areas means that the ACIC image did not fill the entire area that the black land mask template covers.

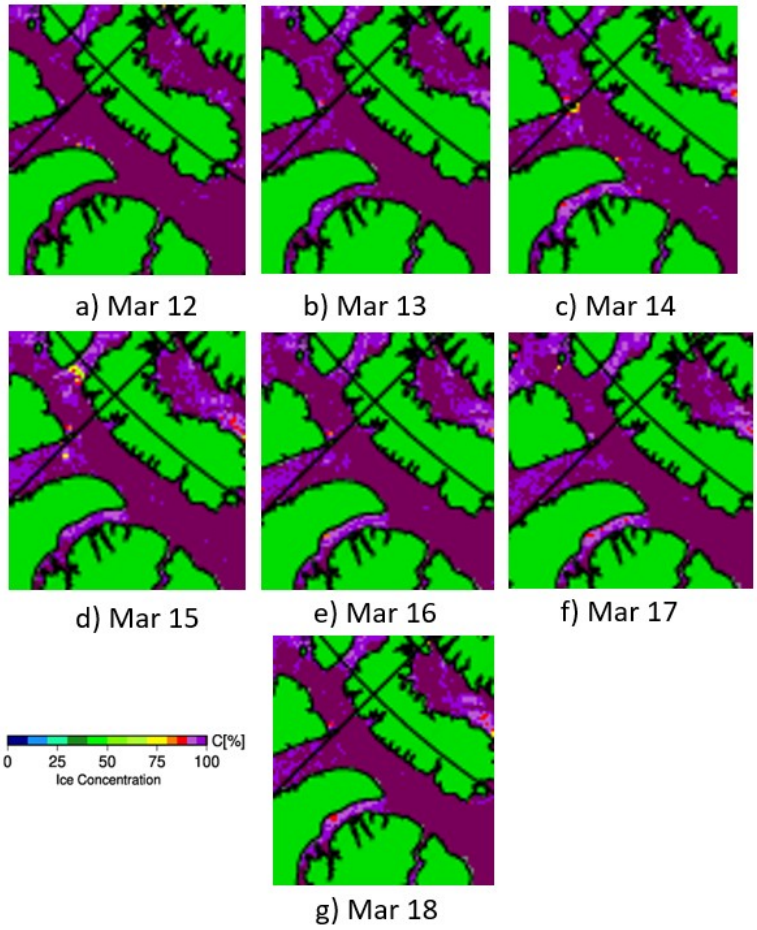

Figure 3.22: Mar 12-18, 2018 (calendar days 71-77) seven-day continuous U Bremen AMSR-2 PM-based IC results in Lancaster Sound (images sourced from [71]).

3.3 AVHRR Visible Channel/Band Isodata and Visual IC Results

For times of year in May/June and September, when it was both too warm for the ACIC to provide accurate results and no SAR image was available, there was sufficient daylight to view channel 1 (visible band) in the non-cloudy AVHRR images of Lancaster Sound. IC estimates in this case were made based on either visual analysis of the image with the aid of the ice

guide images in Fig. 1.8, or via isodata unsupervised classification in ENVI. An example of a day that was conducive to visible channel analysis alone was Jun 5, 2017 (calendar day 156), shown in Fig. 3.23. IC was determined to be 10, 0, 3 and 1 at the four respective selected points: Resolute, Prince Leopold Island, north of Arctic Bay, and the eastern edge of Devon Island (locations shown in Fig. 2.4). The values were selected based on the ice guide images in Fig. 1.8.

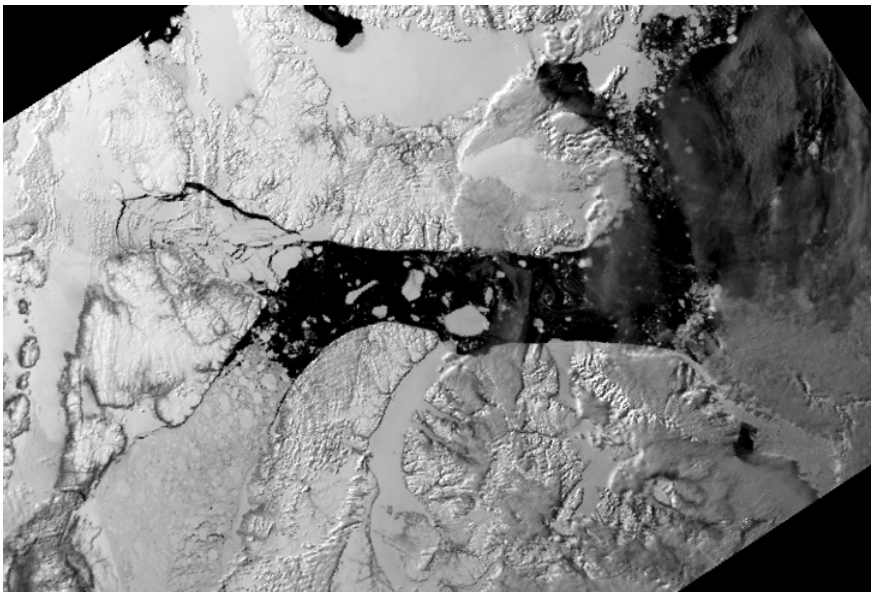

Figure 3.23: Example of a AVHRR MetOp-A channel 1 (visible channel) georeferenced image of Lancaster Sound (Jun 5, 2017 at 23:09 GMT), where IC could be determined visually.

Isodata analysis in ENVI was done on days when it was difficult to determine the IC both visually and with the aid of the ice guide in Fig. 1.8. Fig. 3.24 is an example of the isodata results for Jun 23, 2018 (calendar day 174). After testing some iterations, the selected isodata settings were 3 to 5 classes, 3 iterations, 3 pixels min per class, and 5% change threshold. A selected area in each AVHRR image was chosen without containing land. Sometimes the entire Sound could not be captured within this box. Fig. 3.24 a) shows the AVHRR image and the red box. Fig. 3.24 b) shows the isodata results, where class 1 was red, class 2 was green, class 3 was blue, and class 4 was yellow. From examining the image, it was determined that red was OW, and green,

blue and yellow were ice. The different characteristics of the ice were not required for this analysis. Analyst interpretation of each isodata results was required to determine if just red was OW, or if additional colours also represented OW. For Fig. 3.24 b), the OW value was 42%, meaning the IC was 58% in the overall area, which visually appears reasonable compared to Fig. 3.24 a) and c). Overall the isodata method worked reasonably well to give an overall IC percentage within the studied red box, however it did require analyst interpretation of the identified class colours and which combinations were ice or OW. The uncertainty on both AVHRR visible channel isodata and visual inspection results was set as an assumed conservative value of 1.0 tenths, as per Section 2.9.2, due to the results obtained from the isodata unsupervised classification and the lower precision of those results.

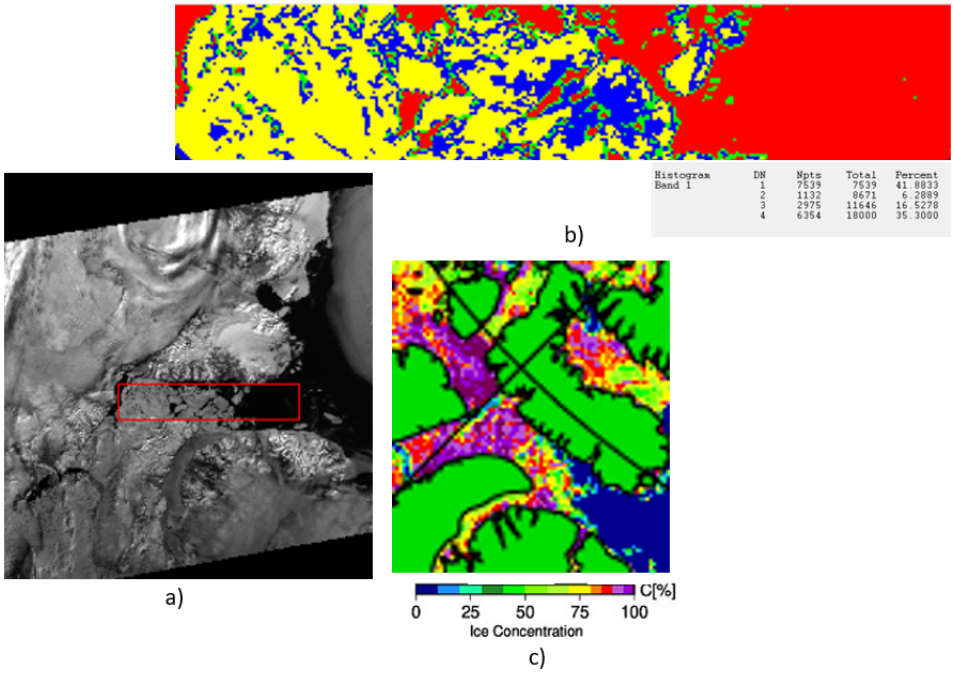

Figure 3.24: Isodata results for the AVHRR visible channel MetOp-A image on Jun 23, 2018 at 00:41 GMT: a) the red box is the selected non-land section in the AVHRR visible channel image of Lancaster Sound that was analyzed, b) isodata colour results for the red box area (red is class 1 and OW, and the other colours are ice), along with band colour percentages, and c) U Bremen AMSR-2 PM IC results (image sourced from [71]) for the same area.

3.4 SAR Isodata IC Results for 2015-2024

3.4.1 Sentinel-1 Results 2015-2019

Isodata unsupervised classification in ENVI was used to analyze the Sentinel-1A/B EW HH polarized images. The process generally produced consistent class colours, where red was OW, and sometimes green and blue was also OW. As with the AVHRR visible channel isodata analysis, the settings were: number of classes set as min 3 to max 5, with 3 iterations, 3 min pixels per class, and a change threshold of 5%. Overall isodata classification was able to differentiate OW and ice during times of year when there was a good mix of both. It did not work when the Sound was practically ice covered, nor did it work when the Sound was fully OW. Isodata worked acceptably on the following dates (just red as OW unless otherwise specified):

1. 2015: Nov 1, Nov 16. Note: no spring SAR images were required;
2. 2016: April 24, May 14, Jun 7 – but rain cloud issue, Oct 9;
3. 2017: May 22, Jun 12 (red and green as OW), Jun 25 – but rain cloud issue, Oct 23, Nov 6, Nov 20, Nov 27, Dec 3;
4. 2018: May 7, May 28, Oct 7, Oct 15, Oct 21; and
5. 2019: Apr 21, May 5, Nov 5, Nov 25, Dec 23 – even with lots of ice.

Overall, the isodata method seemed to work near end of May and late October/early November, depending on IC, which was advantageous since this was near the melt and freeze seasons. Some Sentinel-1 images had cloud-like rain areas partially obstructing Lancaster Sound such as Jun 7, 2016 or Jun 12, 2017, as shown in Fig. 3.25. It was difficult to tell what was beneath it from just looking at the SAR image, though this phenomenon did not occur often in the studied images.

Fig. 3.26 shows the Sentinel-1 HH polarized EW decibel γ^0 SAR image of a section of Lancaster Sound on May 22, 2017. EW images have a spatial resolution of 20 m x 40 m. Fig. 3.27 shows the isodata results for the Sentinel-1 SAR image on May 22, 2017 from Fig. 3.26. Fig. 3.27 a) shows the SAR image with a red box outlining the selected non-land section of Lancaster Sound that was analyzed. Fig. 3.27 b) are the isodata results. Five class colours resulted. In this case, class 1 was red and OW. Class 2 was green, class 3 was blue, class 4 was yellow, and class 5 was teal. As per the percentages shown in Fig. 3.27 b), red made up 33% of the area, meaning that 33% of the pixels within the red box in Fig. 3.27 a) were OW. As a result, the remaining 67% of the pixels were considered ice, and hence IC was 67%. The four other non-OW classes provided undetermined characteristic differentiation of the ice. The U Bremen AMSR-2 IC image in Fig. 3.27 c) showed a similar IC pattern for the studied area. The uncertainty on SAR isodata results was set

as an assumed conservative value of 1.0 tenths, as per Section 2.9.2, due to the results obtained from the isodata unsupervised classification and the lower precision of those results.

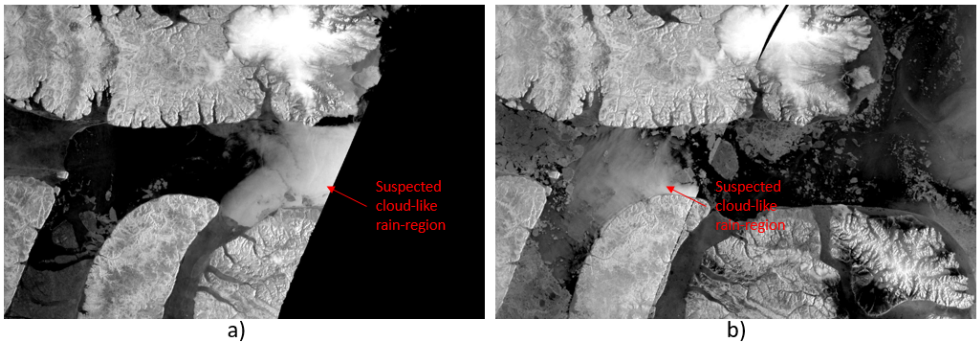

Figure 3.25: Sentinel-1 Extra Wide (EW) Swath HH polarized decibel γ^0 SAR image of a section of Lancaster Sound: a) Jun 7, 2016, and b) Jun 12, 2017 (images sourced from Copernicus [62])

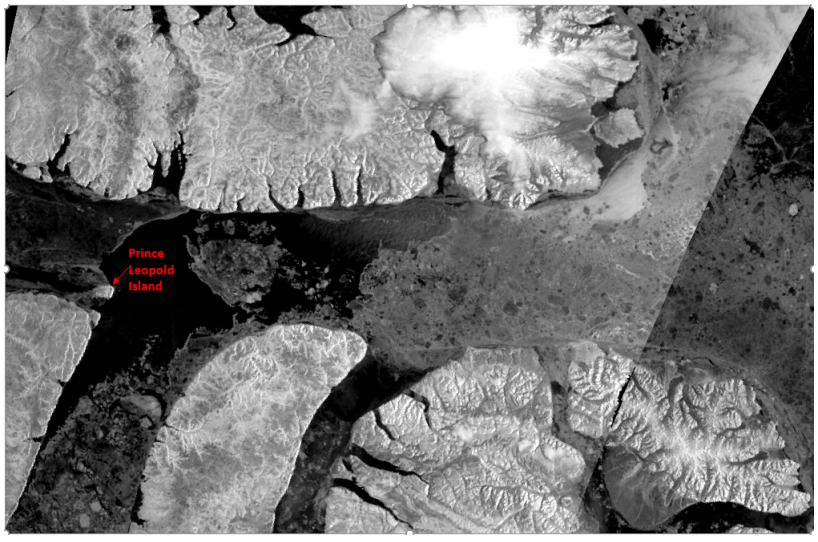

Figure 3.26: Sentinel-1 Extra Wide (EW) Swath HH polarized decibel γ^0 SAR image of a section of Lancaster Sound on May 22, 2017. Prince Leopold Island identified. EW spatial resolution is 20 m x 40 m. (image sourced from Copernicus [62]).

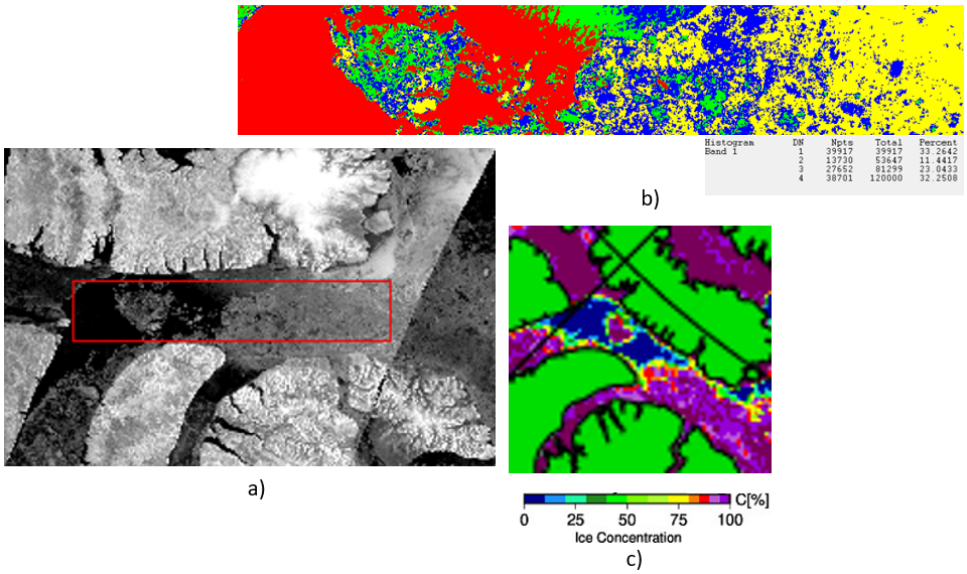

Figure 3.27: Isodata results for the Sentinel-1 SAR image on May 22, 2017 in Fig. 3.26: a) the red box is the selected non-land section in the SAR image of Lancaster Sound that was analyzed, b) isodata colour results for the red box area (red is class 1 and OW, and the other colours are ice), along with band colour percentages, and c) U Bremen AMSR-2 PM IC results (image sourced from [71]) for the same area.

3.4.2 RCM Results 2020-2024

After doing isodata unsupervised classification of RCM HH polarized SAR images of Lancaster Sound at various times of year between 2020-2024, it was determined that isodata classification was able to differentiate OW and ice during times of year when there was a good mix of both. It did not work when the Sound was practically ice covered, nor did it work when the Sound was fully OW. Similar to the Sentinel-1 isodata unsupervised classification in ENVI, the process generally produced consistent class colours, where red was OW, and sometimes green and blue was also OW. As with the AVHRR visible channel and Sentinel-1 isodata analysis, the settings were: number of classes set as min 3 to max 5, with 3 iterations, 3 min pixels per class, and a change threshold of 5%. Isodata worked acceptably on the following dates (just red as OW unless otherwise specified):

1. 2020: April 19, April 28, May 19 (red and green as OW), May 23 (red

and green as OW), Jun 2 (red, green and blue as OW), Oct 9 (red, green and blue as OW);
2. 2021: May 27, Oct 27;
3. 2022: May 25 (red and green as OW), Oct 4 (red, green and blue as OW), Oct 16 (red, green and blue as OW);
4. 2023: May 24 (red, green and blue as OW), Oct 21 (red, green and blue as OW), Nov 5; and
5. 2024: May 27, Jun 18, Nov 25.

Overall, the isodata method seemed to work near end of May and late October/early November, depending on IC, which was acceptable since this was near the melt and freeze seasons.

Fig. 3.28 shows the RCM SC100M HH polarized SAR image (100 m resolution) of Lancaster Sound on May 19, 2020. Fig. 3.28a) shows the image when opened using a standard image viewing software, and Fig. 3.28b) is the same image in ENVI, which appears brighter and shows more detail. Isodata results for the May 19, 2020 RCM SAR image from Fig. 3.28 are shown in Fig. 3.29. Fig. 3.29 a) is the SAR image with the red box showing the selected non-land section of Lancaster Sound that was analyzed. Fig. 3.29 b) shows the isodata colour results for the red box area. Five classes resulted, where class 1 was red and OW. Class 2 was green and also OW in this case. Class 3 was blue, class 4 was yellow, and class 5 was teal, and these three classes were ice. The ability to cross-reference with the U Bremen AMSR-2 IC image, Fig. 3.29 c), allowed for analyst determination of red and green as OW. As per Fig. 3.29 b), red and green made up 56% of the area in total, meaning that 56% of the pixels within the large red box in Fig. 3.29 a) were OW. As a result, the remaining 44% of the pixels were considered ice, hence an IC of 44%, with the three other classes (blue, yellow and teal) providing information that differentiates the ice based on undetermined characteristics. The U Bremen AMSR-2 IC image in Fig. 3.29 c) showed a similar pattern for the studied area. The uncertainty on SAR isodata results was set as an assumed conservative value of 1.0 tenths, as per Section 2.9.2, due to the results obtained from the isodata unsupervised classification and the lower precision of those results.

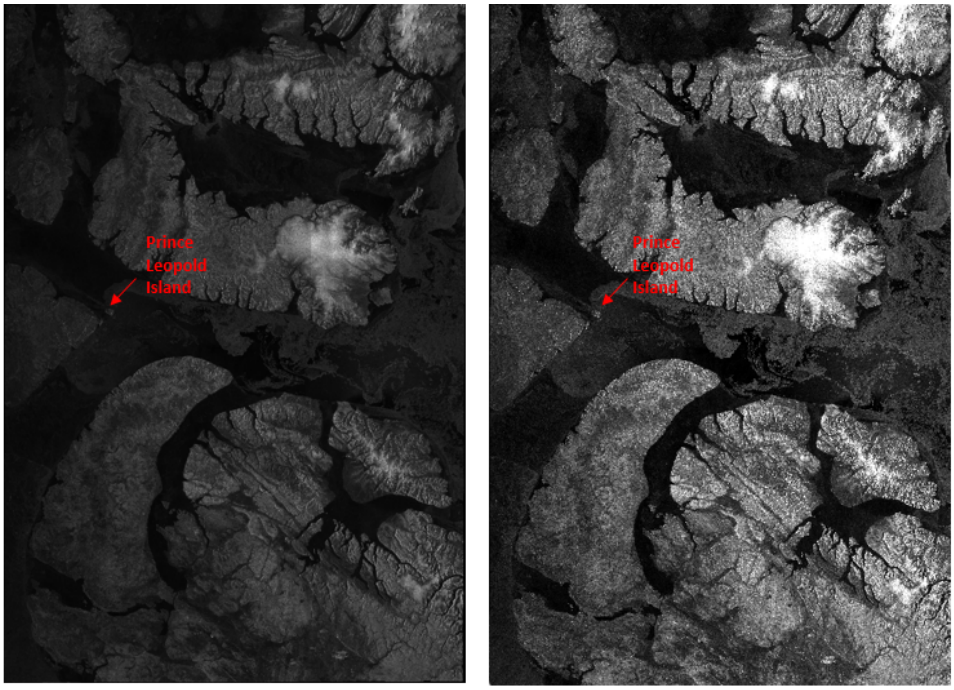

Figure 3.28: RADARSAT Constellation Mission (RCM) SC100M HH polarized SAR image (100 m spatial resolution) of a section of Lancaster Sound on May 19, 2020, at 22:50 GMT, with Prince Leopold Island identified (image sourced from EODMS [63]): a) image viewed in a standard image viewing software, and b) image viewed in ENVI, which appears brighter and shows more detail.

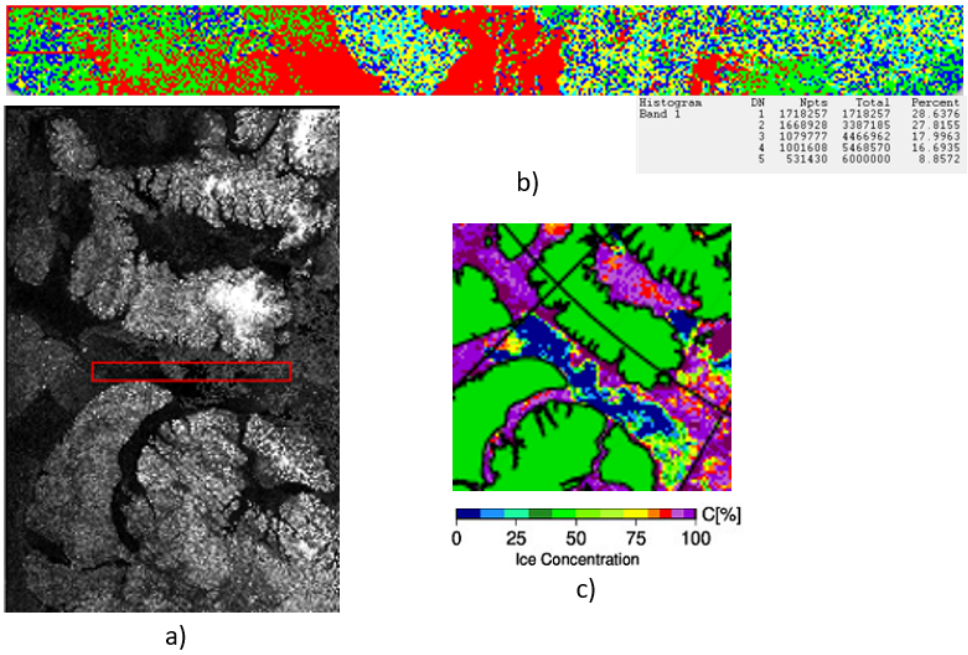

Figure 3.29: Isodata results for the RADARSAT Constellation Mission (RCM) SAR image on May 19, 2020 in Fig. 3.28: a) the red box is the selected non-land section in the SAR image of Lancaster Sound that was analyzed, b) isodata colour results for the red box area (red is class 1 and OW, green is class 2 and also OW in this case, and the other colours are ice), along with band colour percentages, and c) U Bremen AMSR-2 PM IC results (image sourced from [71]) for the same area.

3.5 ACIC Accuracy Assessment 2015-2024 Results

3.5.1 ACIC and SAR Near-Concurrent Images Comparison

Two near-concurrent comparisons of ACIC images with SAR isodata results were completed. The spatial resolution of the AVHRR images was 1.1 km at nadir, while the SAR images were the following: Sentinel EW at 20 m x 40 m resolution and RCM SCLN at 100 m resolution. The first comparison was for Apr 22, 2015 (calendar day 112), which compared a MetOp-A image at 23:46 GMT and a Sentinel-1 EW HH polarized image at 23:07 GMT, shown in Fig. 3.30. This specific timed Sentinel-1 image was different than the HH decibel γ^0 images used for ACIC analysis in the rest of the research for this

thesis, as the HH decibel γ^0 images tended to cover a wider section of Lancaster Sound. The HH decibel γ^0 images were composites for a whole day. The ACIC and SAR images, Fig. 3.30 a) and b), respectively, showed similar features and detail. These two images also showed more detail than the U Bremen AMSR-2 image in Fig. 3.30 c). Fig. 3.30 d) and e) are the isodata analysis of the red box in the SAR image. As per the other isodata analysis for this research, the isodata settings used were: number of classes set as min 3 to max 5, with 3 iterations, 3 min pixels per class, and a change threshold of 5%. Five classes resulted, where class 1 was red and OW. Class 2 was green, class 3 was blue, class 4 was yellow, and class 5 was teal. The four classes other than red were ice. In Fig. 3.30 e), the red OW region was 17%, meaning that the IC was 83% in that area. The red OW region in Fig. 3.30 e) also corresponded to the OW region in the ACIC image, Fig. 3.30 a), just east of the ice arch and south of Resolute.

The second near-concurrent comparison was for Apr 16, 2022 (calendar day 106), which compared a MetOp-B image at 22:21 GMT and and RCM ScanSAR Low Noise (SCLN) 100 m resolution HH polarized image at 22:59 GMT. The ACIC and SAR images, Fig. 3.31 a) and b), respectively, show similar features and detail. These two images also show more detail than the U Bremen AMSR-2 image in Fig. 3.31 c). Isodata analysis was attempted for Fig. 3.31 d) and Fig. 3.31 e), though in this case, Fig. 3.31 e) was an example of when the isodata results were inconclusive. Nonetheless, the characteristic shape of the ice arch in the ACIC and SAR images, Figs. 3.31 a) and b) respectively, was very similar and identifiable.

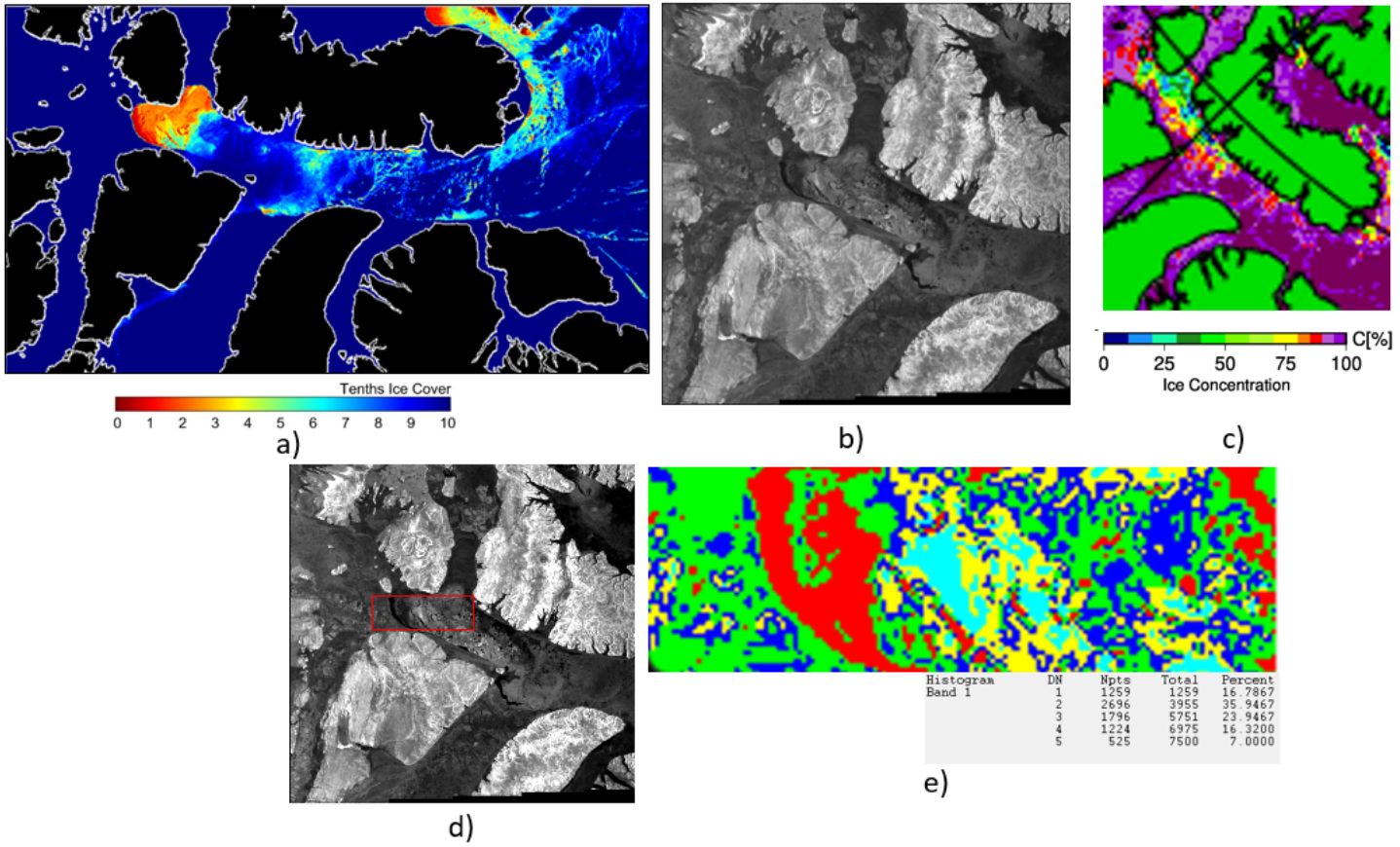

Figure 3.30: Near-concurrent comparison on Apr 22, 2015 of a Sentinel-1 EW HH polarized SAR image of a section of Lancaster Sound at 23:07 GMT with a MetOp-A AVHRR image at 23:46 GMT with ACIC applied: a) ACIC and land mask applied, b) Sentinel-1 EW HH polarized SAR image, c) U Bremen AMSR-2 IC map from the same day (image sourced from [71]), d) SAR image from b) with red box identifying analyzed isodata area, e) isodata results for the SAR image, where red is class 1 and OW.

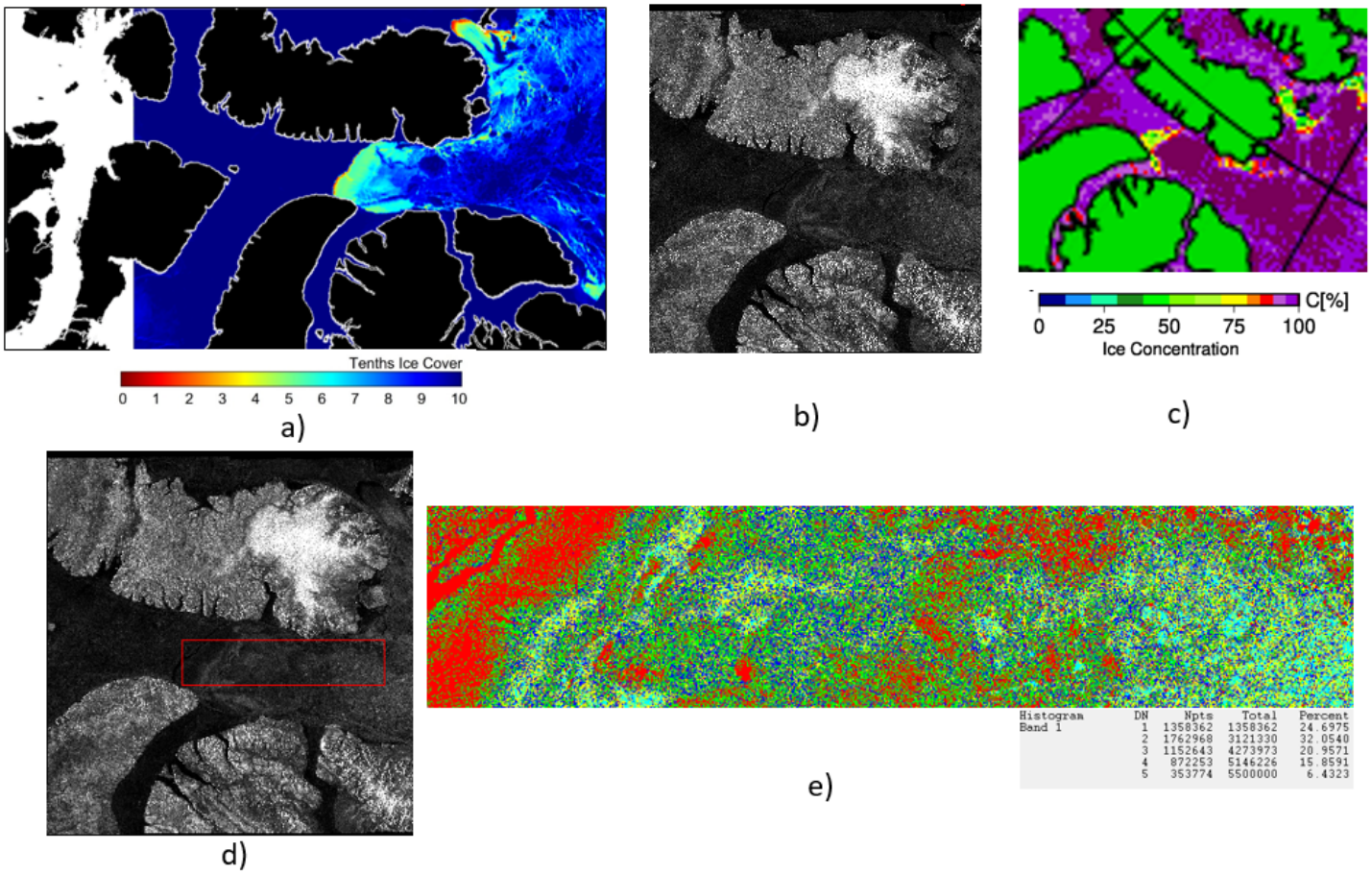

Figure 3.31: Near-concurrent comparison on Apr 16, 2022 of a RADARSAT Constellation Mission (RCM) SCLN (ScanSAR Low Noise 100 m resolution) HH polarized SAR image of a section of Lancaster Sound at 22:59 GMT with a MetOp-B AVHRR image at 22:21 GMT, with ACIC applied: a) ACIC and land mask applied, b) RCM SCLN HH polarized SAR image, c) U Bremen AMSR-2 IC map from the same day (image sourced from [71]), d) SAR image from b) with red box identifying analyzed isodata area, e) isodata results for the SAR image, though in this case those results are inconclusive.

3.5.2 ACIC, CIS Ice Charts, U Bremen AMSR-2 IC Comparison

To determine how accurately the ACIC algorithm measured IC over the 10-year span in Lancaster Sound, a graph was created to compare the ACIC results with the CIS ice charts and the U Bremen AMSR-2 PM results, as shown in Fig. 3.32. IC values sourced from the CIS ice charts and U Bremen AMSR-2 IC maps were interpreted from visually analyzing those charts/maps by the author of this thesis. For these ACIC results, any SAR and AVHRR visible channel gap-filling data was removed, which sometimes required re-averaging of certain data points. In addition, the comparison was only done for the periods of the year when the ACIC was determined to work accurately, which was when SST $<$ -1.8° C and also corresponded to a snow/ice pack $b9$ temperature of approximately $<$ -3° C.

Uncertainties for ACIC data was as per Eqn. 2.9. CIS ice chart data uncertainty was as per Eqn 2.10, and U Bremen AMSR-2 data uncertainty was as per Eqn 2.11. Where the CIS ice chart IC value was shown as 9.5, that was an interpretation of the 9+ values given by the CIS ice charts, which were assigned a value of 9.5 for the research for this thesis. In contrast, for ACIC results during the coldest parts of the year, either a 9 or 10 for IC was assigned during the yearly analysis, as it was too difficult to accurately assign a 9.5 vice a 9 or 10 based on the colour spectrum. Day 365 was not present in all years, so its data was not shown.

In January-May in Fig. 3.32, ACIC and U Bremen AMSR-2 IC data followed similar trajectories, with the data converging at approximately day 134 (May 14). However, the error bars did overlap for this entire period. The CIS ice charts reported a 9.5/10 IC much later into the spring, up to day 120 (Apr 30) than both of the other data sources. Up to day 113 (Apr 23), ACIC data reported IC values approximately 1/10 lower than the U Bremen results, and up to approximately 2/10 lower than the CIS ice chart data by day 127 (May 7). ACIC results are based on AVHRR images with approximately 1.1 km resolution, so smaller areas of ice floes would likely be shown in better detail than the 6.25 km resolution U Bremen images. In the fall time period, ACIC values were still the lowest values of the three methods.

Over the whole 10-year average, shown in Fig. 3.32, ACIC results reported lower IC values than CIS ice chart IC results by approximately 0.6-2.9 tenths, depending on the time of year, and lower IC values than U Bremen AMSR-2 IC results by approximately 0.0-1.6 tenths, depending on the time of year. However, all three data method results were nearly in full agreement when error bars were taken into account: ACIC results matched 34/34 (100%) of

the weekly data points with the U Bremen AMSR-2 IC results, and ACIC results matched 30/34 (88%) of the weekly data points with the CIS ice chart IC results. These exceptions were days 92 (Apr 2), 106 (Apr 16), 120 (Apr 30), and 127 (May 7).

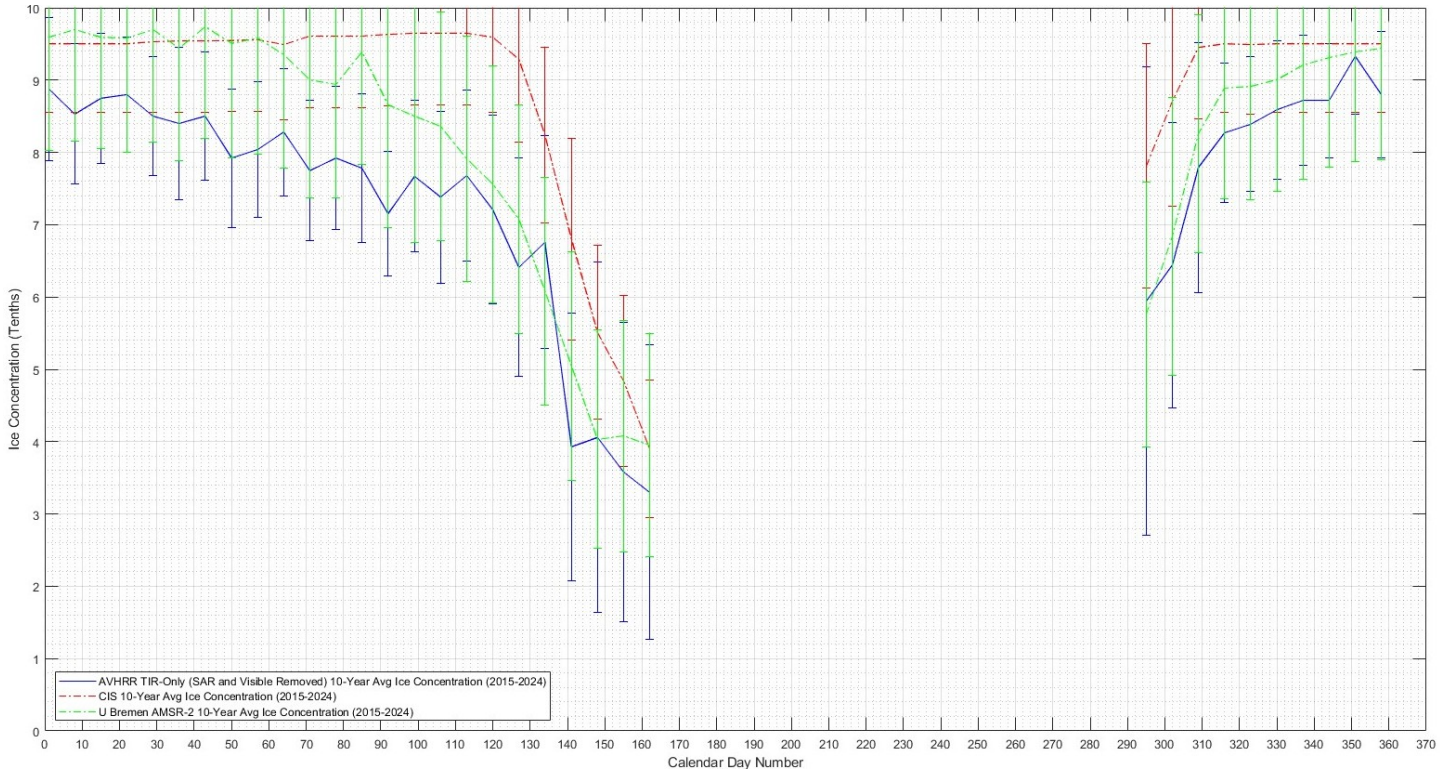

Figure 3.32: 10-year average (2015-2024) IC results for Lancaster Sound using ACIC only (SAR and AVHRR visible channel data removed), compared with CIS ice charts and U Bremen AMSR-2 PM IC maps for times of year that ACIC worked. ACIC worked when SST < -1.8° C. Day 365 was not present in all years, so its data was not shown. ACIC results matched 34/34 (100%) of the weekly data points with the U Bremen AMSR-2 IC results, and ACIC results matched 30/34 (88%) of the weekly data points with the CIS ice chart IC results (exceptions were days 92, 106, 120 and 127).

3.6 Ice Condition Changes in Lancaster Sound 2015-2024

3.6.1 Sea Ice Melt and Freeze Dates

For this research, the definition of *melt* date was selected as the point where the majority (over 50 %) of Lancaster Sound had a sea IC below the lower limit, 4/10, of the 4-6/10 open drift range, based on the ACIC results. Consequently, *freeze* date was when IC then raised above 6/10, the upper limit of the open drift range. Table 3.3 shows the melt/freeze dates per year. The average melt date over the time span was calendar day 153 (Jun 2), with a standard deviation of 21 days. The average freeze day was calendar day 293 (Oct 20), with a tighter standard deviation of nine days. Some SAR or AVHRR visible channel data aided in the determination of the ACIC melt days. Use of the melt and freeze date results provided input towards recommendations in Chapter 4 for times of year to deploy hydrophones and sonobuoys in the waters of Lancaster Sound to support the Audimus cubesat mission. Calculation of these melt and freeze dates were slightly different than the dates that the ACIC line passes the 4/10 and 6/10 IC thresholds on Fig. 3.13. This is because the yearly melt dates were determined from examination of the ACIC and CASSTA results for the entire Lancaster Sound at once on a specific day for each year.

Table 3.4 is similar to Table 3.3, but instead it shows melt and freeze dates based on U Bremen AMSR-2 IC maps. The average melt day over the 2015-2024 time span was calendar day 160 (Jun 9), with a standard deviation of 24 days. The average freeze day was calendar day 292 (Oct 19) with a much tighter standard deviation of nine days. In comparing Tables 3.3 and 3.4, the ACIC predicted a 10-year average melt day seven days earlier than the U Bremen data, and a freeze date one day later than the U Bremen data.

Table 3.3: Determination of melt and freeze dates* in Lancaster Sound, 2015-2024, using ACIC results

Year	Melt Month & Day	Melt Calendar Day #	Freeze Month & Day	Freeze Calendar Day #	Duration Between, in Days
2015	May 11	131	Oct 20	293	162
2016	May 8	129	Oct 9	283	154
2017	May 29	149	Oct 10	283	134
2018	Jul 2	183	Oct 7	280	97
2019	Jun 24	175	Oct 27	300	125
2020	May 19	140	Oct 24	298	158
2021	May 25	145	Nov 3	307	162
2022	Jul 12	193	Oct 16	289	96
2023	May 8	128	Oct 21	294	166
2024	Jun 1	153	Nov 2	307	154
Avg	Jun 2	153	Oct 20	293	141
Std Dev	N/A	22	N/A	9	25

*Melt date defined as the majority of Lancaster Sound ($> 50\%$) reaching a 4/10 threshold IC, and freeze date defined as majority of Lancaster Sound reaching a 6/10 threshold IC.

Table 3.4: Determination of melt and freeze dates* in Lancaster Sound, 2015-2024, using University of Bremen ASMR-2 IC maps

Year	Melt Month & Day	Melt Calendar Day #	Freeze Month & Day	Freeze Calendar Day #	Duration Between, in Days
2015	May 23	143	Oct 17	290	147
2016	May 12	133	Oct 7	281	148
2017	May 31	151	Oct 8	281	130
2018	Jul 10	191	Oct 10	283	92
2019	Jun 26	177	Oct 15	288	111
2020	May 24	145	Oct 22	296	151
2021	Jun 11	162	Nov 4	308	146
2022	Jul 14	195	Oct 15	288	93
2023	May 24	144	Oct 26	299	155
2024	Jun 10	162	Nov 1	306	144
Avg	Jun 9	160	Oct 19	292	132
Std Dev	N/A	24	N/A	9	23

*Melt date defined as the majority of Lancaster Sound (> 50%) reaching a 4/10 threshold IC, and freeze date defined as majority of Lancaster Sound reaching a 6/10 threshold IC.

3.6.2 Ice Arch Location

The location of the ice arch varied over the 2015-2024 timeframe, as shown in Table 3.5. The east-west location of the arch in a certain year affected the IC dynamics in Lancaster Sound for that specific year. Bylot Island, used as the eastern marker [24], is the small island at the east end of Lancaster Sound, directly south of the eastern edge of Devon Island.

Table 3.5: Location of the ice arch within Lancaster Sound on a yearly basis, 2015-2024, based on AVHRR images

Year	Ice Arch Location	km West from Bylot Is.*
2015	Resolute	450
2016	Prince Leopold Is.	310
2017	Prince Leopold Is.	290
2018	Arctic Bay longitude	120
2019	slightly west of Arctic Bay longitude	200
2020	Prince Leopold Is.	300
2021	west of Resolute	550
2022	Arctic Bay longitude	150
2023	Prince Leopold Is.	approx. 290
2024	middle between Resolute & Prince Leopold Is.	approx. 370

*Data from [24], except 2023 and 2024. Bylot Is. is the eastern edge of Lancaster Sound.

For 2023 and 2024, ice arch formation dates were determined to be day 37 (Feb 6) and 118 (Apr 27), respectively. For 2023, non-cloudy AVHRR images were available for calendar days 34, 37 and 38 using MetOp-B. On day 34, the arch had not yet formed but had formed by day 37. The year 2024 was an anomalous year, because an ice arch first formed on day 23 (Jan 23) west of Resolute, but then ice slowly filled and compacted east of it, until a new ice arch formed on day 118 (Apr 27) at a location between Resolute and Prince Leopold Island. In 2024, non-cloudy AVHRR MetOp-B or MetOp-C images were available for days 22, 23, and 24. On day 22 the first ice arch had not yet formed, but was formed by day 23. In 2024, non-cloudy AVHRR MetOp-B images were available for days 112, 118 and 129. On day 112 the final ice arch had not yet formed, but was formed by day 118. Based on the criteria of ice arch formation occurring when it achieved the characteristic shape for the season [24], day 118 was selected as the 2024 ice arch formation date.

For 2023 and 2024, ice arch collapse dates were determined to be calendar days 192 for 2023 (Jul 11), and 191 for 2024 (Jul 9). For 2023, non-cloudy AVHRR images were obtained for calendar days 191 and 193. On day 191 the ice arch was intact, but on 193 it was not. For 2024, non-cloudy AVHRR images were available for both days 190 and 191, where the ice arch was intact on day 190, but it had a big crack on day 191. The dates were determined based on the criteria of ice arch collapse being characterized by the breakdown of the structure [24].

Table 3.6 was created to determine if there was any trend between the estimated spring melt date, denoted by the majority IC first reducing in a particular year to below 4/10 IC range, and the Lancaster Sound ice arch collapse date. From the results, there appeared to be no direct relation.

Table 3.6: Ice arch formation and collapse in Lancaster Sound, 2015-2024. Melt dates based on ACIC data, and melt considered achieved when the majority of the IC within Lancaster Sound drops below 4/10

Year	Ice Arch Formation Calendar Day #*	Melt Calendar Day #	Difference Between Melt/Arch Formation	Ice Arch Collapse Calendar Day #*	Difference Between Melt/Arch Collapse**
2015	1	131	130	180	49
2016	60	129	69	185	56
2017	70	149	79	160	11
2018	105	183	78	172	-11
2019	35	175	40	170	-5
2020	62	140	78	175	35
2021	60	145	85	195	50
2022	50	193	143	180	-13
2023	37***	128	91	192***	64
2024	118***	153	35	191***	38
Avg	60	153	83	180	27
Std Dev	32	22	32	12	28

*Values for 2015-2022 approximated from [24]

**If negative, ice arch collapses first.

***2023-2024 ice arch formation/collapse dates determined during research for this thesis.

3.6.3 Summary of Ice Arch, Melt/Freeze and Full OW Dates

A summary table of important dates including 10-year average for ice arch formation/collapse, melt/freeze dates, and full OW date ranges is presented in Table 3.7.

Table 3.7: 10-year average dates for ice arch formation/collapse, melt/freeze, and full OW range in Lancaster Sound, 2015-2024

Category	Avg Ice Arch Formation Calendar Day #	Avg Melt* Calendar Day #	Avg Ice Arch Collapse Calendar Day #	Avg Freeze* Calendar Day #	Avg Full OW Date Range (Calendar Days)
Avg Date	60 Mar 1	153 Jun 2	180 Jun 29	293 Oct 20	207-270 Jul 26 - Sep 27
Std Dev	32	21	12	9	14 and 26
Date Ranges	Jan 28 - Apr 2	May 12 - Jun 23	Jun 17 - Jul 11	Oct 11 - Oct 29	Jul 12 - Oct 23

*Melt date defined as the majority of Lancaster Sound (> 50%) reaching a 4/10 threshold IC, and freeze date defined as the majority of Lancaster Sound reaching a 6/10 threshold IC.

4 Discussion

4.1 ACIC Limits and Yearly Results Analysis 2015-2024

This section discusses the results presented in Sections 3.1 and 3.2.

4.1.1 MetOp-A/B/C Satellite Applicability

The CASSTA [29] SST algorithm was originally designed for MetOp-A satellite data. MetOp-A ceased operations by December 2021, so the algorithm had to be tested with MetOp-B and MetOp-C to determine its accuracy and applicability. This was completed using the Change Detection tool in ENVI and three different days using all three satellites. The results of two of those days, Feb 13, 2020 and Mar 6, 2020 were presented in Figs. 3.1 and 3.2. The percentage difference results, shown in Fig. 3.1 were less than 2.4%, and less than 0.9% in Fig. 3.2. The results also tested Lancaster Sound near the edge of the image swath for the MetOp-A and -C images. Therefore, MetOp-B and MetOp-C images were applicable for use in 2021-2024 for the ACIC analysis in this research. The maximum sensor zenith angle for these images at the edge of the AVHRR swath was approximately 52°, which provided a test of a non-ideal case. Even though this was greater than the maximum 45° for the CASSTA algorithm [29], the minimal percent change between MetOp-A, -B, and -C images, even at different sensor zenith angles, showed that different images slightly off nadir could still be used for all three satellites. For the main image analysis for the 10-year period, images were selected to comply with the $< 45°$ sensor zenith angle recommendation, though sensor zenith angle values were not recorded. At the 11 µm wavelength used in AVHRR channel 4 (TIR) for sensor zenith angles $< 45°$, the emissivities of snow and bare ice are approximately within less than 0.01 of each other [29], thus minimizing the impact on IC values.

4.1.2 Time of Year Limits and Daylight Effects

Based on the weekly ACIC and CASSTA images of Lancaster Sound generated in ENVI during the 2015-2024 timeframe, it was determined that at certain times of year, the SST was too warm for the ACIC to be accurate. Through analysis of images in late May and early June, the determining factor was that the snow/ice pack value for the spatial pixel editor, the $b9$ value from Eqn. 2.7, became > -3° C on the CASSTA image, corresponding with the CASSTA image having SST > -1.8° C, as shown in Fig. 3.15. Further details on the SST limit are provided in the related Technical Note [51] in Appendix A. It was straightforward to detect when the ACIC no longer worked, as the IC image did not look accurate, and cross-referencing with the geo-referenced TIR image would show discrepancies in ice and water identification, as per Fig. 3.15. In addition, melt ponds at that time of year on top of the ice may have also skewed the thermal results.

Table 3.2 and Fig. 3.16 shows the annual time of year limits, from 2015-2024, when the ACIC stopped working in the spring, and when it started working again in the fall. It was determined that, based on the 2015-2024 data, the ACIC works for approximately 7+ months per year, from January-early June and late October-December, and some years it still worked in late September. For the 10-year average, ACIC stopped working on day 161 (Jun 10) with a standard deviation of 5 days. ACIC began to work again, once the SST dropped below -1.8° C, on day 298 (Oct 25) with a standard deviation of 10 days. This is considered very useful, as it covers the majority of the time where ice was present in Lancaster Sound, and, as also shown in Fig. 3.16, large portions of July-September are times of year where Lancaster Sound was fully OW. One drawback, however, is that for all of the ten years studied, the ACIC stopped working in the spring before the ice arch fully collapsed. This amount of time ranged from less than 5 days prior to ice arch collapse in 2017, to a maximum of 35 days prior in 2021, as per Fig. 3.16. However this was deemed acceptable as the dates were close, and there was enough sunlight that time of year to also use AVHRR visible channel analysis if required.

The time of day of the images used for this research were either between 0:00-03:00 GMT (18:00-21:00 local or 19:00-22:00 local the previous day, depending on west or east end of the Sound) or 22:00-24:00 GMT (16:00-18:00 local or 17:00-19:00 local depending on west or east end of the Sound). Based on these time periods, as well as the geographical location of Lancaster Sound, some daylight was present starting in April, with daylight all day by the end of April. Daylight then faded by late September. This means that for the AVHRR images analyzed in this research, ambient light in varying intensities

was present from early April-late September. During this period, the ACIC still worked between April-late May/early June, with May and June having alot of ambient light at all times of the day. CASSTA is designed for OW, sea ice and MIZ conditions in the arctic [29], but the presence of melt ponds in April-June could have had an effect on emissivity values of the the sea ice, raising emissivity values and resulting in apparent lower IC values. Continuous daylight in May/June could also have led to solar heating/insolation, which could cause discrepancies in the temperature in the top few mm of ice and sea water vs the bulk temperature [27] and hence result in lower IC values.

4.1.3 ACIC (Gap-filled) Yearly Results vs CIS Ice Charts

Yearly graphs of IC between 2015-2024 were generated for Lancaster Sound and Barrow Strait, from Resolute in the west to the eastern edge of Devon Island in the east. Each graph compared the ACIC results, gap-filled by SAR and AVHRR visible channel analysis, with CIS ice charts IC data. The analyzed weekly ACIC figures showing IC colour mapping are presented by year in Appendix B. The data points on Figures 3.3 to 3.12 are aligned with the CIS ice chart dates, so the corresponding images in Appendix B may be $\pm$ 2 days from those dates. The years 2019 and 2021 were the best matches of the ACIC results, gap-filled with SAR and AVHRR visible channel, with the CIS ice chart data including error bars. The other years showed more variability, mostly at the beginning of the year, where ACIC results showed lower IC than the CIS ice charts' data.

The following are comments by year between ACIC (gap-filled by SAR and AVHRR visible channel) and CIS ice chart IC results:

1. 2015 (Fig. 3.3) - The main difference where the ACIC and CIS ice chart IC data did not overlap, even including error bars, was day 82-138 (Mar 23 - May 18). This is within the window where sunlight starts occurring in April, and melt season begins near the end of that period, with the melt date for 2015 occurring on May 11 as per Table 3.3. Perhaps the presence of melt ponds in April/May could have had an effect on emissivity values of the the sea ice, raising emissivity values and resulting in apparent lower IC values. Continuous daylight in May could also have led to solar heating and also apparent lower IC values. In the summer period, AVHRR visible channel results on days 180 and 187 (Jun 29 and Jul 6) showed OW while the CIS ice chart reported an IC of almost 1.3/10. It is not known why this was the case for the CIS ice charts. For the significant difference period between days 280-292 (Oct 7-19),

the two Sentinel-1 SAR images visually showed OW while the CIS ice chart IC was already showing 5.5/10 and 9/10 IC.

2. 2016 (Fig. 3.4) - For the significant lower ACIC from day 1-25 (Jan 1-25) than the CIS ice charts IC, the main reason is likely due to some fine cloud mist over certain sections of the Sound, after re-examination of the related geo-referenced ACIC images for those days, which would result in lower than actual IC, as not all of the emitted energy would reach the AVHRR instrument in orbit. There was no ice fog for those days, however. In April/May/June, some of the melt pond and solar heating/insolation IC-lowering effects may have been present. The melt date in 2016 was May 8 as per Table 3.3. In the late summer, the SAR result on 256 (Sep 12) showed OW while the CIS ice charts reported an IC of 2.5/10. It is not known why this was the case for the CIS ice charts.
3. 2017 (Fig. 3.5) - ACIC values dipped lower than the CIS ice charts IC results between days 72-135 (Mar 13 - May 15) including error bars. This was different than 2015 and 2016 as the dip in ACIC values began in mid-March. During the second half of March, after re-examination of the related geo-referenced ACIC images for those days, there was some minimal mist in some sections of the Sound. There was no ice fog for those days, however. In April/May, melt ponds and solar heating/insolation may have had an effect in lowering the ACIC values. The melt date in 2017 was May 29 as per Table 3.3.
4. 2018 (Fig. 3.6) - Similar to 2017, there was a significant period of lower ACIC values compared to CIS ice chart values in March, including error bars. This period also extended from day 50-99 (Feb 19 - Apr 9). As per 2017, after re-examination of the related geo-referenced ACIC images for those days, on some days there was some minimal mist in some sections of the Sound, though no ice fog. Fig. 4.1 shows the ACIC geo-referenced images for three days in March. There was also a greater difference between the ACIC results and the CIS results in April/May, possibly due to melt ponds and solar heating/insolation effects. The melt date in 2018 was May 31 as per Table 3.3. The year 2018 showed the highest IC values over the summer period, as reported by both ACIC and CIS data, though the reason for the presence of high IC in Lancaster Sound was undetermined from the gathered data. In the fall, the ACIC was lower from day 240-310 (Aug 28 - Nov 6). Review of the SAR image on day 267 (Sep 24) showed mostly OW, though Resolute was not present in the image.
5. 2019 (Fig. 3.7) - The ACIC values and CIS ice chart values matched

well with error bars included, though the ACIC values were still lower. There was one anomalous low ACIC data point on day 133 (May 13). No identifiable reasons from re-examining the AVHRR geo-referenced TIR image on May 13 were determined.

6. 2020 (Fig. 3.9) - The year 2020 was very cloudy, requiring significant gap-filling with SAR and AVHRR visible channel. The period between days 97-138 (Apr 6 - May 17) where the ACIC values were much lower than the CIS ice chart data may have been due to melt ponds or solar heating/insolation effects. The melt date in 2020 was May 24 as per Table 3.3. The early fall lower ACIC value period between days 250-300 (Sep 6 - Oct 26) was interesting, because AVHRR visible channel images for early September showed OW while the CIS ice charts record IC values of greater than 2/10.
7. 2021 (Fig. 3.9) - The year 2021 was also one of the best matches of ACIC values with CIS ice chart values, including error bars. The main discrepancy was in the summer between days 192-256 (Jul 11 - Sep 13), where the CIS data reported IC up to 2.8/10 while AVHRR visible channel reported mostly OW in that timeframe.
8. 2022 (Fig. 3.10) - The ACIC values were lower than the CIS ice chart values, error bars included, for days 52-108 (Feb 21 - Apr 18). Some minimal mist was present on a few of the related ACIC images, but less frequent than previously mentioned years. In the April part of this period, solar heating/insolation might have started to become a factor, which would lower IC values, but melt ponds were less likely as the melt date for 2022 was Jul 14 as per Table 3.3. In the fall, there was a lower ACIC period of day 290-311 (Oct 17 - Nov 7). The first data point of that period was a RCM SAR image which was difficult to interpret IC well, though the corresponding U Bremen AMSR-2 image showed the majority of the Sound as OW.
9. 2023 (Fig. 3.11) - The year 2023 followed a pattern very similar to 2022. There was a period of lower ACIC from day 51-149 (Feb 20 - May 29). Any potential mist effects in this period were on par with 2022 and less than previously mentioned years. Melt ponds and solar heating/insolation may have had an effect in April/May. The melt date in 2023 was May 24 as per Table 3.3.
10. 2024 (Fig. 3.12) - There was significant variability in ACIC between day 1-141 (Jan 1 - May 20), though the error bars overlapped the majority of the time with the CIS ice chart values. The biggest discrepancy occurred on day 141 (May 20). On this day there was some mist shrouding the Sound west of Prince Leopold Island. The melt date in 2024 was Jun 10

as per Table 3.3. In the summer, there was a small period between days 204-225 (Jul 22 - Aug 12) where the CIS ice chart data reported IC up to 2/10, while the AVHRR visible channel showed OW. It is not known why this was the case for the CIS ice charts.

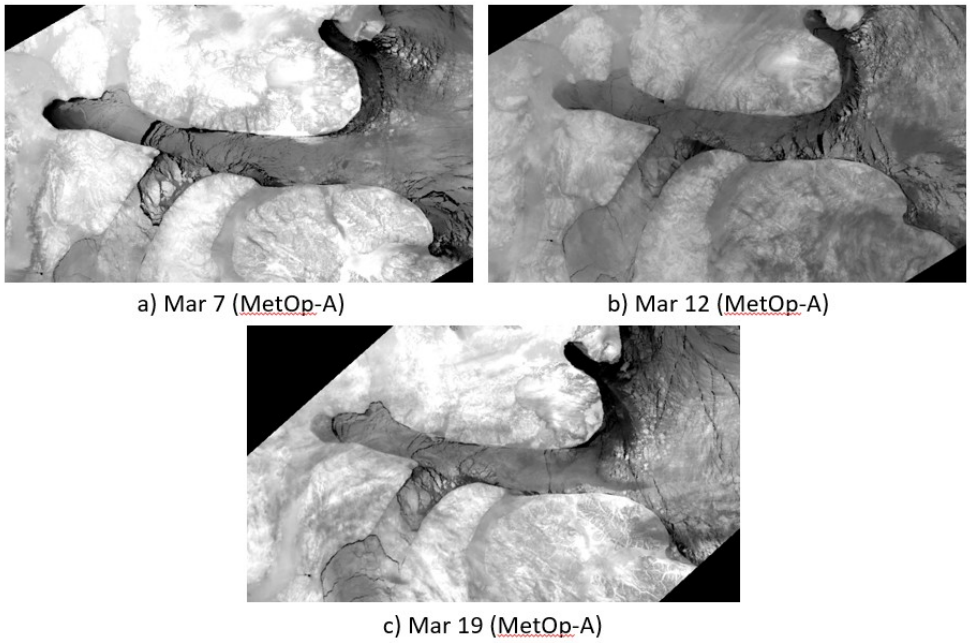

Figure 4.1: March 2018 AVHRR TIR geo-referenced images of Lancaster Sound. All three images were taken between 22:26-23:36 GMT. Some semi-transparent mist was present in parts of Lancaster Sound, which could have affected IC results.

For the 10-year average graph, Fig. 3.13, there was a lower ACIC period from day 1-142 (Jan 1 - May 22). Within this period, excluding error bars, the difference ranges from 0.6-2.8/10 lower than the CIS ice charts. However, with error bars included, the data in that period is in agreement except for day 92 (Apr 2) and day 127 (May 7). These two dates are within the time of year where melt ponds and solar heating/insolation could occur. In addition, as per the ACIC error analysis in the Technical Note [76] in Appendix A, the ACIC becomes less accurate as the SST rises. In the fall, there was a shorter reduced ACIC region from day 302-344 (Oct 29 - Dec 10). During the parts of the year where the CIS ice chart value was 9.5 on Figs. 3.3- 3.13, that was an interpretation of the 9+ values given by the CIS ice charts, which were

assigned a value of 9.5 for the research for this thesis. For the ACIC results during the coldest parts of the year, either a 9 or 10 for IC was assigned, as it was too difficult to accurately assign a 9.5 vice a 9 or 10 based on the colour spectrum used.

Potential reasons for the lower ACIC values from day 1-142 (Jan 1 - May 22) for the 10-year average in Fig. 3.13 include: granularity of the colour spectrums in the 9/10 to 10/10 between the ACIC and the CIS ice charts; the much smaller focused region of Lancaster Sound than the CIS ice charts' entire Eastern Arctic focus, shown in Fig 2.2, could have allowed for better spatial granularity on IC readings in Lancaster Sound and thus better observed detail; creating a weekly Lancaster Sound ACIC data point based on an average of four specific locations within the Sound might have been less precise than the CIS ice chart methods, which could lower the ACIC results accuracy; and the significant differences in 2017 and 2018 in both the calendar day 72-99 range (Mar 12 - Apr 8) and 2020 in the calendar day range 97-138 (Apr 6 - May 17) reduced the overall 10-year ACIC average results. For 2017, the ice arch formed on day 70 (Mar 11) which is near the March/April 2017/2018 time period of lower IC values, but in 2018 the ice arch formed on day 105 (Apr 15), which is just outside that time period. However, in 2017 the ice arch formed at Prince Leopold Island, so the lower IC at that location, which was one of the four locations where the IC was recorded, could have brought down the overall Lancaster Sound IC average between days 72-135 (Mar 13 - May 15).

A comparison of March 2017/2018 and March 2019/2021 was conducted to see what differences there were, as 2019 and 2021 had IC values which were closest to the CIS values in March. For March 2021, the spatial pixel temperatures used on the nearby ice packs ranged between -32 to -26° C. In March 2017, the spatial pixel temperatures used on the nearby ice packs also ranged between -32 to -26° C. For March 2019, the spatial pixel temperatures used on the nearby ice packs ranged between -23 to -19° C. In March 2018, the spatial pixel temperatures used on the nearby ice packs ranged between -35 to -31° C. So, it does not appear that the temperature of the ice pack that goes into the ACIC had an appreciable effect on IC results as all these ranges were similar. In 2021, the ice arch formed west of Resolute, and had not yet formed in March. In 2019, the ice arch formed slightly west of the point north of Arctic Bay. For 2017 and 2018, the ice arch formed at Prince Leopold Island and north of Arctic Bay, respectively, which are points more east than Resolute. In comparing the images of March 2018, Fig. B.7 j)-m), and March 2021, Fig. B.13 f)-j), the ice characteristics were similar, in that the solid ice pack occurred west of Resolute at that time. The estimated

difference is that some of the March 2018 images still perhaps had a faint cloud layer over parts of Lancaster Sound which was semi-transparent, as per Fig. 4.1. If so, a faint cloud layer resulted in a slightly lower IC value than should occur, as it would reduce the TIR emitted readings detected by the satellite. The same phenomena appeared to be present in March 2017. Another example is Jan 25, 2021 in Fig. B.13 b) in Appendix B, where clouds at the eastern entrance to Lancaster Sound have created an anomalous bright low IC pattern. In other cases, opaque cloud over a part of Lancaster Sound resulted in a dark blue colour, which generated a much higher IC than it should in that area. Examples include the east entrance to Lancaster Sound on Nov 13 and 24, 2021 (Fig. B.14 c) and d)) and May 8, 2023 (Fig. B.17 r)). Apr 8, 2024 (Fig. B.19 m)) was one anomaly, in an area southwest of the Sound, where opaque cloud resulted in brighter colours instead. In all cases during analysis, no data was used for a region of Lancaster Sound for that specific day if it was fully or mostly cloud-covered.

In 2020, day 104 (Apr 13) for example, had the ice arch established near Prince Leopold Island with lower IC east of it for the rest of the Sound, even though the CIS ice chart for that week still reported 9+/10 IC. From observing the graph in Fig. 3.8, the April/May ACIC values were much lower than the CIS ice chart results. However, observing the TIR images in April/May 2020 in Fig. 4.2 clearly showed an ice arch and some OW areas east of it, suggesting that the IC was much less than 9+/10.

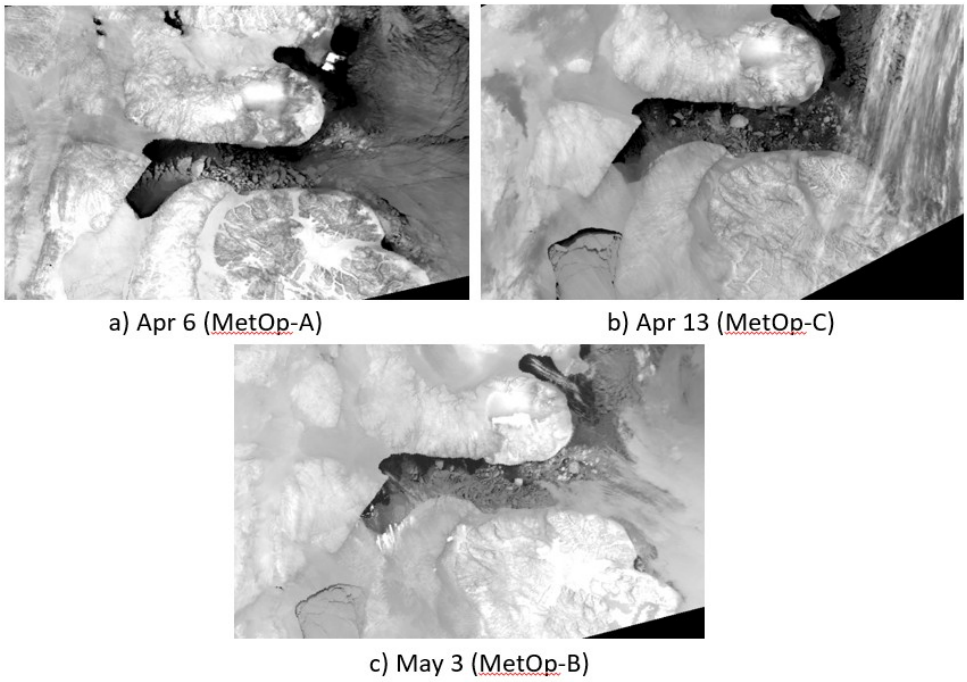

Figure 4.2: April and May 2020 AVHRR TIR geo-referenced images of Lancaster Sound: a) and b) were taken between 23:30-24:00 GMT, and c) was taken at 1:18 GMT. These images clearly show presence of an ice arch, while the CIS ice charts reported IC of 9+/10 on these dates.

Overall, for the 10-year average, the ACIC results were consistently just below the CIS ice charts results, as seen in Fig. 3.13, but the error bars either touched or overlapped, except for days 92 (Apr 2) and 127 (May 7), and the trend patterns were similar. The CIS ice charts, however, tend to be made more conservatively [22], which might explain the extended period of 9+ values in the CIS charts up to calendar day 120 (Apr 30) over a 10-year average. The selected CIS ice charts were generated for the entire Eastern Arctic region, which is a much larger area than Lancaster Sound, and these charts were created using various data sources such as SAR imagery in linear polarization, weather and oceanographic information, and visual observations from ships and aircraft [60, 65]. For the ACIC images at many times in January-May it was observed, by looking at the TIR images from channel 4, that the IC did not appear to be 9+/10 in some locations, as seen for example in Fig. 4.1. In addition, some SAR images used for gap-filling also

sometimes showed lower IC values than what the CIS ice chart reported. Additional weekly ACIC colour mapped images, for times of year when ACIC worked, are provided in Appendix B for 2015-2024. It is postulated that the ACIC is acceptably accurate within the uncertainty range for the Lancaster Sound-sized region and provides more IC granularity than the CIS ice charts, especially during the seasons where the CIS ice charts report consistent 9+/10 IC for lengthy periods before their data typically reports a rapid decrease in late May.

For the four locations graph in Fig. 3.14, over the 10-year span, Resolute at the westmost entrance retained the highest IC later into spring, which was expected. For example, the average IC was still within the open drift category of 4-6/10 up to day 186 (Jul 5) on average, whereas the other three locations dropped below 4/10 in the 134-152 day range (May 14 - Jun 1). Part of the reason was the presence of the ice arch, which generated some OW and lower IC to the east of it. For the 10-year average, the ice arch collapsed on day 180 (Jun 29) with a standard deviation of 12 days, as per Table 3.6. The melt timelines in the three locations east of Resolute contributed to the average melt day of 153 (Jun 2) as per Tables 3.3 and 3.6. In the fall freeze season, all four locations rapidly freeze close together in time, as shown in Fig. 3.14.

4.1.4 Important Start/End Dates & ACIC Time of Year Limits

For the important start/end dates graph in Fig. 3.16, yearly dates for start/end of full OW, ice arch formation/collapse, and ACIC time of year limits were shown. The ice arch formation dates showed a similar trend between day 50-70 (Feb 19 - Mar 11) for 2016, 2017, 2020, 2021, and 2022, with outlier years being 2015, 2018, 2019, 2023 and 2024. However, even with this variability, the ice arch collapse dates were within a tighter range of days 172-195 (Jun 21 - Jul 14), with 2017 being the outlier at day 160 (Jun 9). The year 2018 had a very short OW season as compared to the other years. The ACIC always stopped working in the spring very near, yet prior to, the ice arch collapse dates, which was acceptable. As per Table 3.2, the 10-year average date that the ACIC stopped working was day 161 (Jun 10). By this point, it is only 20 days prior to the 10-year average ice arch collapse date of day 181 (Jun 29), and at that time of year, visual observation of AVHRR images using the visible channel was possible. The ACIC also stopped working in the close vicinity of the 10-year average melt day of day 153 (Jun 2) as per Table 3.3, where melt was defined as the majority of Lancaster Sound having an IC lower than 4/10. In the fall, the ACIC started working again on day 298 (Oct 25) as per

Table 3.2, 18 days after the full OW season ended on day 270 (Sep 27), which was acceptable though less ideal than the spring season, as there is insufficient daylight after end of September for AVHRR visible channel use in the region.

Overall, the ACIC worked for approximately 7+ months per year, from January-early June and late October-December, and some years it still worked in late September. For the 2015-2024 10-year average, the ACIC stopped working on day 161 (Jun 10) with a standard deviation of 5 days. The algorithm began working again on day 298 (Oct 25) with a standard deviation of 10 days. These limits are considered acceptable by the author of this thesis for the Lancaster Sound region, and likely also acceptable for other regions of the arctic with similar climates.

4.1.5 Seven-Day Continuous ACIC Results Analysis

Three time periods were selected for seven-continuous non-cloudy days assessment: Apr 1-7, 2023, 31 Jan - Feb 6, 2017, and Mar 12-18, 2018. During Apr 1-7, 2023, the ice arch was starting to form. The ACIC images in Fig. 3.17 clearly showed the formation of the ice arch, which was not discernible in the corresponding U Bremen AMSR-2 images in Fig. 3.18. During Apr 1-7, 2023, there was noticeable change in IC within a seven-day period in the AVHRR images, though there were only minor changes from one day to the next.

For the Jan 31 - Feb 6, 2017 period, the ice arch had not yet formed, but the IC was very high. Once again, the ACIC images in Fig. 3.19 showed more detail than the corresponding U Bremen AMSR-2 images in Fig. 3.20. This is likely due to the spatial resolution of the AVHRR images being 1.1 km and the U Bremen AMSR-2 images being 6.25 km. During this early period of the year, there was less IC change over a seven-day period, and minor changes from one day to the next.

For the Mar 12-18, 2018 period, the ice arch had not yet formed. The IC was high, in the 7-9/10 range, but lower than the CIS chart value of 9+/10 during the same time period. No ice fog was present during this time period. The mean temperature of the ice pack west of Resolute ranged between -35 to -31° C, using the spatial pixel editor. Fig. 3.21 shows the ACIC results, and Fig. 3.22 shows the U Bremen AMSR-2 PM-based results. The ACIC images in Fig. 3.21 show more ice detail in the rest of the Sound compared to the U Bremen AMSR-2 IC images in Fig. 3.22. There were only minor changes from one day to the next.

Overall, this analysis helped support the weekly use of AVHRR images for analyzing the 2015-2024 time period in Lancaster Sound, in terms of quantity of data to analyze and the minor changes from one day to the next. In addition,

the CIS ice charts are created on a weekly schedule, so it was attempted to align the AVHRR images with that schedule, allowing ± 2 days to maximize the number of non-cloudy images.

4.2 AVHRR Visible Channel/Band Isodata and Visual IC Analysis

This section discusses the results presented in Section 3.3. Visible channel IC analysis was conducted for non-cloudy days in May/June and September when it was too warm for the ACIC to work, but there was sufficient daylight present. For the isodata unsupervised classification analysis in ENVI, this method aided in estimating IC in images most of the time, where the ice distribution and presence was more complex. In situations where isodata results were inconclusive, visual analysis of the visible channel, with the guidance of Fig. 1.8, provided acceptable IC estimates. The uncertainty on both methods was set as 1.0 tenths due to the perceived imprecision. However, the isodata analysis was very quick to implement. A couple disadvantages were that it did require analyst interpretation to determine if one or more class colours was OW, and no additional ice characteristics could be obtained, except that the different colour ice classes were different from each other in some manner. Perhaps additional trials with three classes, to try and isolate OW, MIZ and pack ice could be explored in the future.

4.3 SAR Isodata IC Analysis

This section discusses the results presented in Section 3.4. For Sentinel-1 and RCM, both C-band SAR satellites, the isodata unsupervised classification method in ENVI seemed to work overall near the end of May and late October/early November, which was acceptable since this was near the melt and freeze seasons. In addition, differentiation between FYI and MYI was not needed, which was mentioned [54] as difficult during melt season.

Isodata IC results were not reliable when it was mostly OW or mostly ice. For OW, the SAR images were very *noisy*, which broke down the water into multiple colour classes. For days with almost all ice, the red class was probably smooth ice, and the various class colours denoted different types of ice or ice features. U Bremen AMSR-2 images were helpful in situating the observer for situations of all ice or all OW, as just looking at the SAR image on its own was sometimes ambiguous. In addition, it was determined that application of adaptive image filtering or smoothing in ENVI did not improve the SAR

images used for isodata analysis. Perhaps additional trials with three classes, to try and isolate OW, MIZ and pack ice could be explored in the future.

For some Sentinel-1 images, there were cloud-like rain areas partially obstructing Lancaster Sound, such as Jun 7, 2016 or Jun 12, 2017 in Fig. 3.25. It was difficult to tell what was beneath it from just looking at the SAR image, though this phenomenon did not occur often in the studied images. This phenomenon was also previously reported [82].

When examining Sentinel-1 and RCM images to use for analysis, HH polarized images provided more ice detail and contrast than the HV polarized ones. This seemed contradictory to RADARSAT-2 results [52], which stated that HV-polarized showed more ice/water contrast in their study. However, a different study using Sentinel-1 [81] did state that Sentinel-1 HH images were used since the HV had a lower signal-to-noise ratio than HH. A higher ratio is important for lower-intensity targets such as smooth FYI [81]. Furthermore, RCM images showed more detail in the HH polarization than in the HV one [60].

The Sentinel-1 modes used were mostly EW, as it provided a wide swath, and was also used previously in other studies [81, 83]. Occasionally, IW mode was used. For RCM, SC100M mode was mostly used, with occasionally SC50M and SCLN if SC100M was not available. Such modes were also used in previous studies [60, 84].

From examining the literature, as per Section 2.11, the isodata unsupervised classification of SAR images for IC determination appeared to be a novel low-complexity approach, though it did build upon the general concept of determining sea IC by pixel classification [54]. The Wackerman classification, which had been used in the past for SAR imagery [32], was more complex and was a type of supervised classification. The isodata unsupervised classification method applied for this research provided a useful method within its limitations, which required a reasonable mix of both ice and OW. Since SAR was used as a gap-filler for ACIC data on cloudy days, a rapid and simple approach was preferable.

4.4 ACIC Accuracy Assessment 2015-2024 and Arctic Applicability

This section discusses the results presented in Section 3.5.

4.4.1 ACIC and SAR Near-Concurrent Images Analysis

The first comparison was that of an ACIC image with a Sentinel-1 SAR image from Apr 22, 2015. From observing the ACIC, SAR, and U Bremen AMSR-2 IC images in Fig. 3.30 a), b) and c) respectively, similar ice characteristics were present in all three images. From a comparison of these characteristics, as well as visual inspection of the ACIC and SAR images, supports the position that the ACIC showed accurate results. In this case, the ACIC results in Fig. 3.30 a) better matched the SAR images in Fig. 3.30 b) and d) than did the U Bremen AMSR-2 IC image in Fig. 3.30 c).

The second comparison was that of an ACIC image with an RCM SAR image from Apr 16, 2022. For the RCM results comparison in Fig. 3.31, the same general patterns were present, however, in this case the isodata results in Fig. 3.31 e) were inconclusive. Nonetheless, the ACIC image in Fig. 3.31 a) and the SAR image in Fig. 3.31 b) and d) showed very similar ice characteristics as well as similar outlines of the formed ice arch. In this case, the U Bremen AMSR-2 IC results in Fig. 3.31 c) better matched the related ACIC and SAR images than the case in Fig. 3.30.

Overall, a near-concurrent comparison of ACIC images with SAR images provided confirmation of similar ice characteristics and shapes, which provided confidence that the ACIC was working accurately at classifying OW, ice and MIZ.

4.4.2 ACIC, CIS Ice Charts, U Bremen AMSR-2 Analysis

Fig. 3.32 shows the ACIC results with the gap-filling SAR and AVHRR visible channel data removed. The graph also only shows data for the periods of the year where ACIC worked accurately, based on the 10-year average. The U Bremen AMSR-2 and CIS ice charts data were plotted for the same time periods. Uncertainties were determined as per Section 2.9.2. From day 1-120 (Jan 1 - Apr 30) for the ACIC data in Fig. 3.13 and 3.32, removal of the SAR and AVHRR visible channel gap-filling data for Fig. 3.32 did not appreciably change the pattern of the results. Of the 172 data points in that time of year where the ACIC worked over the 10-year study period, 21 were gap-filled by SAR and zero by AVHRR visible channel. Therefore, 88% of the data points

were ACIC, but the SAR results had to be within comparable IC ranges to not change the pattern appreciably. From day 121-161 (May 1 - Jun 10) for Fig. 3.13 and 3.32, of the 60 data points over the 10-year study period, 18 were gap-filled by SAR and zero by AVHRR visible channel. Therefore 70% of the data points were ACIC, but the removal of the gap-filling data for Fig. 3.32 did not substantially change the results. From day 310-350 (Nov 6 - Dec 16) for the ACIC data in Fig. 3.13 and 3.32, removal of the SAR and visible channel ACIC data gap-filling data for Fig. 3.32 did not appreciably change the pattern of the results. Of the 58 data points in that time of year where the ACIC worked over the 10-year study period, 11 were gap-filled by SAR and zero by AVHRR visible channel. Therefore, 81% of the data points were ACIC, but the SAR results had to be within comparable IC ranges to not change the pattern appreciably.

In the early winter and spring timeframe, from day 1-148 (Jan 1 - May 28) in Fig. 3.32, ACIC results showed lower IC than the other two data sources, but the results started to converge with the U Bremen results around day 114 (Apr 24). From day 1-60 (Jan 1 - Mar 1), the U Bremen IC results and CIS ice chart IC results both showed steady values of approximately 9.5/10, while the ACIC results showed between 9-7.8/10 as time progressed. For March and April, the difference between U Bremen and ACIC results can be partially attributed to ACIC results having a much better spatial resolution of 1.1 km vs 6.25 km, where smaller groups of ice floes and pockets of OW can be differentiated, therefore increasing the ability to detect lower IC. Another reason for the difference could be that CIS ice charts have a category of 9+, which was set at a value of 9.5 for the research for this thesis. For U Bremen, the colour scale also had more colour increments in the 9-10/10 end of the IC spectrum, so values of 9.5 could be assigned. For the ACIC results, it was difficult to assign values of 9.5 based on the colour, so values of 9 or 10 were assigned. Perhaps this factor contributed to ACIC results being slightly lower.

Between day 1-113 (Jan 1 - Apr 23) in Fig. 3.32, the ACIC results were 0.2-1.6/10 lower than the U Bremen results not including uncertainties, with the gap closing very quickly afterwards. For the same date range, the ACIC results were 0.6-2.5/10 lower than the CIS ice chart IC results. The CIS ice charts are a combination of many data sources and are generally created conservatively [22]. However, the CIS ice chart average IC value of 9.5/10 extends from day 1-120 (Jan 1 - Apr 30), while the U Bremen IC results start dropping after day 60 (Mar 1). It is not known why this is the case for the CIS ice charts. During the year on average, the CIS ice charts showed very high IC, then IC dropped off rapidly towards OW in Lancaster Sound in the summer, as shown in both Fig. 3.13 and 3.32.

From day 60 to at least day 132 (Mar 1 - May 12) in Fig. 3.32, there was significant difference between the CIS ice chart results with both the U Bremen and ACIC results, not including uncertainties. From observing ACIC results in March over various years, provided in Appendix B, the ACIC images show that the IC was lower than 9.5/10. Ambient light started appearing in early April in the selected AVHRR images, with full daylight by May. The largest discrepancy period for ACIC results as compared to the CIS ice chart results was between day 91-148 (Apr 1 - May 28). One potential reason for lower values in April/May could be attributed to meltwater ponds on top of some regions of ice, which would bring the IC values down [40]. Another reason could be solar heating/insolation due to significant daylight in the region during May, which would also lower IC values. In addition, as per the ACIC error analysis in the Technical Note [76] in Appendix A, ACIC becomes less accurate as the SST rises. However, between day 127-162 (May 7 - Jun 11), the AVHRR and U Bremen AMSR-2 results did overlap at certain times. Overall in the spring, with uncertainties included, the ACIC results were in 100% agreement with the U Bremen AMSR-2 IC results. With uncertainties included, ACIC results were also in agreement with the CIS ice chart results, except for days 92 (Apr 2), 106 (Apr 16), 120 (Apr 30), and 127 (May 7).

In the fall timeframe, from day 295 (Oct 22) onwards, the IC values for all three data sources had a closer fit, with all three being in agreement with uncertainties included. The ACIC still consistently showed the lowest IC, but with the uncertainties included, it was very close to alignment with the U Bremen AMSR-2 data. However, as of day 308 (Nov 4), the CIS ice charts showed 9+/10 IC, while the ACIC and U Bremen showed more granularity and a more gradual rise to 9+/10 IC. The reason for the lower IC for the ACIC compared to the U Bremen results is due to the better spatial resolution of 1.1 km in the AVHRR images vs 6.25 km. The conservatism of the CIS ice charts could explain the difference between day 295-308 (Oct 22 - Nov 4). During that time period no daylight was present in Lancaster Sound. The CIS ice charts then showed a lengthy period of 9.5/10 from day 308-365 (Nov 4 - Dec 31).

Overall, the ACIC is considered reasonably accurate within the uncertainty range. Over the 10-year average, ACIC reported lower IC values compared to the more conservative and broader geographical scoped CIS ice charts, and also lower IC values than the U Bremen AMSR-2 PM results except for days 132-148 (May 12-28). Of the 34 weekly 10-year average data points in Fig. 3.32 comparing the three data sources including uncertainty ranges, ACIC was in agreement with the U Bremen AMSR-2 data for all 34 (100%) of them, and ACIC was in agreement with the CIS ice charts data for 30 of 34 (88%) of them.

One recommendation for increased accuracy for the ACIC method would be to modify the colour spectrum to allow for more differentiation between the 9/10 and 10/10 so that values of 9.5 could be determined if required.

4.4.3 ACIC Applicability to the Arctic

Based on the research work completed for this thesis, the ACIC is applicable to both arctic research and supporting operational monitoring/assessment of IC. The accuracy of ACIC was determined to be acceptable by the author of this thesis when compared with U Bremen AMSR-2 PM-based data, and CIS ice charts. The application of ACIC for this research was focused on the Lancaster Sound and Barrow Strait ROI, which is approximately a 500 km by 75 km sized seawater region, whereas the CIS ice charts and U Bremen IC maps are completed for a much larger Eastern Arctic region. Nonetheless, Lancaster Sound, which is an operationally significant section of the NWP, can be fully analyzed within one MetOp image swath. The MetOp images are available for free from NOAA [37], and are usually downloadable within a day or two. Therefore, near-realtime IC observation of Lancaster Sound or other desired regions of the arctic could be performed using the methodology in the research for this thesis, provided the ROI is not cloudy during the desired time period. It is recommended to trial ACIC in other parts of the Canadian Arctic such as other parts of the NWP or CAA, as well as trial ACIC on a larger region than Lancaster Sound, to assess its ability to analyze a larger region.

The following overall advantages of using ACIC for IC determination are as follows:

1. Provides better granularity (1.1 km resolution) than the AMSR-2 IC maps from U Bremen (6.25 km resolution);
2. On non-cloudy days, and during times of year when it is not too warm, which is approximately up to 8 months of the year, provides a good snapshot of the IC distribution in Lancaster Sound;
3. Provides good IC information on days where the visible channel does not give any information due to darkness;
4. Can make use of MetOp-A, MetOp-B or MetOp-C satellites;
5. Has a wide allowable sensor zenith angle operating range of 0-45°;
6. Provides better IC granularity in the spring melt season for Lancaster Sound than the CIS ice charts and U Bremen AMSR-2 PM IC maps; and
7. Provides a rapid method of analyzing IC. An AVHRR image can be obtained from NOAA in 1-2 days, and then using ENVI, the CASSTA and ACIC can be applied in less than a day.

The following overall disadvantages of using ACIC for IC determination are as follows:

1. It may not be easily applicable to regions larger than a 2700 km MetOp satellite image swath, such as the entire Eastern Arctic, unless a multiple swath mosaic can be generated;
2. It is limited by cloud cover;
3. The method does not provide as conservative a result as the U Bremen AMSR-2 IC maps or CIS ice charts; and
4. The accuracy of the ACIC may still need some further improvement based on the reported IC results and comparison with the U Bremen AMSR-2 and CIS ice charts IC results.

4.5 Lancaster Sound Sea Ice Melt/Freeze Dates Analysis 2015-2024

This Section discusses the results presented in Section 3.6. In comparing Tables 3.3 and 3.4 for the melt data, the differing resolutions between the AVHRR and U Bremen data could possibly account for the difference. Based on the finer spatial resolution of the AVHRR images, groups of smaller ice floes, and hence lower IC, would be detectable earlier in the year. No trend was determined between melt date and where the ice arch formed within Lancaster Sound in a particular year. Some SAR or AVHRR visible channel data aided in the determination of the ACIC melt dates.

The 10-year average melt date in Lancaster Sound was determined to be day 153 (Jun 2). The definition of melt date for the research for this thesis was when the majority (over 50 %) of Lancaster Sound had a sea IC below 4/10, which is the lower limit of the 4-6/10 open drift range. A 10-year average melt date of calendar day 153 aligned well with the literature, as a previous study of the northern route of the NWP using AVHRR [16], shown in Table 2.10, also determined a 10-year average melt date of day 153 for the same 2015-2024 time period. The definition of melt in [16] was based on a pixel-based threshold, where their algorithm identified melt onset timing by analyzing C-band SAR imagery backscatter variability exceeding specified threshold parameters compared to the mean winter backscatter. Another study from 1997-2014 for the CAA region [86], which is northwest of Lancaster Sound, determined an average melt day of 164 $\pm$ 4 days using SAR and a similar melt onset definition as [16]. According to the U Bremen AMSR-2 IC data obtained and analyzed for the research for this thesis, the average melt

date for 2015-2024 was day 160 (Jun 9), which is only seven days later than the ACIC results.

The 10-year average freeze date in Lancaster Sound was determined to be day 293 (Oct 20). The freeze date was reached once the majority (over 50 %) of Lancaster Sound had a sea IC above 6/10, which is the upper limit of the 4-6/10 open drift range. According to the U Bremen AMSR-2 IC data obtained and analyzed for the research for this thesis, the average freeze date for 2015-2024 was day 292 (Oct 19), which is only one day earlier than the ACIC results.

Calculation of the melt and freeze dates were slightly different than the dates that the ACIC line passes the 4/10 and 6/10 IC thresholds on Fig. 3.13. This is because the yearly melt dates were determined from examination of the ACIC and CASSTA results for the entire Lancaster Sound at once on a specific day, which is slightly different than the averaging of IC over four locations of Lancaster Sound, then averaged over 10-years. The standard deviations of the reported melt and freeze dates from Table 3.3 do include the dates shown on Fig. 3.13.

As a result of the research for this thesis, the ice arch formation and collapse dates in 2023 and 2024 were determined. For 2023, the ice arch formation/collapse dates were days 37 (Feb 6) and 192 (Jul 11). For 2024, the ice arch formation/collapse dates were days 118 (Apr 27) and 191 (Jul 9). Ice arch formation criteria was based on the ice arch formation occurring when it achieved the characteristic shape for the season [24]. Ice arch collapse criteria was based on the criteria of collapse being characterized by the breakdown of the structure [24]. Unfortunately, as per Table 3.6, there was no identifiable trend between the ice arch formation or ice arch collapse dates and the melt date. The overall average difference between ice arch formation and melt date was 83 days (standard deviation of 32 days), and the overall average difference between melt date and ice arch collapse was 27 days (standard deviation of 28 days).

A summary table of important dates including 10-year average for ice arch formation/collapse, melt/freeze dates, and full OW date ranges was presented in Table 3.7. This table was useful in determining recommended hydrophone and/or sonobuoy water deployment dates during the year.

4.6 Audimus Mission-related Hydrophones/Sonobuoys Deployment

This Section uses the results presented in Section 3.6 to make predictions. Lancaster Sound, over the time period 2015-2024 has been relatively ice free between mid-July to mid-September according to Section 1.4. Therefore, hydrophones could be positioned in the water or sonobuoys could be dropped into the water from aircraft anytime in that period. The more difficult prediction periods are the melting and freezing periods. By using the IC results from ACIC, as well as SAR image IC results and AVHRR visible channel image IC results, general times of year to position hydrophones or drop sonobuoys in the water in melt/freeze seasons could be determined.

Once the ice arch formed, there was typically OW to the east of it. Hydrophones or sonobuoys could be placed at that location as soon as the ice arch forms. The melt and freeze dates are defined in the research for this thesis as the majority of Lancaster Sound having an average IC of 4/10 or 6/10, respectively. Therefore, hydrophones/sonobuoys could be deployed in the water anytime between the melt date in the spring and the freeze date in the fall due to enough water being exposed. One benefit of the ACIC is that for 2015-2024, the average day in the spring that it became too warm for the algorithm to be accurate was calendar day 161 (Jun 10) with a standard deviation of 5 days (Table 3.2), which occurs after the average melt date of day 153 (Jun 2) with a standard deviation of 22 days (Table 3.3).

Depending on a ship's ice class, some ships will be able to traverse the Sound in the melt/freeze period where the IC is between 4-6/10. Fig. 1.5 showed the times of year that different classes of ships have traversed the NWP between 2013-2020, where FS 1A Super (equivalent to PC 6 ice strengthened, which can operate in medium FYI) and FS 1A/B/C classes (FS 1A equivalent to PC 7 and only strengthened for thin FYI conditions) could transit between mid-June to mid-October. This aligns well with the time period between the melt and freeze dates in Table 3.7. As per Fig. 1.5, FS 1A/B/C transits are highly concentrated during mid-July to mid-September, which is OW the majority of the time.

For PC 6 and PC 7 ice strengthened ships, it is recommended to deploy hydrophones/sonobuoys in the water in Lancaster Sound between the average melt and freeze dates of Jun 2 - Oct 20. An additional period of Mar 1 - Jun 2, where an appreciable region of OW was present east of the ice arch but bounded by ice further east, is another option for hydrophones/sonobuoys water deployment. This date range represents the period between average

ice arch formation and the average melt date, and could be used for PC 1 through PC 5 class ships, which can traverse FYI year-round [13], as well as other scientific purposes. For full OW ships that do not have icebreaking capability, the full OW period of Jul 26 - Sep 27 would apply. A summary is provided in Table 4.1. Table 3.7 provides additional details on the date ranges.

Table 4.1: Recommended times of year to deploy Audimus mission-related hydrophones and/or sonobuoys in the waters of Lancaster Sound, based on 2015-2024 data

Ship*	Time Period in Calendar Days (Dates)	Description
Polar Class (PC) 1 through 5 ice strengthened ships	60-293 (Mar 1 - Oct 20)	Between ice arch formation date and freeze date, containing an Open Water (OW) region east of the ice arch but bounded by ice further east.
PC 6 and 7 ice strengthened ships	153-293 (Jun 2 - Oct 20)	Between melt and freeze dates.**
OW ships	207-270 (Jul 26 - Sep 27)	Between full OW start and end dates

*PC 1-5 can traverse FYI year-round. PC 6 equivalent to FS 1A Super, PC 7 equivalent to FS 1A, and OW equivalent to FS II in the Finnish-Swedish classification system.

**Melt date defined as the majority of Lancaster Sound ($> 50\%$) reaching a 4/10 threshold IC, and freeze date defined as the majority of Lancaster Sound ($> 50\%$) reaching a 6/10 threshold IC.

5 Conclusions and Recommendations

5.1 Conclusions

5.1.1 Sea IC in Lancaster Sound 2015-2024 using ACIC

This subsection addresses objectives #1-2 in Section 2.15 of this thesis.

The following findings were determined:

1. An ice concentration (IC) algorithm, based on the Composite Arctic Sea Surface Temperature Algorithm (CASSTA) and using Advanced Very High Resolution Radiometer (AVHRR) satellite data from the MetOp-A, MetOp-B and MetOp-C satellites was developed and applied to 10-years (2015-2024) of AVHRR thermal infrared (TIR) images of Lancaster Sound in the Canadian Arctic. The algorithm was termed AVHRR CASSTA-based IC (ACIC). IC data and trends were successfully obtained;
2. Yearly graphs with weekly intervals, Figs. 3.3-3.12, aligned with the Canadian Ice Service (CIS) ice charts, were used to report ACIC results. A 10-year average IC graph, Fig. 3.13, was also created. ACIC results had to be gap-filled on cloudy days by Synthetic Aperture Radar (SAR) and AVHRR visible channel IC data, which was a beneficial method and provided sufficient overall data; and
3. Based on the change detection method used in ENVI for MetOp-A, MetOp-B and MetOp-C, the differences were minimal enough to rely on the MetOp-A-based Single-Channel CASSTA algorithm for MetOp-B and MetOp-C Level 1B AVHRR images.

Overall, the ACIC succeeded in providing insight into the IC of Lancaster Sound for non-cloudy AVHRR TIR images 2015-2024. Though originally developed for MetOp-A, ACIC was determined to be applicable to MetOp-B and -C satellites, which are still currently operational.

5.1.2 ACIC Effectiveness and Accuracy

This subsection addresses objective #3 in Section 2.15 of this thesis.

The following findings were determined:

1. Comparison, without including uncertainty ranges, of ACIC to CIS ice chart and University of Bremen Advanced Microwave Scanning Radiometer 2 (AMSR-2) passive microwave (PM) data sources: Over the 2015-2024 10-year period in Fig. 3.32, the ACIC reported the lowest IC values on average for the three data sources, but had a similar trend shape to the U Bremen AMSR-2 data. For instance, between Jan 1 - Apr 23 (days 1-113), the ACIC results were 0.2-1.6/10 lower than the U Bremen AMSR-2 IC results not including uncertainties, with the gap closing very quickly afterwards. For the same date range, the ACIC results were 0.6-2.5/10 lower than the CIS ice chart IC results, not including uncertainties. In March and April, the gap was wider between the ACIC results and the CIS ice chart values as the CIS ice charts reported consistent 9.5/10 IC on average until Apr 30 (day 120). In the fall, there was better agreement between the three data sources, with the ACIC still reporting the lowest IC values. ACIC reported lower IC values compared to the more conservative and broader geographical scoped CIS ice charts, and also lower IC values than the U Bremen AMSR-2 results, except for approximately May 12-28 (days 132-148) over a 10-year average;
2. Comparison, including uncertainty ranges, of ACIC to the CIS ice chart and U Bremen AMSR-2 PM IC data sources: Over the 2015-2024 10-year period in the spring in Fig. 3.32, the ACIC results were in agreement with the U Bremen AMSR-2 IC results. The ACIC results were also in agreement with the CIS ice chart IC results, except for four days: Apr 2 (day 92), Apr 16 (day 106), Apr 30 (day 120), and May 7 (day 127). In the fall timeframe, from Oct 22 (day 29) onwards, the IC values for all three data sources had a closer fit, with all three being in agreement with uncertainties included. For the full year in Fig. 3.32, of the 34 data points in the graph comparing the three data sources, created from 10-year averages, ACIC was in agreement with the U Bremen AMSR-2 IC data for all 34 (100%) of them with uncertainties included, and in agreement with the CIS ice charts IC data for 30 of 34 (88%) of them with uncertainties included. Overall, the ACIC is considered acceptably accurate within the uncertainty range, however, the accuracy could still be further improved;
3. ACIC provided better spatial resolution, 1.1 km at nadir compared to

the 6.25 km resolution of the U Bremen AMSR-2 data. This accounted for part of the lower IC results, as the ACIC images could identify and differentiate smaller sets of ice floes, which would appear as a solid mass at the 6.25 km lower spatial resolution;

4. ACIC worked in both darkness and daylight conditions;
5. ACIC was able to be quickly generated in ENVI once AVHRR images were obtained from the National Oceanic and Atmospheric Administration (NOAA) Comprehensive Large Array-Data Stewardship System (CLASS);
6. ACIC sensor zenith angle restriction of $< 45^{\circ}$ for best results, which is the same restriction for the Single-Channel CASSTA algorithm, was not a limiting factor on obtaining sufficient AVHRR images;
7. ACIC results were sensitive to melt season phenomena such as melt ponds and sea ice solar heating/insolation in the April/May/June time of year. The effects of these phenomena may have contributed to lower than expected IC values in that time period for certain years;
8. ACIC no longer worked accurately when the spatial pixel editor mean of the snow/ice pack in a Single-Channel CASSTA image of Lancaster Sound in ENVI was $>$ -3° C. This corresponded with a sea surface temperature (SST) $>$ -1.8° C. This could be confirmed by observing that the resulting ACIC image did not make sense when compared with the AVHRR TIR image;
9. The colour spectrum used for the ACIC did not have enough increments between 9/10 and 10/10 to allow for accurate estimates of 9.5/10. The CIS ice charts have a classification of 9+/10 between 9/10 and 10/10; and
10. The time of year limits in the spring and fall, when ACIC no longer worked accurately, was fairly consistent over the 10 year period: spring was Jun 10 (day 161) with a standard deviation of 5 days, and fall was Oct 25 (day 298) with a standard deviation of 10 days. Therefore ACIC worked for 7+ months of the year, providing good tracking of IC in Lancaster Sound.

Overall, the novel ACIC was determined to be acceptably accurate and applicable to the arctic region, though the accuracy could still be further improved. Although the ACIC data generally reported lower IC values than the CIS ice charts and U Bremen AMSR-2 PM IC data, the trend shapes were similar, and near full agreement was obtained for all three data sources when uncertainty ranges were included. ACIC also provides a rapid IC analysis method for non-cloudy days.

5.1.3 SAR and AVHRR Visible Channel/Band IC Gap-filling

This subsection addresses objective #4 in Section 2.15 of this thesis.

The following findings were determined:

1. For Sentinel-1 and RCM, both C-band SAR satellites, the isodata unsupervised classification method in ENVI generally worked near the end of May and late October/early November, which was acceptable since this was near the melt and freeze seasons;
2. When examining Sentinel-1 and RCM images to use for analysis, HH polarized images provided more ice detail and contrast than the HV polarized ones. Application of adaptive image filtering or smoothing in ENVI did not improve the SAR images used for isodata analysis;
3. AVHRR visible channel IC analysis was conducted for non-cloudy days in May/June and September when it was too warm for ACIC to work, yet there was sufficient daylight present. Use of the visual ice guide in Fig. 1.8 assisted in visually determining IC in some images. Isodata unsupervised classification analysis in ENVI most of the time aided in estimating IC in images where the ice distribution and presence was more complex;
4. Isodata unsupervised classification IC results for both SAR and AVHRR visible channel images were not reliable when it was mostly open water (OW) or mostly ice. For OW, the SAR images were very noisy, which broke down the water into multiple colour classes. For days with almost all ice, the red colour class was probably smooth ice, and the various class colours denoted different types of ice or ice features. U Bremen AMSR-2 IC images were helpful in situating the analyst for situations of all ice or all OW, as just looking at the SAR image on its own was sometimes ambiguous; and
5. The isodata analysis for both SAR and AVHRR visible channel images was very quick to implement. In general, consistent class colours were produced, with the red colour class being OW. However, the isodata analysis did require analyst interpretation to determine if one or more class colours was OW. In addition, no additional ice characteristics could be obtained, except that the different ice classes were different from each other in some manner.

Overall, the novel isodata unsupervised classification IC analysis of SAR and AVHRR visible channel images provided a rapid novel approach to estimate IC within a desired small region, in cases where there was a mix of ice and OW present.

5.1.4 Sea Ice Melt/Freeze Dates in Lancaster Sound 2015-2024

This subsection addresses objective #5 in Section 2.15 of this thesis.

The following findings were determined:

1. The 10-year average melt day in Lancaster Sound was determined to be Jun 2 (day 153). The definition of melt date for the research for this thesis was when the majority (over 50 %) of Lancaster Sound had a sea IC below 4/10, which is the lower limit of the 4-6/10 open drift range. A 10-year average melt date of calendar day 153 aligned well with the literature [16, 86]. According to the U Bremen data analyzed in the research for this thesis, the average melt date for 2015-2024 was Jun 9 (day 160), which was only seven days later than the ACIC results.
2. The 10-year average freeze day in Lancaster Sound was determined to be Oct 20 (day 293). The freeze date was reached once the majority (over 50 %) of Lancaster Sound had a sea IC above 6/10, which is the upper limit of the 4-6/10 open drift range. Oct 20 was only 1 day later than the freeze date calculated with the U Bremen data (Oct 19) analyzed in the research for this thesis;
3. The ice arch formation and collapse dates in 2023 were determined to be Feb 6 (day 37) and Jul 11 (day 192), respectively. For 2024, the ice arch formation and collapse dates were determined to be Apr 27 (day 118) and Jul 9 (day 191), respectively. This extends the work of [24]. Ice arch formation criteria was based on the ice arch formation occurring when it achieved the characteristic shape for the season [24]. Ice arch collapse criteria was based on the criteria of collapse being characterized by the breakdown of the structure [24]; and
4. There was no identifiable trend between the ice arch formation or ice arch collapse dates and the melt date. The overall average difference between ice arch formation and melt date was 83 days (standard deviation of 32 days), and the overall average difference between melt date and ice arch collapse was 27 days (standard deviation of 28 days).

Overall, 10-year average melt and freeze season dates were determined for Lancaster Sound using ACIC, gap-filled by SAR and AVHRR visible channel analysis. The melt date of Jun 2 (day 153) occurs before the Jun 10 (day 161) date that ACIC stopped working in the spring due to SST > -1.8° C, and the freeze date of Oct 20 (day 293) occurs shortly before the ACIC starts working again on Oct 25 (298). This is considered acceptable by the author of this thesis for ACIC use.

5.1.5 Audimus Mission Hydrophones/Sonobuoys Deployment

This subsection addresses objective #6 in Section 2.15 of this thesis.

The following findings were determined:

1. It was confirmed that when the ice arch forms for the season, there was generally OW to the east of it, even if the IC further east was much higher at that time of year; and
2. The ACIC functions close enough to the melt and freeze season dates to provide sufficient data.

Overall, the methodology used in the research for this thesis provided recommended times of year to deploy hydrophones and sonobuoys in the water in Lancaster Sound, to support the Audimus cubesat mission and other operational or research needs. These dates are provided in the Recommendations section (Section 5.2).

5.2 Recommendations

5.2.1 Sea IC in Lancaster Sound 2015-2024 using ACIC

The following recommendations are offered:

1. Use the ACIC to support operational or research needs in Lancaster Sound; and
2. Trial the algorithm in other parts of the Canadian Arctic such as other parts of the Northwest Passage or the Canadian Arctic Archipelago;

5.2.2 ACIC Effectiveness and Accuracy

The following recommendations are offered:

1. Trial the algorithm on a region larger than Lancaster Sound to assess its ability to analyze a larger region;
2. Modify the IC colour spectrum to add more increments between 9/10 and 10/10 to better match CIS ice charts; and
3. Investigate methods to further improve the accuracy of the ACIC.

5.2.3 SAR and AVHRR Visible Channel/Band IC Gap-filling

The following recommendations are offered:

1. Further refine the isodata unsupervised classification method for SAR and AVHRR visible channel images if refinement does not hinder the rapid application of the test; and

2. Further investigate various SAR polarimetry options for the isodata unsupervised classification method.

5.2.4 Sea Ice Melt/Freeze Dates in Lancaster Sound 2015-2024

No recommendations are offered for this subsection.

5.2.5 Audimus Mission Hydrophones/Sonobuoys Deployment

The following recommendations are offered, based on the 10-year analysis of Lancaster Sound from 2015-2024:

1. For Polar Class (PC) 6 and PC 7 ice strengthened ships, equivalent to Finnish-Swedish (FS) 1A Super and FS 1A, respectively, it is recommended to deploy hydrophones or sonobuoys in the waters of Lancaster Sound between the average melt and freeze dates, which are Jun 2 - Oct 20;
2. An additional period of Mar 1 - Jun 2, where an appreciable region of OW was present east of the ice arch but bounded by ice further east, is another option for hydrophones/sonobuoys water deployment. This date range represents the period between average ice arch formation date and the average melt date, and could be used for PC 1 through PC 5 class ships, which can traverse FYI year-round [13], as well as other scientific purposes. Therefore the overall recommended hydrophones/sonobuoys deployment date range for the PC 1 - 5 ship classes is Mar 1 - Oct 20;
3. For full OW ships that do not have icebreaking capability, the full OW period of Jul 26 - Sep 27 would apply; and
4. Investigate potential geobuoy use on ice packs in conjunction with water-based hydrophones and sonobuoys.

References

[1] A. Cook, J. Dawson, S. Howell, J. Holloway, and M. Brady, "Sea ice choke points reduce the length of the shipping season in the northwest passage," *Communications Earth & Environment*, vol. 5:362, pp. 1–11, 2024.

[2] Z. Kochanowicz, J. Dawson, and O. Mussells, "Shipping trends in Tallurutiup Imanga (Lancaster Sound), Nunavut from 1990 to 2018," *University of Ottawa Department of Geography, Environment and Geomatics publication*, 2020.

[3] W. Hu, G. Cervone, L. Trusel, and M. Yu, "Arctic accessibility: recent trend in observed ship tracks and validation of arctic transport accessibility model," *Annals of GIS*, vol. 30(4), p. 455–474, 2024.

[4] C. Min, Q. Yang, D. Chen, Y. Yang, X. Zhou, Q. Shu, and J. Liu, "The emerging arctic shipping corridors," *Geophysical Research Letters*, vol. 49, no. 10, pp. 786–797, 2022.

[5] Carnaghan M. and Goody, A., "Canadian Arctic Sovereignty," tech. rep., Parliamentary Information and Research Service Ottawa, 2006.

[6] J. Kraska, "International security and international law in the Northwest Passage (article from 2009)," *Vanderbilt Journal of Transnational Law*, vol. 42, pp. 1109–1132, 2021.

[7] R. Huebert, "Submarines, oil tankers, and icebreakers: trying to understand Canadian Arctic sovereignty and security," *International Journal*, vol. 66, no. 4, pp. 809–824, 2011.

[8] M. Fernandes, K. Rasouli, P. Golubkin, A. Dolatshah, I. Radchenko, U. Prokhorova, A. Dixit, A. E., A. Arunkarthik, Acharya, B. Senapati, B. Nela, C. Shah, C. M.C., D. Kumar, J. Neelam, M. T.M., P. Behera, P. Thind, and E. Shalina, "Comparing recent changes in the arctic and the third pole: linking science and policy," *Polar Geography*, Aug 2022.

[9] Britannica, "Northwest Passage." https://www.britannica.com/place/Northwest-Passage-trade-route, 2025.

[10] Col Pierre LeBlanc (Ret'd), "The need for underwater surveillance in the arctic." Vanguard, https://vanguardcanada.com/the-need-for-underwater-surveillance-in-the-arctic/, 2021.

[11] M. D. Anderson, "Examination of an acoustic data source and payload for the Audimus cubesat mission," Master's thesis, Royal Military College of Canada, 2024.

[12] S. C. Tarla, "A satellite-augmented acoustic surveillance system for the Canadian Arctic," Master's thesis, Royal Military College of Canada, 2023.

[13] Transport Canada, "Polar classes." https://tc.canada.ca/en/marine-transportation/arctic-shipping/polar-classes, 2010.

[14] Sjöfartsverket, "Ice classes and requirements." https://www.sjofartsverket.se/en/services/icebreaking/ice-classes-and-requirements/, 2021.

[15] Traficom, "Finnish ice classes equivalent to class notations and establishing the ice classes of ships." https://www.finlex.fi/api/media/authority-regulation/687392/mainPdf/main.pdf, 2024.

[16] S. E. Howell, A. Cabaj, D. G. Babb, J. C. Landy, J. Dawson, M. Mahmud, and M. Brady, "Near sea ice-free conditions in the northern route of the Northwest Passage at the end of the 2024 melt season," *The Cryosphere*, vol. 19, no. 12, pp. 6711–6725, 2025.

[17] Royal Military College of Canada, "Audimus preliminary critical design review (presented to the Canadian Space Agency in april 2025)," 2025.

[18] J. Hamilton, S.B. Martin, N.E. Chorney, A.J. Cole, P. Borys, "Arctic Buoy Component Investigations," tech. rep., JASCO Applied Sciences, 2023.

[19] J. M. Hamilton and M. D. Pittman, "Sea-ice freeze-up forecasts with an operational ocean observatory," *Atmosphere-Ocean*, vol. 53, no. 5, pp. 595–601, 2015.

[20] C. Richards, M. Pittman, K. Phelan, S. Nudds, and J. Hamilton, "The Barrow Strait Real Time Observatory: under-ice monitoring in the canadian high arctic," in *Proceedings of the 12th International Conference on Underwater Networks & Systems*, pp. 1–7, 2017.

[21] Ultra Maritime, "AN/SSQ 573 Passive Directional Multi-Mode Sonobuoy." https://umaritime.com/wp-content/uploads/2024/02/SSQ-573-Directional-Passive-Multi-mode-Sonobuoy-Feb-2024.pdf, 2024.

[22] M. Shokr and N. K. Sinha, *Sea Ice Physics and Remote Sensing: 2nd Edition*. New Jersey, USA: John Wiley and Sons, Inc., 2023.

[23] Transport Canada - Marine Transportation and the National Research Council, "Arctic ice regime shipping system - pictorial guide." https://tc.canada.ca/en/marine-transportation/marine-safety/arctic-ice-regime-shipping-system-pictorial-guidecomparison-of-in-for-each-class, 2018.

[24] R. F. Vincent, "An assessment of the Lancaster Sound polynya using satellite data 1979 to 2022," *Remote Sensing*, vol. 15, no. 4, 2023.

[25] J. Key and M. Haefliger, "Arctic ice surface temperature retrieval from avhrr thermal channels," *Journal of Geophysical Research: Atmospheres*, vol. 97, no. D5, pp. 5885–5893, 1992.

[26] R. Lindsay and D. Rothrock, "The calculation of surface temperature and albedo of arctic sea ice from AVHRR," *Annals of Glaciology*, vol. 17, pp. 391–397, 1993.

[27] R. F. Vincent, R. F. Marsden, P. J. Minnett, K. A. M. Creber, and J. R. Buckley, "Arctic waters and marginal ice zones: A Composite Arctic Sea Surface Temperature Algorithm using satellite thermal data," *Journal of Geophysical Research: Oceans*, vol. 113, no. C4, 2008.

[28] G. Dybkjær, R. Tonboe, and J. Høyer, "Arctic surface temperatures from MetOp AVHRR compared to in situ ocean and land data," *Ocean Science*, vol. 8, no. 6, pp. 959–970, 2012.

[29] R. F. Vincent, "The case for a Single Channel Composite Arctic Sea Surface Temperature Algorithm," *Remote Sensing*, vol. 11, no. 20, 2019.

[30] P. Minnett, A. Alvera-Azcárate, T. Chin, G. Corlett, C. Gentemann, I. Karagali, X. Li, A. Marsouin, S. Marullo, E. Maturi, R. Santoleri, S. Saux Picart, M. Steele, and J. Vazquez-Cuervo, "Half a century of satellite remote sensing of sea-surface temperature," *Remote Sensing of Environment*, vol. 233, p. 111366, 2019.

[31] M. G. Lobb, "An Investigation of the Relationship Between the Skin Temperature of the Sea Surface and the Temperature of the Dynamically Significant Surface Layer," Master's thesis, Royal Military College of Canada, 2012.

[32] S. Sandven and O. Johannessen, *Remote Sensing of the Marine Environment, Manual of Remote Sensing: 3rd Edition*, vol. 6, ch. 8: Sea Ice Monitoring by Remote Sensing, pp. 241–283. Maryland, USA: American Society for Photogrammetry and Remote Sensing, Jan 2006.

[33] M. A. Killie, Ø. Godøy, S. Eastwood, and T. Lavergne, "Algorithm theoretical basis document for the EUMETSAT ocean & sea ice satellite application facility regional ice edge product," *Ocean & Sea Ice SAF project report no. OSI-146, Version*, vol. 1, 2011.

[34] D. Battles, R. Lambeck, A. Pérez Albiñana, H. Bauch, and J. Ackermann, "In-orbit performance of the AVHRR, HIRS, and AMSU-A instruments on-board the MetOp-A and MetOp-B satellites," *Proc SPIE*, vol. 8867, Sep 2013.

[35] C. Elachi and J. V. Zyl, *Introduction to the Physics and Techniques of Remote Sensing (2nd Ed.)*. 2006.

[36] K. D. Klaes, J. Ackermann, C. Anderson, Y. Andres, T. August, R. Borde, B. Bojkov, L. Butenko, A. Cacciari, D. Coppens, M. Crapeau, S. Guedj, O. Hautecoeur, T. Hultberg, R. Lang, S. Linow, C. Marquardt, R. Munro, C. Pettirossi, G. Poli, F. Ticconi, O. Vandermarcq, M. Vasquez, and M. Vazquez-Navarro, "The EUMETSAT polar system: 13+ successful years of global observations for operational weather prediction and climate monitoring," *Bulletin of the American Meteorological Society*, vol. 102, no. 6, pp. E1224 – E1238, 2021.

[37] National Oceanic and Atmospheric Administration (NOAA), "Comprehensive Large Array Data Stewardship System (CLASS)." https://www.aev.class.noaa.gov/saa/products/, 2025.

[38] NOAA Office of Satellite and Product Operations, "POES Performance Status." https://www.ospo.noaa.gov/operations/poes/status.html, 2025.

[39] NV5 Geospatial Software, "ENVI Remote Sensing Software for Image Processing and Analysis." https://www.nv5geospatialsoftware.com/Products/ENVI, 2025.

[40] K. A. Scott, M. Buehner, A. Caya, and T. Carrieres, "A preliminary evaluation of the impact of assimilating AVHRR data on sea ice concentration analyses," *Remote Sensing of Environment*, vol. 128, pp. 212–223, 2013.

[41] E. P. McClain, "Multiple atmospheric-window techniques for satellite-derived sea surface temperatures," in *Oceanography from space*, pp. 73–85, Springer, 1981.

[42] E. P. McClain, W. G. Pichel, and C. C. Walton, "Comparative performance of AVHRR-based multichannel sea surface temperatures," *Journal of Geophysical Research: Oceans*, vol. 90, no. C6, pp. 11587–11601, 1985.

[43] K. Kilpatrick, G. P. Podestá, and R. Evans, "Overview of the NOAA/NASA advanced very high resolution radiometer Pathfinder algorithm for sea surface temperature and associated matchup database," *Journal of Geophysical Research: Oceans*, vol. 106, no. C5, pp. 9179–9197, 2001.

[44] Y. Liu, R. Dworak, and J. Key, "Ice surface temperature retrieval from a single satellite imager band," *Remote Sensing*, vol. 10, no. 12, p. 1909, 2018.

[45] Y. Li, T. Liu, M. E. Shokr, Z. Wang, and L. Zhang, "An improved single-channel polar region ice surface temperature retrieval algorithm using Landsat-8 data," *IEEE Transactions on Geoscience and Remote Sensing*, vol. 57, no. 11, pp. 8557–8569, 2019.

[46] R. F. Vincent, "The effect of arctic dust on the retrieval of satellite derived sea and ice surface temperatures," *Sci Rep*, vol. 8, p. 9727, 2018.

[47] R. F. Vincent, "An examination of the non-formation of the north water polynya ice arch," *Remote Sensing*, vol. 12, no. 17, 2020.

[48] B. A. Burns, M. Schmidt-Grottrup, and T. Viehoff, "Methods for digital analysis of AVHRR sea ice images," *IEEE transactions on geoscience and remote sensing*, vol. 30, no. 3, pp. 589–602, 1992.

[49] W. N. Meier, "Comparison of passive microwave ice concentration algorithm retrievals with AVHRR imagery in arctic peripheral seas," *IEEE Transactions on geoscience and remote sensing*, vol. 43, no. 6, pp. 1324–1337, 2005.

[50] P. Nielsen-Englyst, J. L. Høyer, K. S. Madsen, R. Tonboe, G. Dybkjær, and E. Alerskans, "In situ observed relationships between snow and ice surface skin temperatures and 2 m air temperatures in the arctic," *The Cryosphere*, vol. 13, no. 3, pp. 1005–1024, 2019.

[51] R. F. Vincent, "Ice concentration algorithm using single channel CASSTA," tech. rep., Department of Physics and Space Science, Royal Military College of Canada, 2025 (unpublished).

[52] Y. Lu, B. Zhang, and W. Perrie, "Arctic sea ice and open water classification from spaceborne fully polarimetric synthetic aperture radar," *IEEE Transactions on Geoscience and Remote Sensing*, vol. 61, pp. 1–13, 2023.

[53] National Aeronautics and Space Administration (NASA), "Synthetic Aperture Radar (SAR)." https://www.earthdata.nasa.gov/learn/earth-observation-data-basics/sar, 2025.

[54] H. Lyu, W. Huang, and M. Mahdianpari, "A meta-analysis of sea ice monitoring using spaceborne polarimetric SAR: Advances in the last decade," *IEEE Journal of Selected Topics in Applied Earth Observations and Remote Sensing*, vol. 15, pp. 6158–6179, 2022.

[55] M. E. Shokr, Z. Wang, and T. Liu, "Sea ice drift and arch evolution in the robeson channel using the daily coverage of Sentinel-1 SAR data for the 2016-2017 freezing season," *The Cryosphere*, vol. 14, no. 11, pp. 3611–3627, 2020.

[56] H. Peter, A. Jäggi, J. Fernández, D. Escobar, F. Ayuga, D. Arnold, M. Wermuth, S. Hackel, M. Otten, W. Simons, P. Visser, U. Hugentobler, and P. Féménias, "Sentinel-1A – first precise orbit determination results," *Advances in Space Research*, vol. 60, no. 5, pp. 879–892, 2017.

[57] European Space Agency (ESA), "Sentinel-1." https://www.esa.int/ Applications/Observing_the_Earth/Copernicus/Sentinel-1, 2025.

[58] European Space Agency, "Overview of Sentinel-1 Mission." https://sentiwiki.copernicus.eu/web/s1-mission, 2026.

[59] G. Kroupnik, D. De Lisle, S. Côté, M. Lapointe, C. Casgrain, and R. Fortier, "RADARSAT Constellation Mission overview and status," in *2021 IEEE Radar Conference (RadarConf21)*, pp. 1–5, IEEE, 2021.

[60] M. Dabboor, I. Olthof, M. Mahdianpari, F. Mohammadimanesh, M. Shokr, B. Brisco, and S. Homayouni, "The RADARSAT Constellation Mission core applications: First results," *Remote Sensing*, vol. 14, no. 2, pp. 301–320, 2022.

[61] A. S. Komarov, A. Caya, L. Pogson, and M. Buehner, "Assimilation of RCM data in the Canadian ice concentration analysis system," *Remote Sensing of Environment*, vol. 306, no. 114113, 2024.

[62] European Space Agency, "Copernicus Data Space Ecosystem." https://scihub.copernicus.eu, 2025.

[63] National Resources Canada, "Earth Observation Data Management System (EODMS)." https://www.eodms-sgdot.nrcan-rncan.gc.ca/index-en.html, 2025.

[64] MDA Systems Ltd., "RADARSAT constellation mission image product format definition: RCM-SP-53-0419," tech. rep., June 2021.

[65] Canadian Ice Service (CIS) - Environment and Climate Change Canada, "Eastern arctic regional ice charts." https://www.canada.ca/en/environment-climate-change/services/ice-forecasts-observations/latest-conditions/products-guides/chart-descriptions.html, 2025.

[66] Environment Canada, "Manual of Ice (MANICE)," tech. rep., Environment Canada, 2005.

[67] National Snow and Ice Data Center, "Canadian Ice Service, 2009. Canadian Ice Service Arctic Regional Sea Ice Charts in SIGRID-3 Format, Version 1 User Guide.," tech. rep., National Snow and Ice Data Center, Boulder, Colorado, USA, 2009.

[68] S. Howell, D. Babb, J. C. Landy, G. Moore, T. Ballinger, K. McNeil, B. Montpetit, and M. Brady, "Baffin bay ice export and production from sentinel-1, the radarsat constellation mission, and cryosat-2: 2016–2022," *Geophysical Research Letters*, vol. 51, no. 22, p. e2024GL111364, 2024.

[69] L. Wang, *Learning to Estimate Sea Ice Concentration from SAR Imagery.* PhD thesis, University of Waterloo, 2016.

[70] M. Buehner, A. Caya, L. Pogson, T. Carrieres, and P. Pestieau, "A new Environment Canada regional ice analysis system," *Atmosphere-Ocean*, vol. 51, no. 1, pp. 18–34, 2013.

[71] Institute of Environmental Physics at the University of Bremen, "Sea Ice Remote Sensing - Arctic Sea Ice Concentration." https://seaice.uni-bremen.de/sea-ice-concentration/amsre-amsr2/, 2025.

[72] H. Tsutsui, K. Imaoka, M. Kachi, T. Maeda, M. Kasahara, N. Ito, T. Oki, and H. Shimoda, "Present status of the global change observation mission 1st - water 'SHIZUKU' (GCOM-W1) and the advanced microwave scanning radiometer 2 (AMSR2)," in *Earth Observing Missions and Sensors: Development, Implementation, and Characterization III* (X. Xiong and H. Shimoda, eds.), vol. 9264, p. 92640E, International Society for Optics and Photonics, SPIE, 2014.

[73] National Aeronautics and Space Administration (NASA), "Advanced Microwave Scanning Radiometer EOS." https://www.earthdata.nasa.gov/data/instruments/amsr-e, 2025.

[74] G. Spreen, L. Kaleschke, and G. Heygster, "Sea ice remote sensing using AMSR-E 89-Ghz channels," *Journal of Geophysical Research: Oceans*, vol. 113, no. C2, 2008.

[75] E. Svendsen, C. Matzler, and T. C. Grenfell, "A model for retrieving total sea ice concentration from a spaceborne dual-polarized passive microwave instrument operating near 90 Ghz," *International Journal of Remote Sensing*, vol. 8, no. 10, pp. 1479–1487, 1987.

[76] R. F. Vincent, "Ice concentration algorithm using single channel CASSTA error analysis," tech. rep., Department of Physics and Space Science, Royal Military College of Canada, 2026 (unpublished).

[77] Stephanie Bell, "The Beginner's Guide to Uncertainty of Measurement (Good Practice Guide No. 11)." https://www.npl.co.uk/getattachment/63c00201-a38d-44e5-8470-2440284c3dfe/gpg11_uncertainty.pdf?lang=en-GB, 2013.

[78] NV5 Geospatial, "Isodata." https://www.nv5geospatialsoftware.com/docs/ISODATAClassification.html, 2026.

[79] NV5 Geospatial, "K-Means." https://www.nv5geospatialsoftware.com/docs/KMeansClassification.html, 2026.

[80] J. Karvonen, "A sea ice concentration estimation algorithm utilizing radiometer and SAR data," *Cryosphere*, vol. 8, no. 5, pp. 1639–1650, 2014.

[81] R. K. Scharien and S. Nasonova, "Incidence angle dependence of texture statistics from Sentinel-1 HH-polarization images of winter arctic sea ice," *IEEE Geoscience and Remote Sensing Letters*, vol. 19, pp. 1–5, 2022.

[82] W. Alpers, Y. Zhao, A. A. Mouche, and P. W. Chan, "A note on radar signatures of hydrometeors in the melting layer as inferred from Sentinel-1 SAR data acquired over the ocean," *Remote Sensing of Environment*, vol. 253, p. 112177, 2021.

[83] J. Karvonen, "Baltic sea ice concentration estimation using Sentinel-1 SAR and AMSR2 microwave radiometer data," *IEEE Transactions on Geoscience and Remote Sensing*, vol. 55, no. 5, pp. 2871–2883, 2017.

[84] G. Macdonald, R. Scharien, K. Duncan, S. Farrell, P. Rezania, and A. Tavri, "Arctic sea ice topography information from RADARSAT Constellation Mission (RCM) synthetic aperture radar (SAR) backscatter," *Geophysical Research Letters*, vol. 51, 2024.

[85] M. Dabboor, B. Montpetit, and S. Howell, "Assessment of the high resolution SAR mode of the RADARSAT Constellation Mission for first year ice and multiyear ice characterization," *Remote Sensing*, vol. 10, no. 4, 2018.

[86] M. Mahmud, S. Howell, T. Geldsetzer, and J. Yackel, "Detection of melt onset over the northern Canadian Arctic Archipelago sea ice from RADARSAT, 1997–2014," *Remote Sensing of Environment*, vol. 178, pp. 59–69, 2016.

[87] J. Zheng, T. Geldsetzer, and J. Yackel, "Snow thickness estimation on first-year sea ice using microwave and optical remote sensing with melt modelling," *Remote Sensing of Environment*, vol. 199, pp. 321–332, 2017.

[88] National Research Council of Canada, "Sunrise/sunset (full year, Nautical Twilight) for RESOLUTE NU for 2016." https://nrc.canada.ca/en/research-development/products-services/software-applications/sun-calculator/, 2020.

[89] National Snow and Ice Data Center, "Day of the Year (DOY) Calendar." https://nsidc.org/data/user-resources/help-center/day-year-doy-calendar, 2025.

Appendices

A Technical Notes Related to the ACIC

Two Technical Notes provide amplification and a basis for the ACIC. The references cited in this Appendix are related to each specific Technical Note and not the main thesis references section.

A.1 Technical Note - ACIC using Single-Channel CASSTA

Ice Concentration Algorithm using Single-Channel CASSTA

Technical Note - January 2025

Dr. R.F. Vincent, Professor
Department of Physics and Space Science
Royal Military College of Canada

Sea and ice surface temperatures can be determined using the single channel Composite Arctic Sea Surface Temperature Algorithm (CASSTA) [1]. The algorithm uses Channel 4 to determine the temperature of three regimes: sea surface, ice surface and marginal ice zones containing a combination of seawater and ice. The application of a single channel in the dry Arctic climate addresses potential inaccuracies of split window algorithms that use the difference between 11 µm and 12 µm brightness temperatures as a proxy for atmospheric absorption of thermal infrared energy [2].

Sea ice concentration (IC) may be estimated through using single-channel CASSTA. Open water during the colder months in Arctic waters will be near the freezing point of seawater (-1.8° C). If leads are narrower than the minimum spatial resolution (1.1 km), the resulting temperature for that pixel will be

a combination of open water (-1.8° C) and the surrounding snow/ice, which will approximate the surface air temperature [3,4]. The average single-channel CASSTA temperature of nearby ice is compared to pixels that contain open water. A linear relation between the average ice temperature and the deviation from -1.8° C of each pixel gives tenths IC,

$$IC = \left[\frac{(b1 + 1.8)}{(b9 + 1.8)}\right] (10) \tag{A.1}$$

where $b1$ is the single channel CASSTA temperature (° C) and $b9$ is the average temperature of the nearby ice (° C). Pending validation, it is expected that this method will improve upon the spatial and temporal resolution of published ice charts during periods when open water is -1.8° C.

References

[1] Vincent, R. The Case for a Single Channel Composite Arctic Sea Surface Temperature Algorithm. *Remote Sens.* 2019, 11, 2393.
[2] Vincent, R.F.; Marsden, R.F.; Minnett, P.J.; Buckley, J.R. Arctic waters and marginal ice zones: 2. An investigation of arctic atmospheric infrared absorption for advanced very high resolution radiometer sea surface temperature estimates. *J. Geophys. Res.* 2008, 113, C08044.
[3] Nielsen-Englyst, P.; Høyer, J. L.; Madsen, K. S.; Tonboe, R.; Dybkjær, G.; Alerskans, E. In situ observed relationships between snow and ice surface skin temperatures and 2 m air temperatures in the Arctic. *The Cryosphere.* 2019, 13, 1005–1024. https://doi.org/10.5194/tc-13-1005-2019.
[4] Nielsen-Englyst, P., Høyer, J. L., Madsen, K. S., Tonboe, R. T., Dybkjær, G., and Skarpalezos, S.: Deriving Arctic 2 m air temperatures over snow and ice from satellite surface temperature measurements, *The Cryosphere.* 2021, 15, 3035–3057. https://doi.org/10.5194/tc-15-3035-2021.

Citation:

Vincent, R.F. (2025). Ice Concentration Algorithm using Single Channel CASSTA. [Unpublished technical note]. Department of Physics and Space Science, Royal Military College of Canada.

A.2 Technical Note - ACIC using Single-Channel CASSTA Error Analysis

Ice Concentration Algorithm using Single Channel CASSTA Error Analysis

Technical Note - February 2026

Dr. R.F. Vincent, Professor
Department of Physics and Space Science
Royal Military College of Canada

For single-channel CASSTA pixels where $b4 < 268.95$ K, the IST algorithm is applied, introducing a warm bias if there is open water within the pixel. The bias occurs because the IST portion of the algorithm returns a higher temperature than the SST for a pixel brightness temperature owing to the higher emissivity of ice in the AVHRR Channel 4 regime.

- The warm bias affects ice concentration calculation by inflating the amount of open water as a function of air/ice temperature and open water.
- Error increases with increasing air temperature and open water, with an estimated maximum of +0.6/10 to +1.0/10 at 1/10 coverage for air/ice temperatures -40° C to -20° C respectively (Figure 1).
- For air/ice temperatures warmer than -20° C, the marginal ice zone portion of single channel CASSTA takes effect for low ice coverage.
- The algorithm may be improved by accounting for these systematic errors based on air/ice temperature and calculated ice concentration.

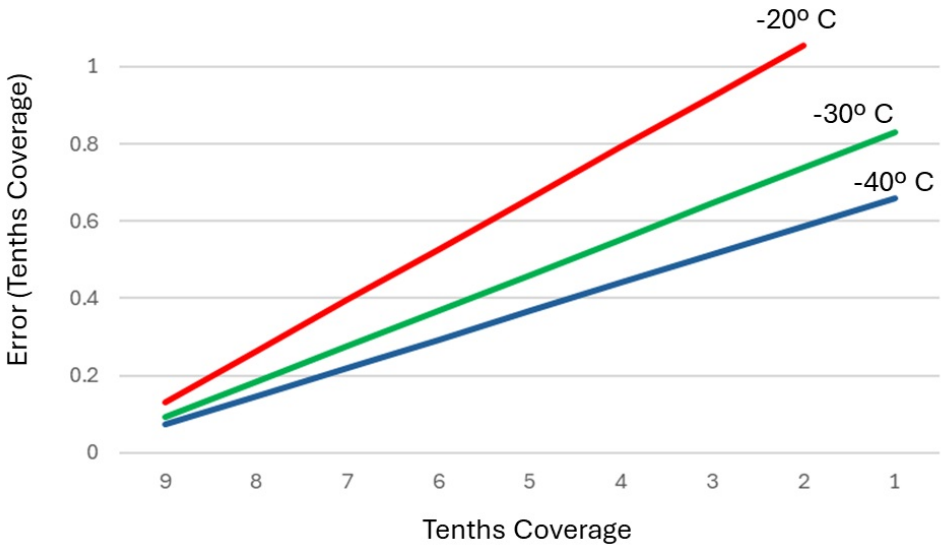

Figure 1. Estimated CASSTA IC error due to warm bias for -20° C, -30° C and -40° C air/ice temperature for 9/10 to 1/10 ice coverage.

Citation:

Vincent, R.F. (2026). Ice Concentration Algorithm using Single Channel CASSTA Error Analysis. [Unpublished technical note]. Department of Physics and Space Science, Royal Military College of Canada.

B Weekly ACIC Images of Lancaster Sound 2015-2024

Figs. B.1- B.20 show the weekly ACIC images for the various years between 2015-2024 using MetOp-A, -B or -C satellite data and ACIC, which is based on the Single-Channel CASSTA algorithm. The ACIC images shown were all during the times of year where the ACIC worked accurately. All images were generated in ENVI v5.7. Blank white areas means that the ACIC image did not fill the entire area that the black land mask template covers. Table B.1 outlines which Figures correspond to which year.

Table B.1: Figure references by year for ACIC images of Lancaster Sound

Year	Applicable Figures
2015	Fig. B.1- B.2
2016	Fig. B.3- B.4
2017	Fig. B.5- B.6
2018	Fig. B.7- B.8
2019	Fig. B.9- B.10
2020	Fig. B.11- B.12
2021	Fig. B.13- B.14
2022	Fig. B.15- B.16
2023	Fig. B.17- B.18
2024	Fig. B.19- B.20

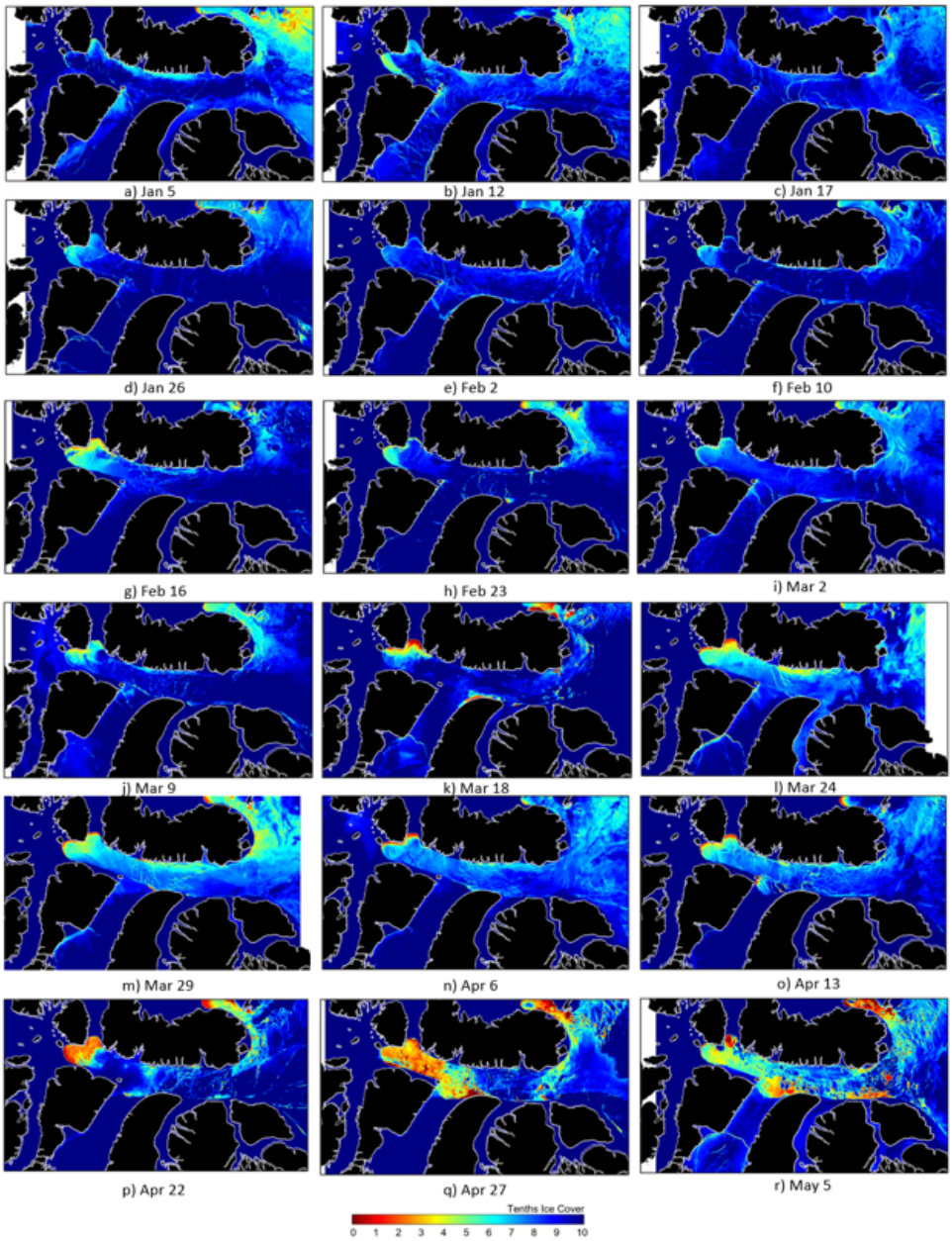

Figure B.1: 2015 ACIC Images of Lancaster Sound using MetOp-A Satellite Data: Jan 5 - May 5

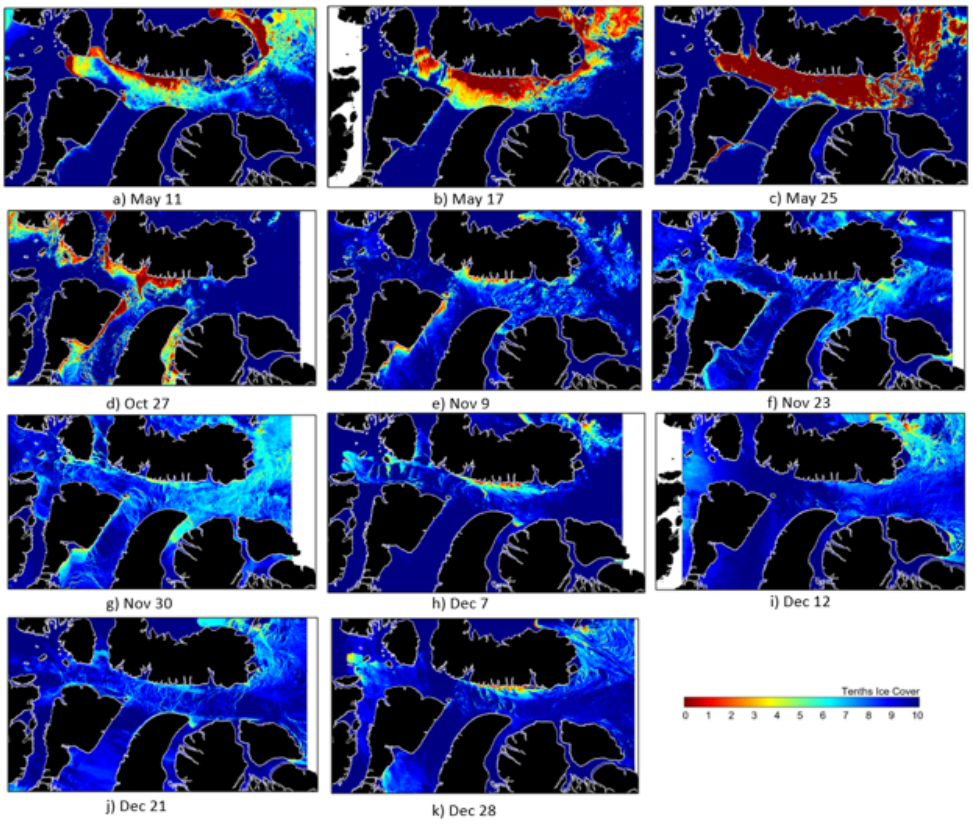

Figure B.2: 2015 ACIC Images of Lancaster Sound using MetOp-A Satellite Data: May 11 - Dec 28

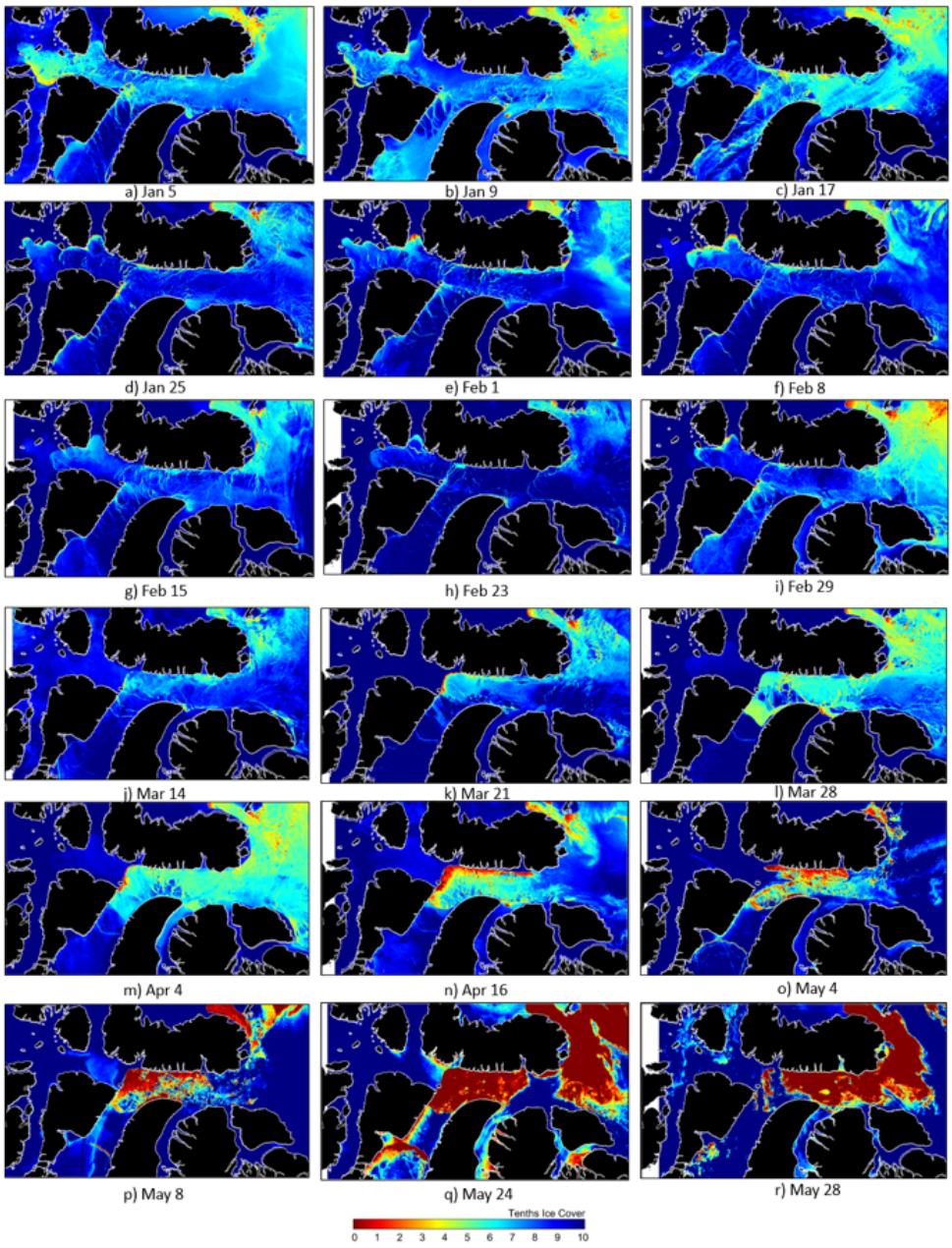

Figure B.3: 2016 ACIC Images of Lancaster Sound using MetOp-A Satellite Data: Jan 5 - May 28

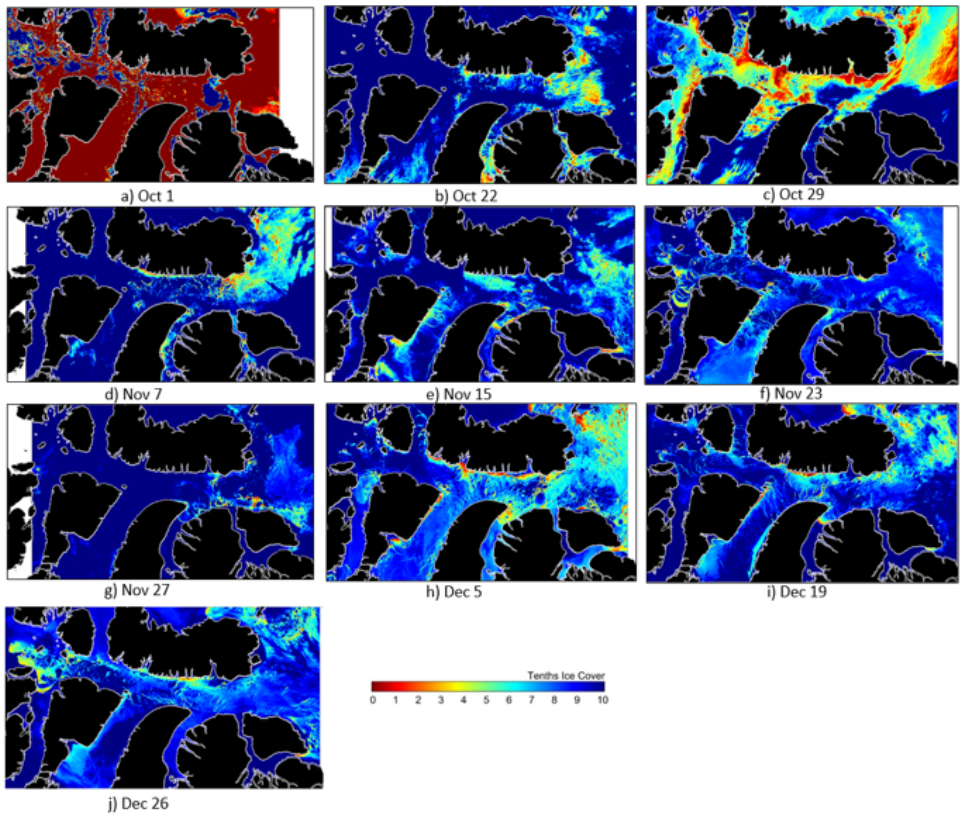

Figure B.4: 2016 ACIC Images of Lancaster Sound using MetOp-A Satellite Data: Oct 1 - Dec 26

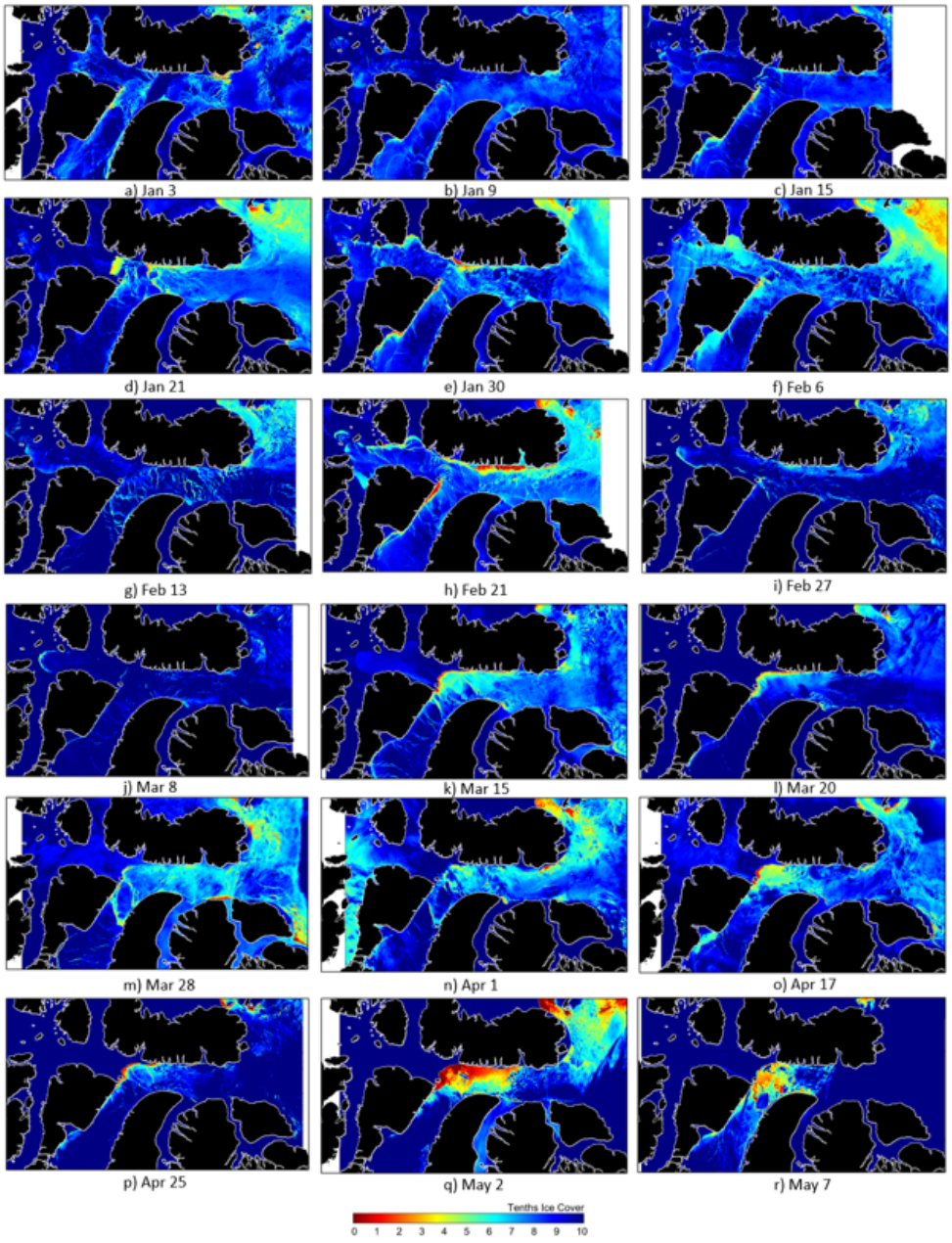

Figure B.5: 2017 ACIC Images of Lancaster Sound using MetOp-A Satellite Data: Jan 3 - May 7

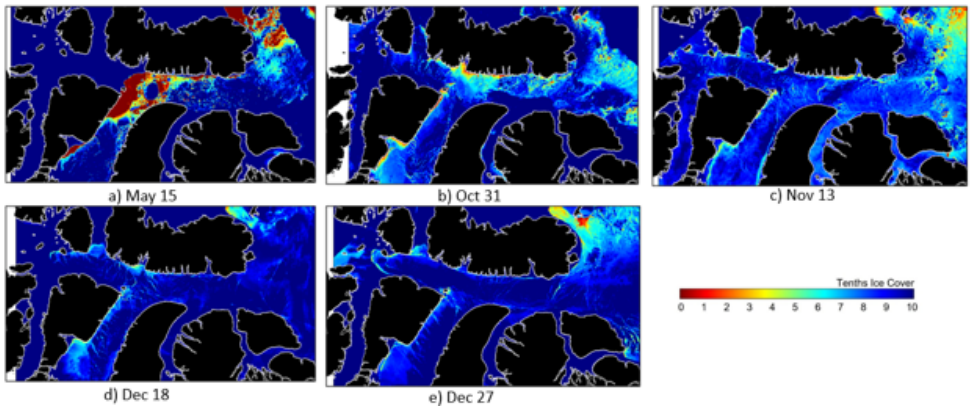

Figure B.6: 2017 ACIC Images of Lancaster Sound using MetOp-A Satellite Data: May 15 - Dec 27

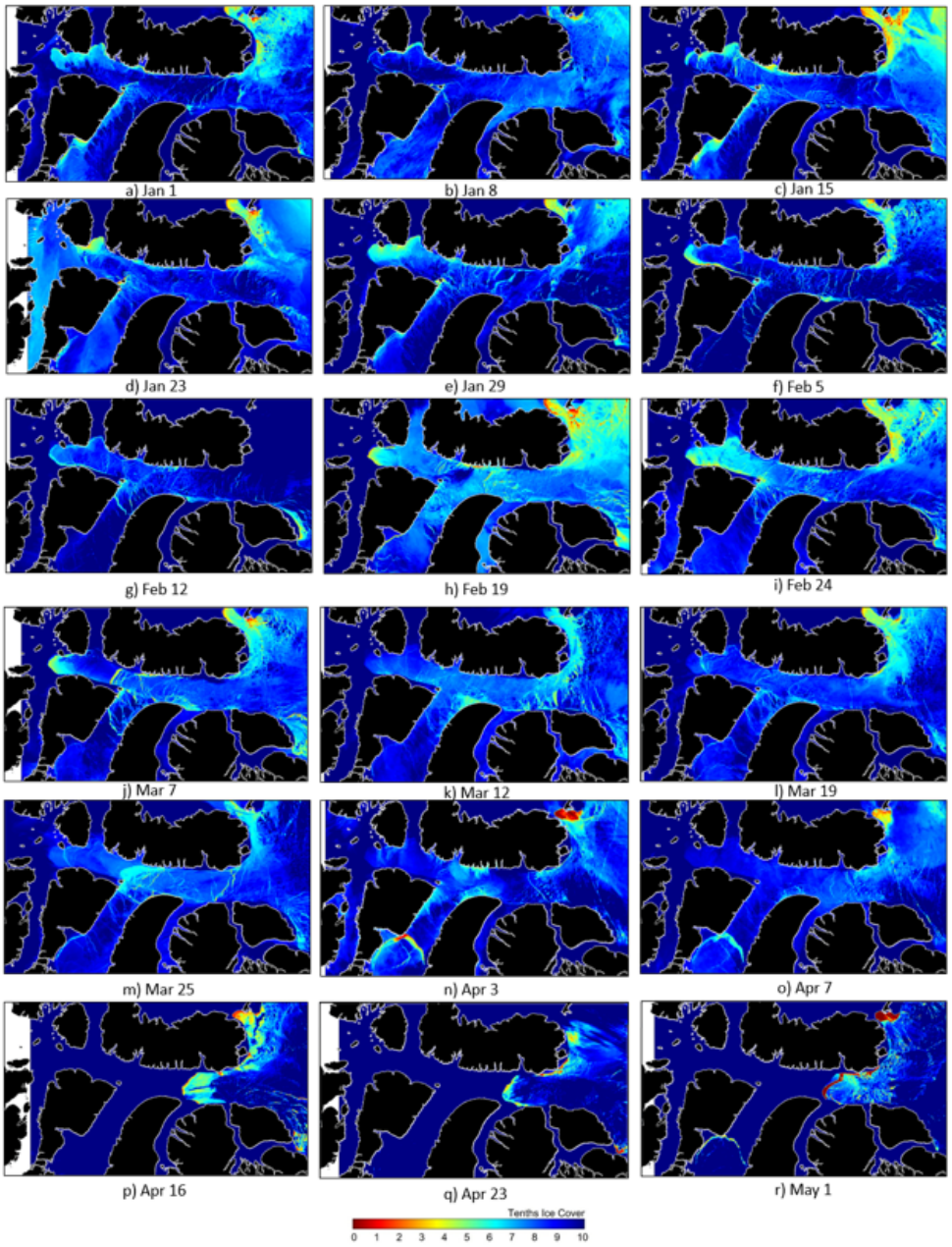

Figure B.7: 2018 ACIC Images of Lancaster Sound using MetOp-A Satellite Data: Jan 1 - May 1

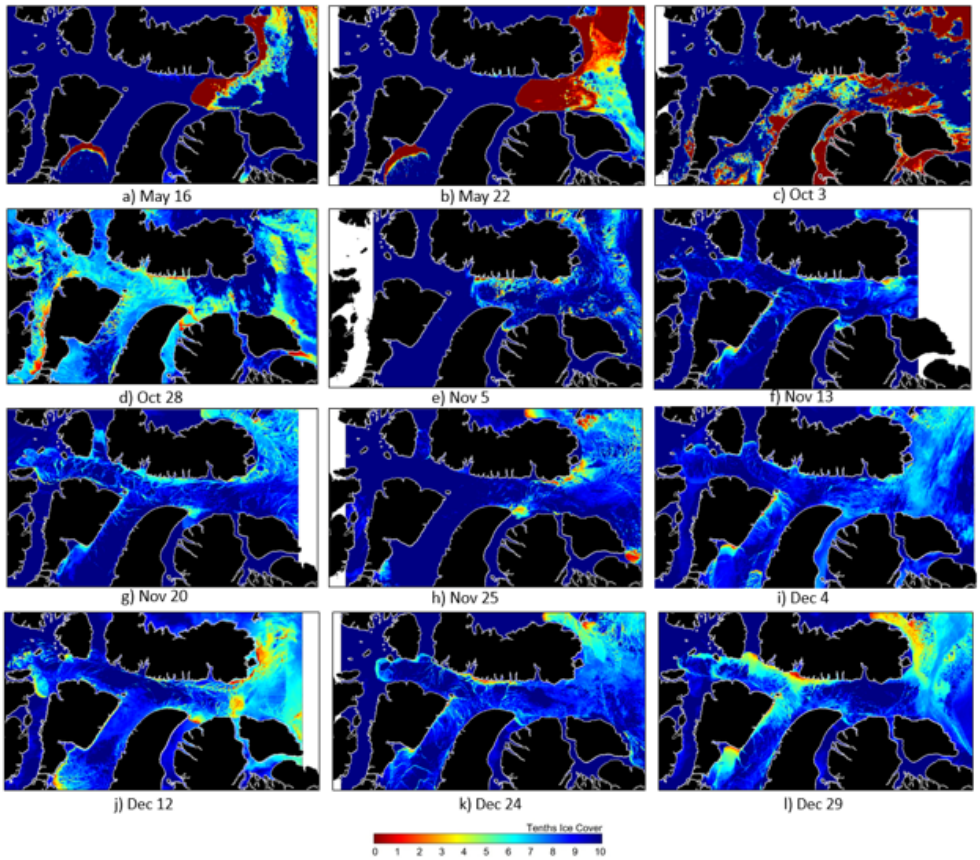

Figure B.8: 2018 ACIC Images of Lancaster Sound using MetOp-A Satellite Data: May 16 - Dec 29

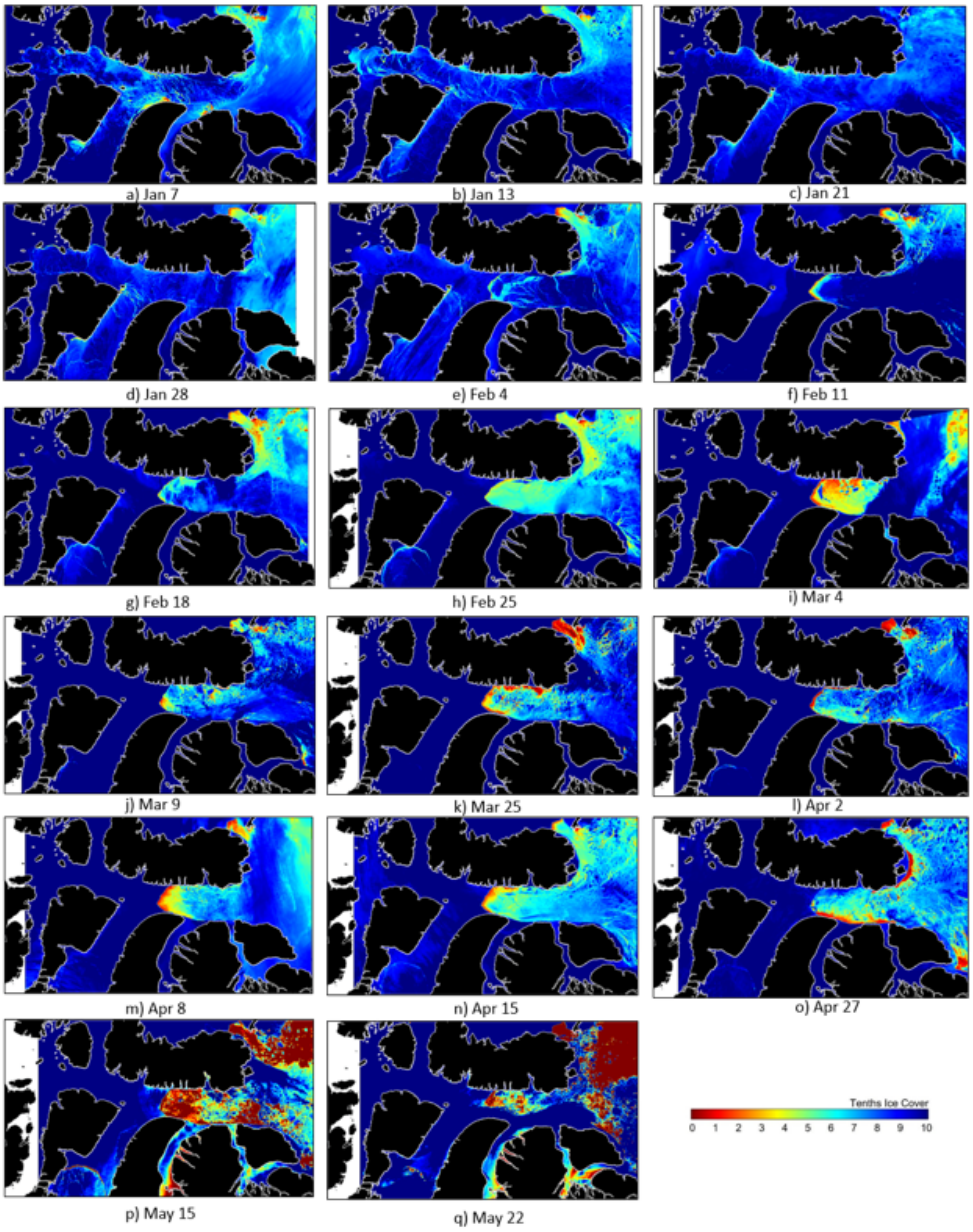

Figure B.9: 2019 ACIC Images of Lancaster Sound using MetOp-A Satellite Data: Jan 7 - May 22

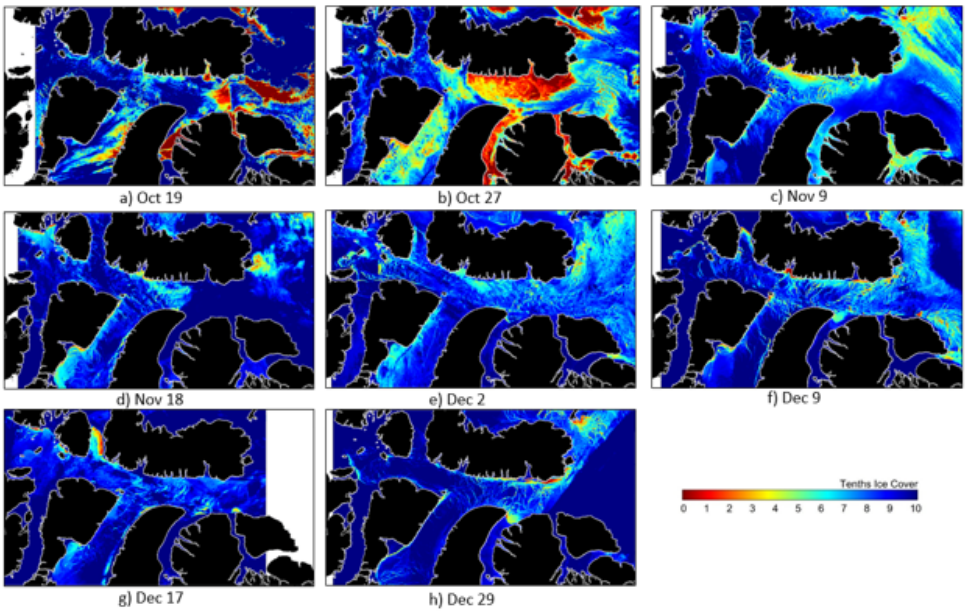

Figure B.10: 2019 ACIC Images of Lancaster Sound using MetOp-A Satellite Data: Oct 19 - Dec 29

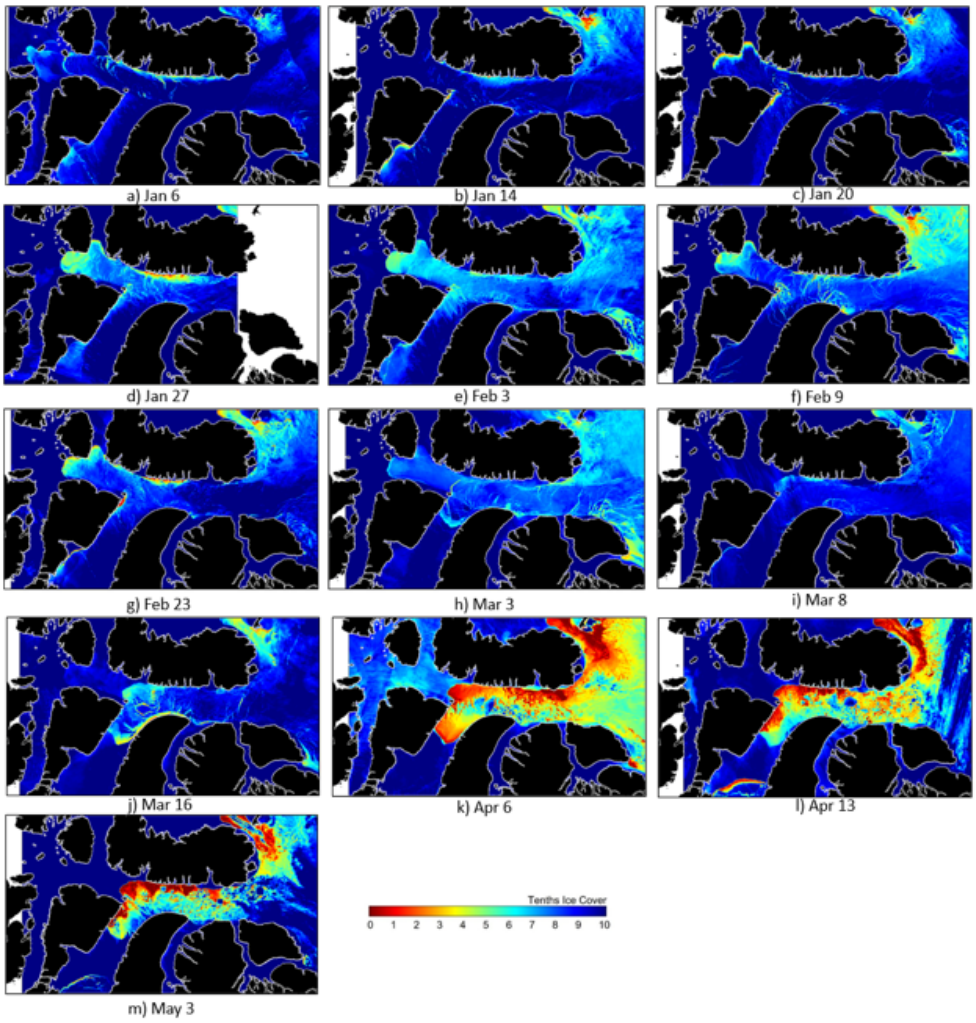

Figure B.11: 2020 ACIC Images of Lancaster Sound using MetOp-A Satellite Data: Jan 6 - May 3

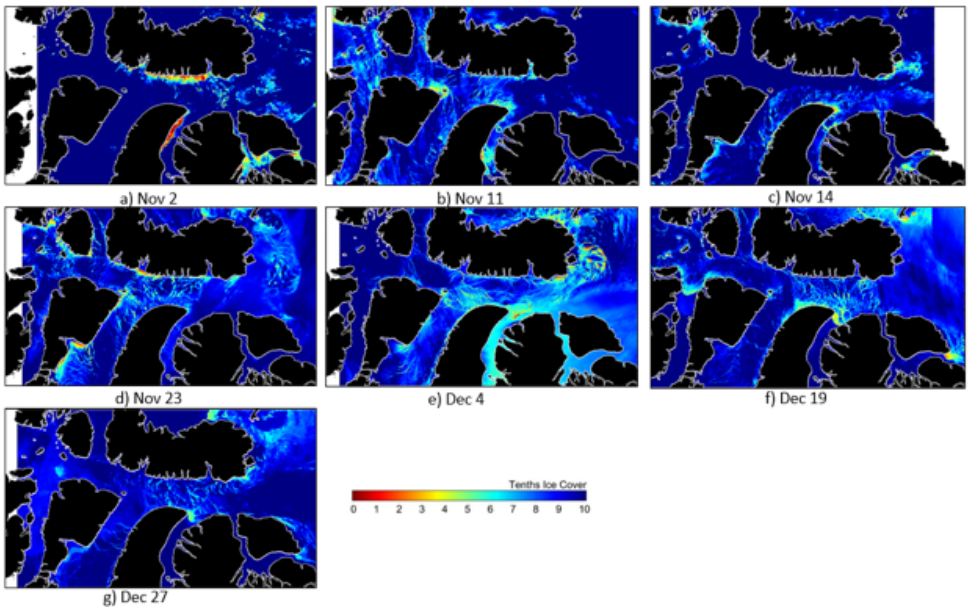

Figure B.12: 2020 ACIC Images of Lancaster Sound using MetOp-A Satellite Data: Nov 2 - Dec 27

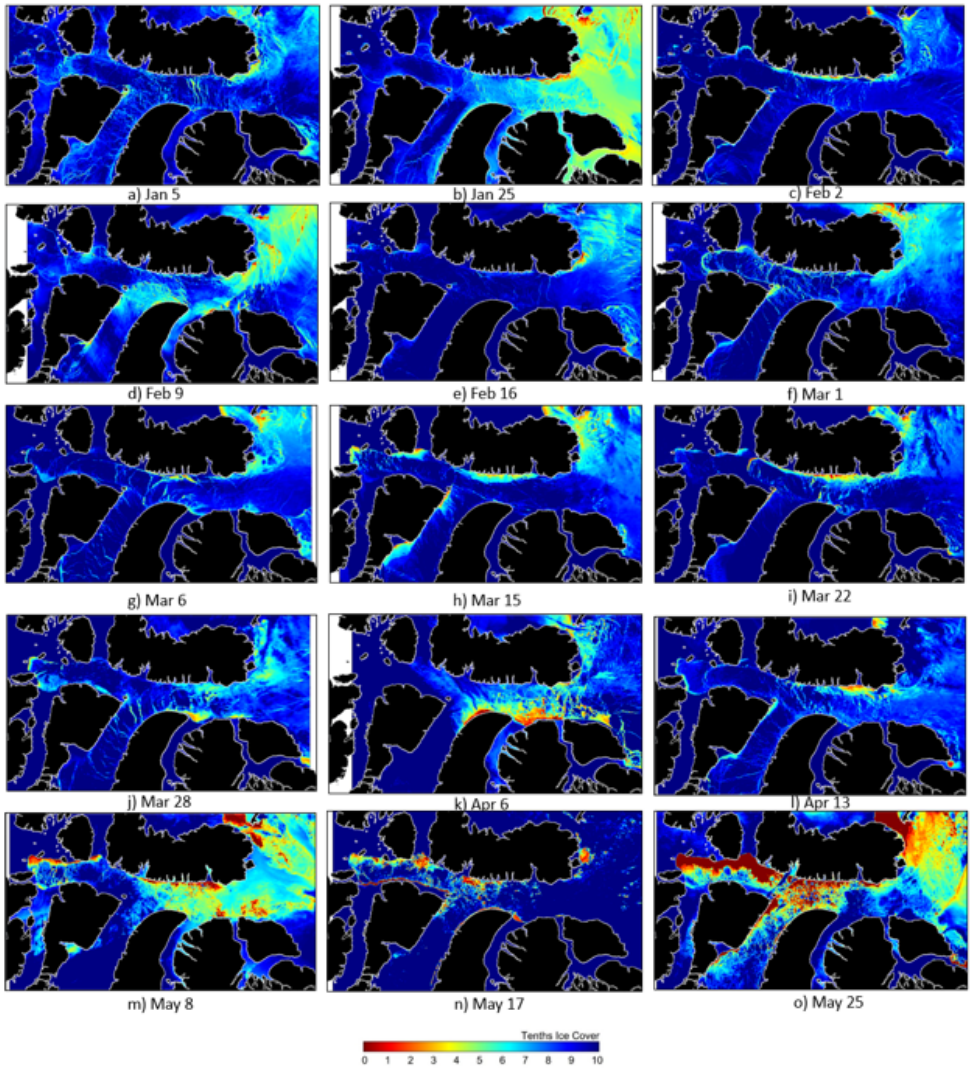

Figure B.13: 2021 ACIC Images of Lancaster Sound using MetOp-A Satellite Data: Jan 5 - May 25

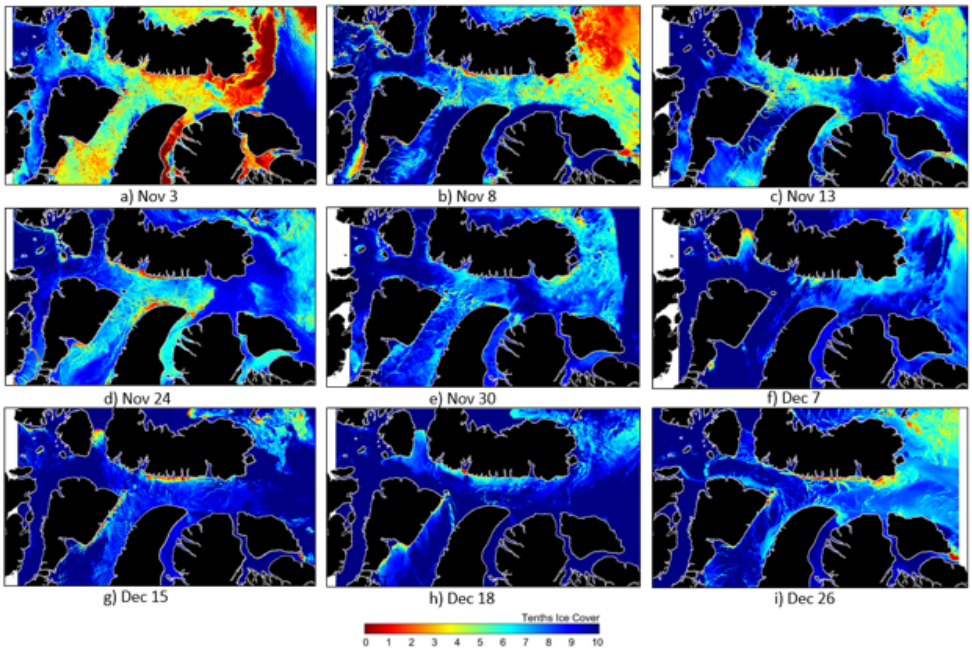

Figure B.14: 2021 ACIC Images of Lancaster Sound using MetOp-B/C for November and December Satellite Data: Nov 3 - Dec 26

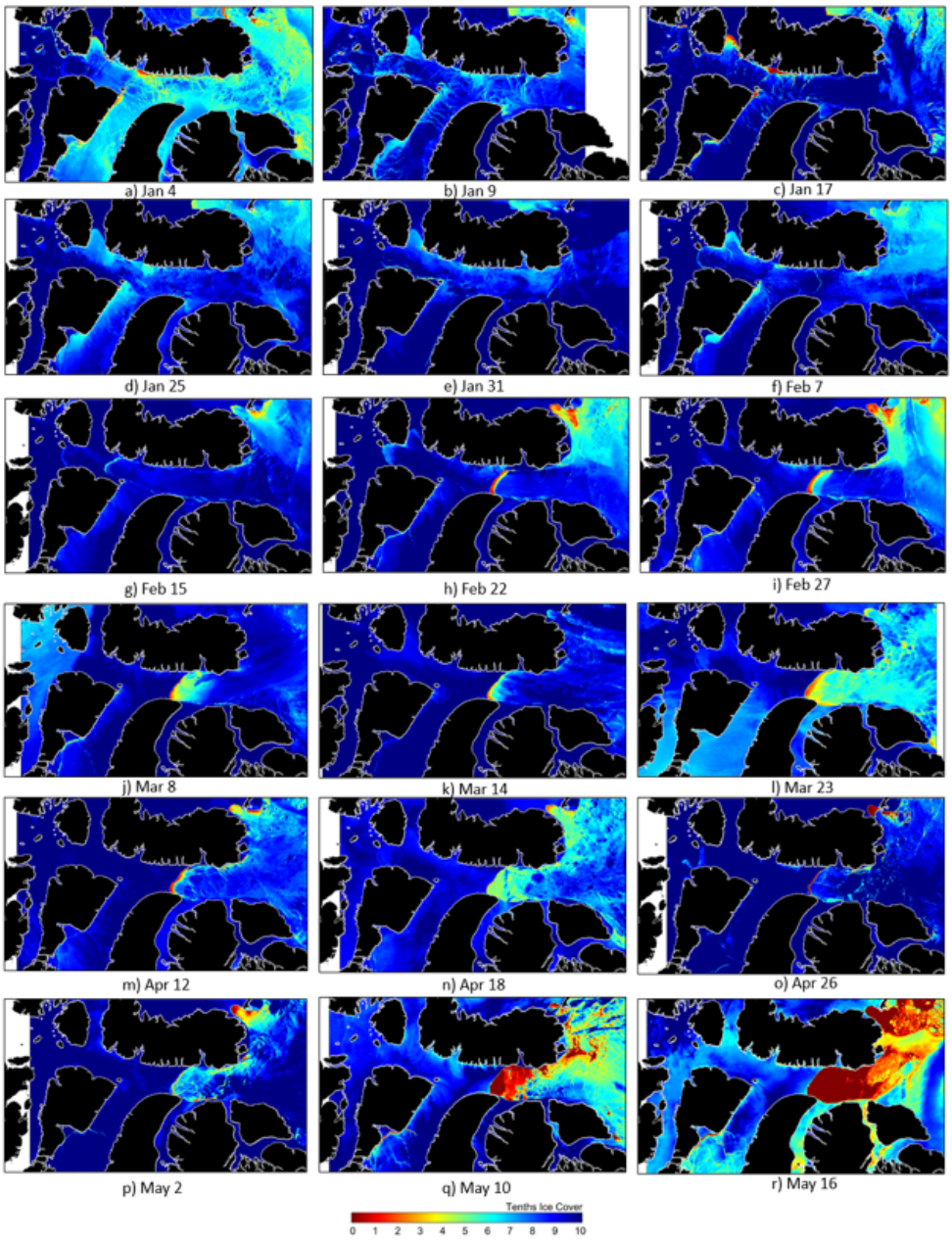

Figure B.15: 2022 ACIC Images of Lancaster Sound using MetOp-B/C Satellite Data: Jan 4 - May 16

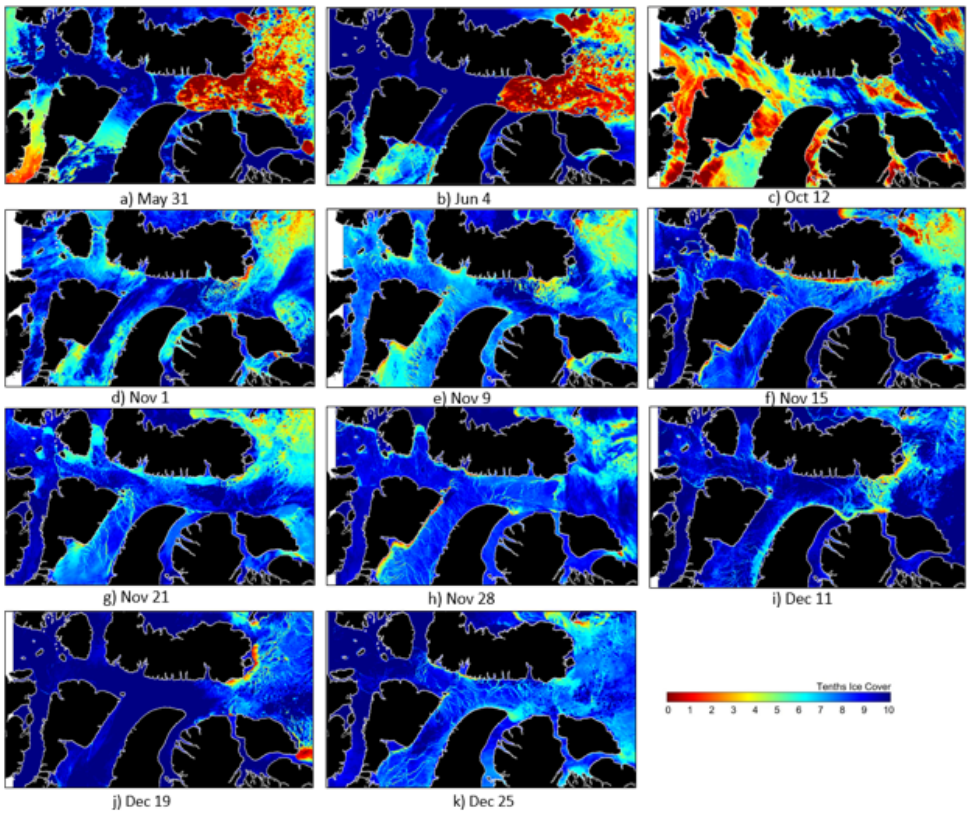

Figure B.16: 2022 ACIC Images of Lancaster Sound using MetOp-B/C Satellite Data: May 31 - Dec 25

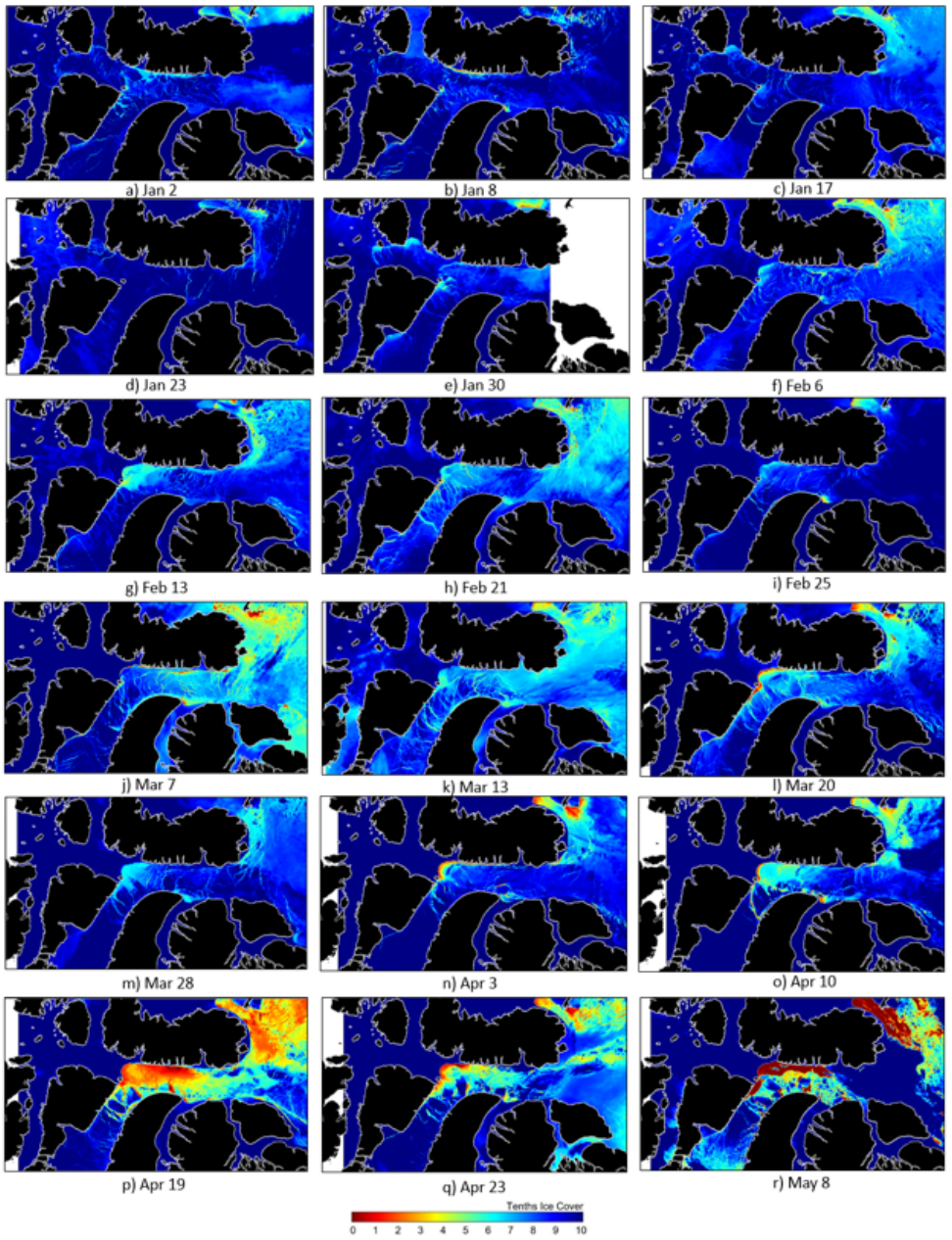

Figure B.17: 2023 ACIC Images of Lancaster Sound using MetOp-B/C Satellite Data: Jan 2 - May 8

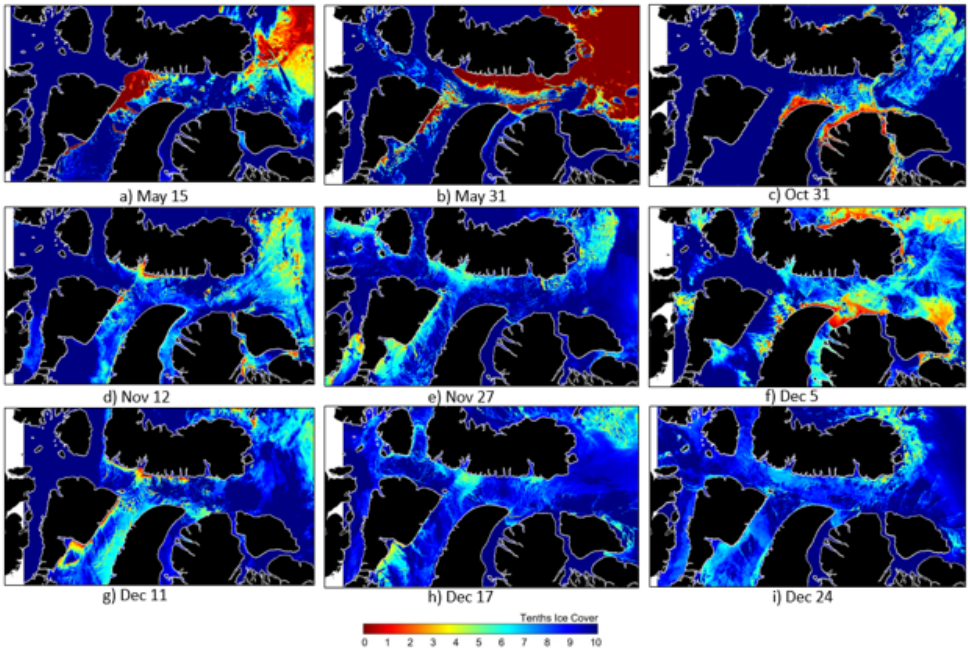

Figure B.18: 2023 ACIC Images of Lancaster Sound using MetOp-B/C Satellite Data: May 15 - Dec 24

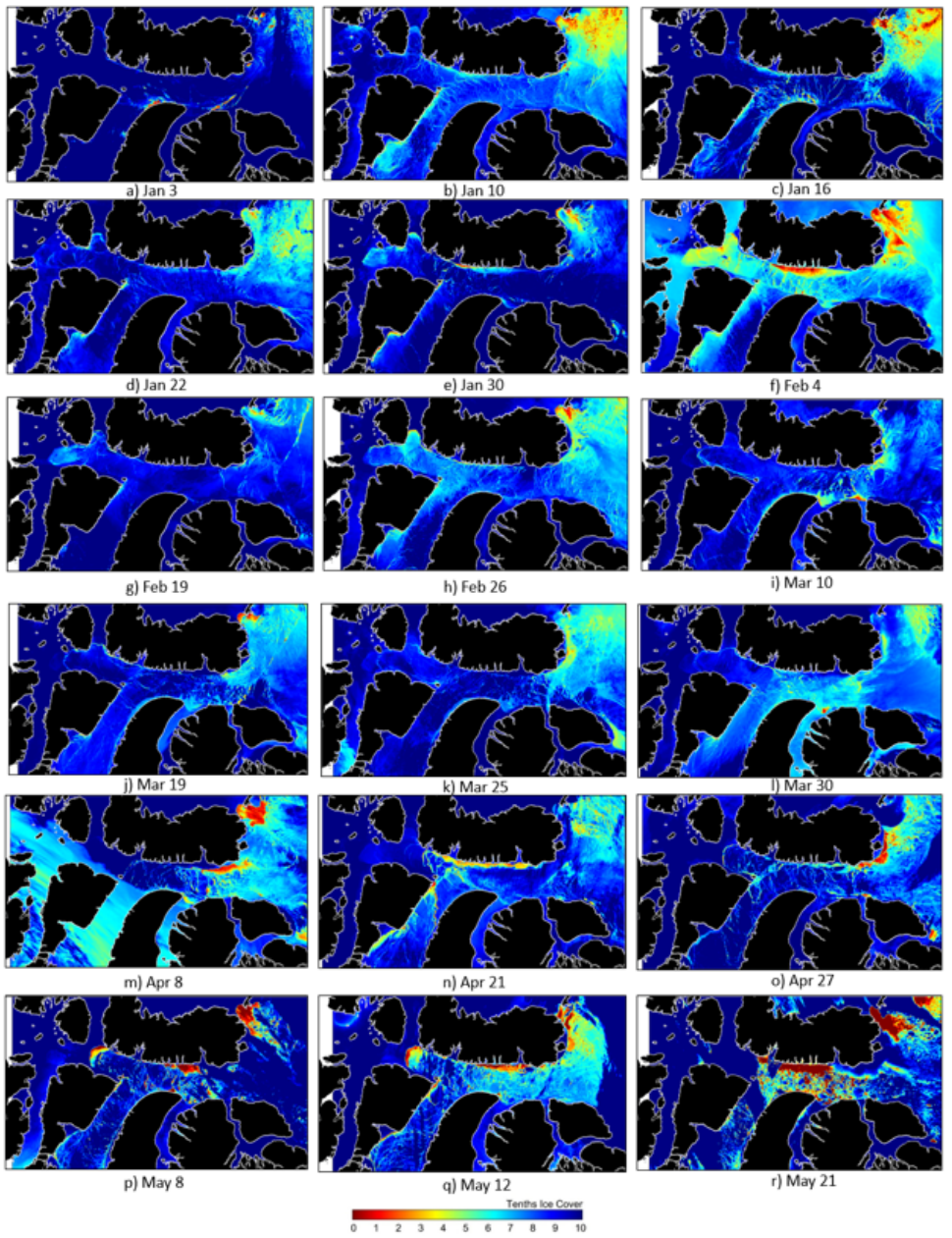

Figure B.19: 2024 ACIC Images of Lancaster Sound using MetOp-B/C Satellite Data: Jan 3 - May 21

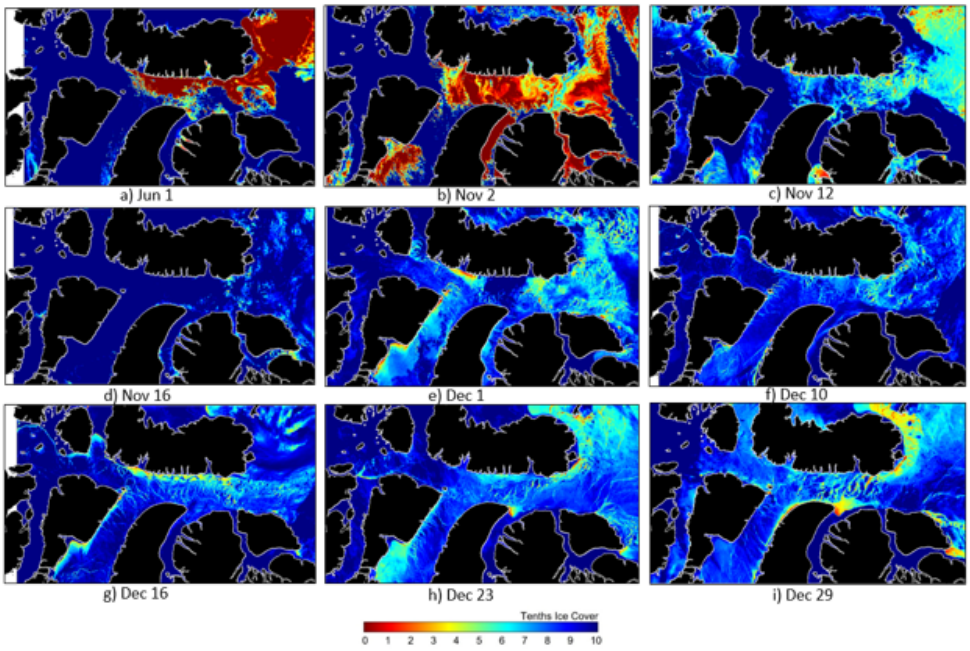

Figure B.20: 2024 ACIC Images of Lancaster Sound using MetOp-B/C Satellite Data: Jun 1 - Dec 29

C Calendar Day # Charts

This Appendix contains Figs. C.1 and C.2, which provide the calendar day # for each month and day date of the year.

C.1 Normal Year

Jan	Feb	Mar	Apr	May	Jun	Jul	Aug	Sep	Oct	Nov	Dec
1	32	60	91	121	152	182	213	244	274	305	335
2	33	61	92	122	153	183	214	245	275	306	336
3	34	62	93	123	154	184	215	246	276	307	337
4	35	63	94	124	155	185	216	247	277	308	338
5	36	64	95	125	156	186	217	248	278	309	339
6	37	65	96	126	157	187	218	249	279	310	340
7	38	66	97	127	158	188	219	250	280	311	341
8	39	67	98	128	159	189	220	251	281	312	342
9	40	68	99	129	160	190	221	252	282	313	343
10	41	69	100	130	161	191	222	253	283	314	344
11	42	70	101	131	162	192	223	254	284	315	345
12	43	71	102	132	163	193	224	255	285	316	346
13	44	72	103	133	164	194	225	256	286	317	347
14	45	73	104	134	165	195	226	257	287	318	348
15	46	74	105	135	166	196	227	258	288	319	349
16	47	75	106	136	167	197	228	259	289	320	350
17	48	76	107	137	168	198	229	260	290	321	351
18	49	77	108	138	169	199	230	261	291	322	352
19	50	78	109	139	170	200	231	262	292	323	353
20	51	79	110	140	171	201	232	263	293	324	354
21	52	80	111	141	172	202	233	264	294	325	355
22	53	81	112	142	173	203	234	265	295	326	356
23	54	82	113	143	174	204	235	266	296	327	357
24	55	83	114	144	175	205	236	267	297	328	358
25	56	84	115	145	176	206	237	268	298	329	359
26	57	85	116	146	177	207	238	269	299	330	360
27	58	86	117	147	178	208	239	270	300	331	361
28	59	87	118	148	179	209	240	271	301	332	362
29		88	119	149	180	210	241	272	302	333	363
30		89	120	150	181	211	242	273	303	334	364
31		90		151		212	243		304		365
Jan	Feb	Mar	Apr	May	Jun	Jul	Aug	Sep	Oct	Nov	Dec

Figure C.1: Day of Year Calendar - Normal Year (sourced from [89])

C.2 Leap Year

Leaps years in this study were 2016, 2020 and 2024.

Jan	Feb	Mar	Apr	May	Jun	Jul	Aug	Sep	Oct	Nov	Dec
1	32	61	92	122	153	183	214	245	275	306	336
2	33	62	93	123	154	184	215	246	276	307	337
3	34	63	94	124	155	185	216	247	277	308	338
4	35	64	95	125	156	186	217	248	278	309	339
5	36	65	96	126	157	187	218	249	279	310	340
6	37	66	97	127	158	188	219	250	280	311	341
7	38	67	98	128	159	189	220	251	281	312	342
8	39	68	99	129	160	190	221	252	282	313	343
9	40	69	100	130	161	191	222	253	283	314	344
10	41	70	101	131	162	192	223	254	284	315	345
11	42	71	102	132	163	193	224	255	285	316	346
12	43	72	103	133	164	194	225	256	286	317	347
13	44	73	104	134	165	195	226	257	287	318	348
14	45	74	105	135	166	196	227	258	288	319	349
15	46	75	106	136	167	197	228	259	289	320	350
16	47	76	107	137	168	198	229	260	290	321	351
17	48	77	108	138	169	199	230	261	291	322	352
18	49	78	109	139	170	200	231	262	292	323	353
19	50	79	110	140	171	201	232	263	293	324	354
20	51	80	111	141	172	202	233	264	294	325	355
21	52	81	112	142	173	203	234	265	295	326	356
22	53	82	113	143	174	204	235	266	296	327	357
23	54	83	114	144	175	205	236	267	297	328	358
24	55	84	115	145	176	206	237	268	298	329	359
25	56	85	116	146	177	207	238	269	299	330	360
26	57	86	117	147	178	208	239	270	300	331	361
27	58	87	118	148	179	209	240	271	301	332	362
28	59	88	119	149	180	210	241	272	302	333	363
29	60	89	120	150	181	211	242	273	303	334	364
30		90	121	151	182	212	243	274	304	335	365
31		91		152		213	244		305		366
Jan	Feb	Mar	Apr	May	Jun	Jul	Aug	Sep	Oct	Nov	Dec

Figure C.2: Day of Year Calendar - Leap Year (sourced from [89])